EFFECT OF FREESTREAM VORTICAL STRUCTURES AND VORTICITY ON STAGNATION REGION HEAT TRANSFER

AUNG NAING OO

EFFECT OF FREESTREAM VORTICAL STRUCTURES AND VORTICITY ON STAGNATION REGION HEAT TRANSFER

by

©Aung Naing Oo

A thesis submitted to the

School of Graduate Studies

in partial fulfillment of the

requirements for the degree of

Doctor of Philosophy

Faculty of Engineering and Applied Science

Memorial University of Newfoundland

January 2002

St. John's Newfoundland

Abstract

An experimental study was performed to investigate the influence of freestream turbulence with coherent vortical structures on stagnation region heat transfer. A heat transfer model with a cylindrical leading edge was tested in a low speed wind tunnel at Reynolds numbers ranging from 67,750 to 142,250 based on leading edge diameter of the model. Grids of parallel rods with diameters 2.86 cm, 1.59 cm and 0.95 cm were used to generate the freestream turbulence with well-defined primary vortex lines. The grids were placed at several locations upstream of the heat transfer model in orientations where the rods were perpendicular and parallel to the stagnation line. Hot-wire anemometry was used to measure the turbulence characteristics of the freestream turbulence. The freestream turbulence was characterized using the turbulence intensity, integral length scale, lateral velocity and vorticity fluctuating component. The turbulence intensity and the ratio of integral length scale to leading edge diameter were in the range of 3.93 to 11.78% and 0.07 to 0.7, respectively. Characteristics of coherent vortical structures downstream of the grids were examined by analyzing the isotropy of turbulence, lateral velocity and vorticity fluctuating components and the wavelet energy spectra of the lateral fluctuating velocity components downstream of the turbulence grids. Heat transfer coefficients were estimated by measuring the temperature distribution and the heat flux. The grids with rods perpendicular to the stagnation line, where the primary vortical structures are expected to be perpendicular to the stagnation line, result in higher heat transfer than those with rods parallel to the stagnation line. The difference between the

two grid orientations was more pronounced for the bigger rod-grids. The measured heat transfer data and freestream turbulence characteristics were compared with existing correlation models. An attempt to predict the heat transfer augmentation at the stagnation line due to the turbulence with coherent vortical structures using a neural network was made. A new correlation for the stagnation line heat transfer, which includes the spanwise fluctuating vorticity components, has been developed.

Acknowledgements

I would like to express my sincerest gratitude to Dr. Chan Ching for his excellent advice, unfading patience, invaluable guidance, brotherly care and continuous encouragement throughout the study period. I also thank Dr. Neil Hookey and Dr. Michael Hinchey for their useful suggestions and good-hearted help.

The financial support of the Natural Sciences and Engineering Research Council (NSERC) of Canada to conduct this experimental study is gratefully acknowledged.

Special thanks are also given to the technicians, staff members and friends at the Faculty of Engineering and Applied Science for their kind assistance.

Finally, I would like to mention my heartiest gratitude to my beloved wife, Thi, and my family for their patience and understanding.

Table of Contents

List of Tables

List of Figures

List of Abbreviations and Symbols

a	=	Wavelet dilation parameter (s)
A	=	Area of the heated portion of the leading edge (m^2)
b	=	Wavelet location parameter (s)
C	=	Chord length of a turbine blade (m)
C_f	=	Correction factor
C_g	=	Admissibility constant
$C_t(a,b)$	=	Wavelet transform using wavelet scale a at location b
d	=	Diameter of a rod (m)
D	=	Diameter of cylindrical leading edge (m)
$E(f)$	=	Energy spectra (m^2/s)
f	=	Frequency (Hz)
f_c	=	Frequency of the passband center of the wavelet (Hz)
f_k	=	Kolmogorov frequency (Hz)
f_s	=	Sampling frequency (Hz)
Fr	=	Frossling Number ($Nu / \sqrt{Re_D}$)
F_v	=	Dimensionless vortex force
g	=	Wavelet function
h	=	Heat transfer Coefficient (W/m^2K)
I	=	Current (Ampere)
Iso	=	Degree of isotropy

k	=	Thermal conductivity (W/m.K)
Nu	=	Nusselt number (= hD/k)
Q_{cond}	=	Conduction heat loss (W)
Q_{cov}	=	Convection heat transfer (W)
Q_{in}	=	Heat input (W)
Q_{rad}	=	Radiation heat loss (W)
$R(\tau)$	=	Autocorrelation function for time shift τ
Re_d	=	Reynolds number based on d (= Ud/ν)
Re_D	=	Reynolds number based on D (= UD/ν)
$s(t)$	=	Signal variable (herein velocity)
s	=	Distance between two wires (m)
S	=	Instantaneous velocity of fluid flow over a hot wire (m/s)
t	=	Time (s)
Tu	=	Streamwise Turbulence Intensity (%) (= $u/U \times 100$)
$Tw(\theta)$	=	Temperature of the leading edge at angle θ (K)
T_∞	=	Temperature of freestream (K)
u	=	rms of fluctuating velocity component in streamwise direction (m/s)
U	=	Mean freestream velocity (m/s)
Un	=	Uncertainty (%)
v	=	rms of fluctuating velocity component in spanwise Y direction (parallel to stagnation line) (m/s)
V	=	Mean velocity in spanwise Y direction (m/s)

Vo	=	Voltage (V)
w	=	rms of fluctuating velocity component in spanwise Z direction (perpendicular to stagnation line) (m/s)
W	=	Mean velocity in spanwise Z direction
x	=	Distance downstream of the grid (m)
X	=	Streamwise distance measured along a turbine blade from the stagnation line (m)
Y	=	Spanwise direction parallel to the stagnation line
Z	=	Spanwise direction perpendicular to the stagnation line
θ	=	Angle measured from the stagnation point (degree)
ε	=	Turbulent kinetic energy dissipation rate (m^2/s^3)
ν	=	Kinematic viscosity of freestream (m^2/s)
τ	=	Time shift (s)
η	=	Kolmogorov length scale (m)
λ_x	=	Streamwise integral length scale of turbulence (m)
ω_c	=	Angular frequency of the passband center of the wavelet (rad/s)
ω_y	=	rms of fluctuating vorticity component in spanwise Y direction (1/s)
Ω_y	=	Instantaneous vorticity in spanwise Y direction (1/s)
ω_z	=	rms of fluctuating vorticity component in spanwise Z direction (1/s)
Ω_z	=	Instantaneous vorticity in spanwise Z direction (1/s)

List of Appendices

Chapter I

Introduction

1.1 Importance of Stagnation Region Heat Transfer

Stagnation region heat transfer in the presence of freestream turbulence is important in a number of common engineering applications. For example, in heat transfer devices such as boilers and tubular heat exchangers, the cross-flow over the tubes results in a stagnation region. Heat transfer in the stagnation region is significantly augmented when the freestream becomes turbulent. The augmentation in heat transfer depends on the flow characteristics, physical properties of the fluid, shape, size and surface roughness of the stagnation region. Stagnation region heat transfer is probably the most critical in the blunt leading edge region of gas turbine airfoils where the temperature of the combustion gases often exceeds the allowable temperature limit of the blade materials. As a ten percent increase in the turbine inlet temperature from the current level of 1950 K can result in an approximate 40% increase in specific power output, in kW/kg/s, of a gas turbine (Lakshminarayana, 1996), modern gas turbine engines tend to use increasingly higher turbine inlet temperatures. Turbine inlet temperatures are, however, limited by the allowable turbine blade metal temperature. While newer blade materials such as ceramic composites and ceramic coatings are under development, the usual practice to achieve higher inlet temperatures is through turbine blade cooling. The cooling is usually accomplished by bleeding air from the compressor outlet and directing it through cooling channels on the blade (Figure 1.1). The effectiveness of the cooling technique is important since a smaller cooling airflow requirement would lead to a higher overall efficiency of the turbine. A great deal of research on improving both blade cooling systems and allowable metal temperatures has been performed over the last few decades (Hannis and Smith, 1982; LeGrives, 1986). Significant improvements in blade cooling techniques have produced greater increases in turbine inlet temperature than development of better material technology (see Figure 1.2). While modern gas turbines operate at turbine inlet temperatures of about 1500 °C, advanced blade cooling techniques keep the blade surface at temperatures lower than the allowable metal temperature of about 950 °C (Bathie, 1996; Lakshminarayana, 1996; Sato et al., 1997; Duffy et al., 1997). As the exit temperature of a modern high enthalpy rise combustor can be greater than 2000 °C, there is still significant potential to increase turbine inlet temperatures by further improving blade cooling techniques and allowable metal temperatures.

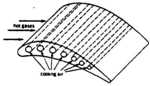

Figure 1.1 Illustration of Turbine Blade Cooling (Bathie, 1996)

Accurate prediction of turbine blade heat transfer (i.e. heat transfer from combustion gases to turbine blades) is essential to improve blade cooling system designs.

A complete understanding of turbine blade heat transfer, however, may be difficult, since gas turbine flows are complex with high turbulence, strong secondary flows, rotational effects, airfoil row interaction (rotor/stator and stator/rotor), local flow separation and shock-boundary layer interactions (Blair et al., 1989). The predictions of heat transfer to the first stage blades and vanes of a newly designed gas turbine can be in error by a factor of two or three under certain engine conditions (Maciejewski and Moffat, 1992; Larsson, 1997). However, a fundamental understanding of the isolated influence of each of the above effects on heat transfer would allow them to be incorporated more effectively into cooling system designs.

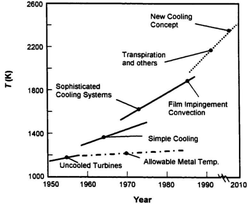

Figure 1.2 Variation of Turbine Inlet Temperature over Recent Years (Adopted from Copyright © Rolls Royce, plc.)

The stagnation region is of interest because heat transfer is usually a maximum at the blunt leading edge of the airfoils (see Figure 1.3). The physics of stagnation region heat transfer in the presence of freestream turbulence is still poorly understood despite the number of empirical correlations that have been developed.

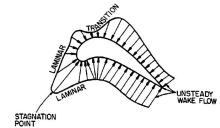

Figure 1.3 Heat Transfer Distribution over a Turbine Blade (Lakshminarayana, 1996)

1.2 Influence of Freestream Vorticity and Vortical Structures

Turbulence is characterized by fluctuating vorticity, and in a sense, vorticity can be viewed as the underlying characteristic of turbulence (Tennekes and Lumley, 1972). Heat transfer augmentation in the stagnation region is hypothesized to be caused by vorticity amplification (Sutera et al., 1963; Sutera, 1965; Morkovin, 1979). If a vortical filament, which is normal to the stagnation line and freestream flow direction, is considered, the filament is stretched and tilted as it is advected into the stagnation region due to divergence and acceleration around the bluff body (see Figure 1.4). This stretching causes the vorticity to be intensified through conservation of angular momentum. The vortical filament with intensified vorticity interacts with the boundary layer and induces velocity gradients in the spanwise direction parallel to the stagnation line. The three-dimensional velocity gradients enhance the transport mechanism within the boundary layer resulting in higher heat transfer. On the other hand, a vortical filament which is parallel to the stagnation line is not stretched, due to no apparent velocity divergence in this direction, as it approaches the stagnation region. Prior experimental and numerical studies (Sutera et al., 1963; Sutera, 1965; Kestin and Wood,1971; VanFossen and Simoneau, 1987; Rigby and VanFossen, 1991) show that this intensification of vorticity causes heat transfer to increase while the boundary layer remains laminar. A complete understanding of the transport mechanisms of momentum and heat in turbulent flows has not been achieved, however, it is well established that the coherent vortical structures in a turbulent flow play an important role in momentum transport and heat transfer. Manipulation of these vortical structures could result in a change in heat transfer (Jacobson and Reynolds, 1993; Ho and Tai, 1996; Kasagi and Iida, 1999).

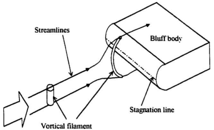

Figure 1.4 Vortex Filaments Stretched and Tilted by Divergence of Streamlines and Acceleration around Leading Edge

Several attempts have been made to understand the relationship between freestream turbulence and stagnation region heat transfer by studying the isolated effect of turbulent intensity, Reynolds number, unsteady wake, stagnation point velocity gradient and integral length scale (Smith and Kuethe, 1966; Kestin and Wood, 1971; Lowery and Vachon, 1975; O' Brien and VanFossen, 1985; Mehendale et al., 1991; Han et al., 1993; Zhang and Han, 1994; VanFossen et al., 1995; Ahmaed and Yovanovich, 1997; Du et al., 1997). The study of the effect of freestream vorticity on the stagnation region heat transfer is, however, very limited, and no considerable efforts to include the information on vortical structures in the mathematical models have been done. If the heat transfer mechanism in gas turbine blades is considered, it is rational to study the effect of freestream vortical structures and vorticity on the stagnation region heat transfer as the turbulence at turbine inlet is expected to be highly anisotropic (Johnston, 1974) and well laced with coherent vortical structures (Lakshminarayana, 1996).

1.3 Objectives of the Study

Describing a turbulent flow without reference to the vorticity field and vortical structures is unlikely to provide a complete picture of the turbulence. A knowledge of the effect of freestream vorticity and vortical structures on stagnation region heat transfer should lead to a better understanding of the physical mechanism of the heat transfer. The goal of the current study is, therefore, to investigate the influence of freestream vorticity and vortical structures on the stagnation region heat transfer. The specific objectives of the study are:

(i) To generate turbulence with different vortical structures (one with primary vortices susceptible to stretching and another with primary vortices not susceptible to stretching as they approach the stagnation region);

(ii) To quantify the freestream turbulence by measuring the fluctuating velocity components, integral length scale and the vorticity field and to analyze the characteristics of vortical structures;

(iii) To quantify the heat transfer enhancement in the stagnation region by the two different turbulent flows in (i);

(iv) To examine the nature of heat transfer augmentation over the stagnation region by different freestream coherent vortical structures;

(v) To investigate the difference in stagnation region heat transfer due to freestream turbulence with distinct vortical structures and that due to turbulence generated using square mesh grids; and

(vi) To examine the relationship between the characteristics of the freestream turbulence, including information pertaining to the vortical structures and the vorticity field, and stagnation region heat transfer.

1.4 Rationale of the Study

By including the vortical structures and vorticity field to characterize the freestream turbulence, this study should provide a better understanding of the stagnation region heat transfer. To the author's knowledge, this is the first study that would incorporate freestream vortical structures and vorticity when formulating models for the heat transfer. The conjecture that vorticity amplification in the stagnation region plays an important role had not been experimentally proven, and this study should produce quantitative experimental information on the relation between the freestream vorticity and stagnation heat transfer. Most previous studies have focused on the effect of isotropic turbulence generated by square mesh grids on heat transfer augmentation. The influence of freestream turbulence with different vortical structures, i.e. turbulence with a specific direction of vorticity, should be useful in many engineering applications. Empirical models based on a more complete description of the freestream turbulence should not only lead to more reliable estimates of heat transfer augmentation, but also provide further insight into the physical mechanism of stagnation region heat transfer.

1.5 Methodology

The experimental study included two major parts: (i) to generate and quantify the characteristics of freestream turbulence with distinct coherent vortical structures; and (ii) to measure the heat transfer in the stagnation region.

(i) Turbulence Generation and Measurements

The experiments were performed in a low speed wind tunnel, and passive turbulence grids with parallel rods were used to generate the freestream turbulence with well-defined vortex lines. The characteristics of turbulence were measured using hot wire anemometry. A hot wire vorticity probe designed and built in-house was used for the vorticity measurements. The Reynolds number, velocity fluctuations, integral length scale and spanwise fluctuating vorticity components were used to characterize the freestream turbulence. The vortical structures were investigated using the wavelet transform technique.

(ii) Heat Transfer Measurement in the Stagnation Region

The stagnation region was simulated using a heat transfer model with a cylindrical leading edge. The cylindrical leading edge had a heated metal surface with a uniform heat flux. A number of thermocouples were embedded on the leading edge to measure surface temperatures in order to estimate the heat transfer in the stagnation region.

Chapter II

Literature Review

2.1 Heat Transfer in the Stagnation Region

Accurate prediction of stagnation region heat transfer in the presence of freestream turbulence is important in a number of engineering applications. The influence of turbulence intensity, integral length scale, Reynolds number, surface roughness, pressure gradient and body shape on stagnation region heat transfer has been investigated by several researchers using a variety of experimental and numerical techniques. In most cases, the augmentation of heat transfer with a specific parameter is presented, and models which correlate certain characteristics of freestream turbulence with stagnation region heat transfer have been formulated. Despite the extensive amount of research, a complete understanding of the heat transfer process has not yet been obtained. This is primarily because of the complex manner in which a large number of parameters affect the heat transfer process.

Heat transfer between the freestream and the surface depends to a large extent on the nature of the boundary layer at the surface. The boundary layer, in turn, depends on several parameters such as Reynolds number, freestream turbulence intensity, pressure gradient, surface roughness, etc. For the same temperature difference between the freestream and the surface, a thinner boundary layer leads to higher heat transfer rate due to a greater temperature gradient across the thermal boundary layer. Heat transfer increases substantially when the laminar boundary layer becomes turbulent, because the momentum transfer and heat transfer are closely coupled. However, the physical mechanism of heat transfer at the leading edge is quite unique, because heat transfer is significantly augmented by freestream turbulence while the boundary layer is believed to remain laminar in this region. Furthermore, heat transfer unsteadiness, defined as the ratio of the rms to mean heat transfer rate, is a maximum at the stagnation point (Ching and O'Brien, 1991). Although a complete understanding of the transport mechanisms of momentum and heat in turbulent flows has not been achieved, it is well established that the coherent vortical structures in a turbulent flow play an important role in momentum and heat transfer. A knowledge of the nature of heat transfer augmentation in the stagnation region due to the freestream turbulence with well defined vortical structures should, therefore, lead to better understanding of the physics in this region. Characteristics of stagnation region heat transfer are reviewed from related previous studies and briefly presented, followed by a review of the studies on turbulence with coherent vortical structures. The existing empirical correlation models and predictions by computational methods are also examined and summarized in this section.

2.1.1 Effects of Turbulence Parameters

For a laminar freestream, heat transfer in the stagnation region can be estimated if the pressure distribution is known (Frossling, 1958). However, when the freestream is turbulent, accurate prediction of heat transfer becomes very difficult. Several studies suggest that the thermal boundary layer is more sensitive to freestream turbulence than the hydrodynamic boundary layer.

(i) Reynolds Number

The boundary layer thickness around a bluff body decreases as the Re_D increases, resulting in an increase in heat transfer. This effect can be seen clearly in the experimental data of Achenbach (1975). Heat transfer data on a circular cylinder with a freestream turbulence intensity less than 0.5 percent over a wide range of Reynolds numbers are shown in Figure 2.1 and illustrate the boundary layer effects such as separation and transition on the heat transfer. In the Reynolds number range 3×10^4 to 4×10^6, the flow passes through four distinct flow regimes. The first flow regime, which extends over the Reynolds number range up to 3×10^5, is characterized by a laminar flow separation about 80° from the stagnation line. This is reflected in the heat transfer distribution where downstream of the separation point there is a continuous increase in heat transfer due to the increased transverse exchange of fluid in the separated flow region. Flow in the second regime is marked by separation of the boundary layer on the rear surface of the cylinder and subsequent formation of a separation bubble. The flow reattaches as a turbulent boundary layer with a corresponding marked increase in the heat transfer and finally separates again further downstream. Two experimental curves are presented for the critical flow range, at Re_D=3.1×10^5 and 4×10^5 to illustrate the effect of Reynolds number on the heat transfer peak due to the reattached boundary layer. The third flow regime is distinguished from the second one by the fact that the transition from laminar to turbulent is direct without the occurrence of a separation bubble. No discernible difference in the local heat transfer distribution is observed between the critical and supercritical flow states. For Re_D=1.9×10^6 the transition to turbulence occurs on the front surface of the cylinder indicating that the fourth flow regime has been established. The heat transfer distributions for Re_D=2.8×10^6 and 4×10^6 show the rapid shift of the transition point towards the front stagnation point with increasing Reynolds number.

When the Reynolds number increases by 29 percent, from 3.1×10^5 to 4×10^5, heat transfer in the stagnation region increases by 13.6 percent. It should be noted that Frossling number, $Fr = Nu/\sqrt{\mathrm{Re}_D}$, is used to present the heat transfer distribution on the cylinder in Figure 2.1. The use of Fr collapses the heat transfer distribution to a single curve in the stagnation region at all Re_D since Nu varies linearly with $\sqrt{\mathrm{Re}_D}$.

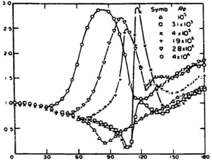

Figure 2.1 Heat Transfer around a Cylinder in Crossflow (Achenbach, 1975)

(ii) Turbulence Intensity

For a given Reynolds number, heat transfer in the stagnation region increases significantly with freestream turbulence intensity. Kestin (1966) determined that a relatively small turbulence intensity of about 5 percent increased the average heat transfer from a heated circular cylinder by about 50 percent. For a given turbulence intensity, the enhancement of heat transfer due to turbulence over the laminar level was found to remain almost constant in the laminar boundary layer region as shown in Figure 2.2.

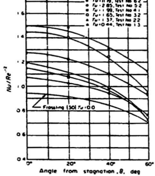

Figure 2.2 Heat Transfer Distribution in the Stagnation Region of a Circular Cylinder

(Lowery and Vachon, 1975)

In a study of heat transfer on a turbine airfoil, Yeh et al., (1993) determined that heat transfer in the stagnation region increased by about 60 percent when turbulence intensity was increased from 1.8 to 5.9 percent for $Re=7\times10^6$ (based on the cascade inlet velocity and blade chord length). Freestream turbulence was found to promote earlier and broader boundary layer transition on the blade and increase the heat transfer in the stagnation region. The same phenomenon was observed in similar experiments at moderate Reynolds numbers in the range 1×10^5 to 3×10^5 (Zhang and Han, 1994; Mehandale et al., 1991; Zhang and Han, 1995; VanFossen et al., 1995; Du et al., 1997).

(iii) Integral Length Scale

The integral length scale describes the average eddy size associated with the turbulence. The size of turbulent eddies has considerable influence on the stagnation region heat transfer as the augmentation is believed to be caused by vorticity amplification (see Figure 1.4). Turbulent eddies that are very large relative to the size of the bluff body are not stretched and, thus, act only as mean flow variations. Eddies that are very small (approaching Kolmogorov scales) are destroyed by viscous dissipation before they can interact with the boundary layer. This leads to the hypothesis that somewhere between these two extremes there must be an optimum eddy size that causes the highest heat transfer augmentation.

Yardi and Sukhatme (1978) found a systematic influence of the integral length scale on the stagnation region heat transfer by using a circular cylinder in crossflow. In their study, turbulence intensities were varied from 1 to 7 percent while the ratio of integral length scale to cylinder diameter ratio was varied from 0.03 to 0.38. They found an increasing heat transfer with decreasing length scale and claimed that the optimum length scale was ten times the boundary layer thickness. VanFossen et al. (1995) used different turbulence grids and models to vary the ratio of integral length scale to leading edge diameter from 0.05 to 0.30. There was an increase in stagnation region heat transfer with decreasing length scale but no optimum length scale was found. Wang et al. (1999) studied the effect of high freestream turbulence with large length scale on heat and mass transfer on a turbine blade which had an effective cylindrical leading edge diameter of 9 mm. In the laminar boundary layer region around the leading edge, lower heat transfer rates were found for the highest freestream turbulence level with large length scale (turbulence intensity of 18% and integral length scale of about 8 cm) than for the moderate turbulence levels with relatively small scales (turbulence intensity of 8.5 % and integral length scale of about 2.6 cm).

(iv) Unsteady Wake

The unsteady wake from the upstream airfoil also influences the stagnation region heat transfer. Han et al. (1993) simulated passing wakes using a rotating spoked wheel and determined that a higher wake Strouhal number ($S = 2\pi Ndn/60U$, where N is the rod rotational speed in rpm, d is the rod diameter, n is the number of rods, and U is the main stream flow velocity at the cascade inlet) greatly enhanced the time-averaged heat transfer coefficient over the stagnation region (Figure 2.3).

Zhang and Han (1995) studied the combined effect of freestream turbulence and unsteady wake on heat transfer from a turbine blade. They defined the mean turbulence intensity as the turbulence level of the combined freestream turbulence and unsteady wake flow. The mean turbulence intensity, regardless of whether it was caused by the unsteady wake or the turbulence generating grid or a combination of both, was an important parameter on the heat transfer rate. A higher Strouhal number also induces earlier and broader boundary layer transition (Han et al., 1993; Zhang and Han, 1995; Du et al., 1997).

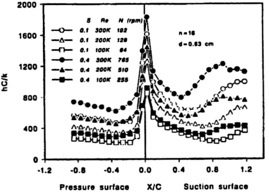

Figure 2.3 Effect of Strouhal Number by Varying Reynolds Number on the Local Heat Transfer Distribution on a Gas Turbine Blade (Han et al., 1993)

(v) Vortical Structures and Vorticity

Vorticity amplification is believed to be an important physical mechanism for heat transfer augmentation in the stagnation region. Although the interaction between a turbulent freestream and the laminar boundary layer in the stagnation region is still not fully understood, amplified vorticity fluctuations seem to excite and induce substantial three-dimensional effects in the boundary layer, thereby enhancing the heat transfer. Furthermore, different coherent vortical structures of freestream turbulence interact differently with the laminar boundary layer resulting in dissimilar heat transfer augmentation.

Sutera et al. (1963, 1964) presented a mathematical model for the interaction of vorticity in the oncoming flow with the two-dimensional stagnation-point boundary layer. The physical situation considered was that of a steady flow, with a sinusoidal variation of velocity superimposed in the normal direction, into a plane stagnation point as shown in Figure 2.4. Vorticity with this orientation is susceptible to stretching in the stagnation-point flow. The equations of vorticity and energy transport were solved to determine the effect of the added vorticity. Their calculations revealed that the thermal boundary layer was much more sensitive to the external vorticity than the hydrodynamic boundary layer. The theory also predicted the existence of a neutral scale, which is about 2.6 times the Hiemenz boundary layer thickness, where amplification by stretching is exactly balanced by viscous dissipation. Only vorticity of larger scale would experience net amplification while smaller scale vorticity would be attenuated.

Rigby and VanFossen (1991) investigated the effect of a similar spanwise sinusoidal variation in velocity on a cylindrical leading edge of a semi-infinite flat plate. They hypothesized that a minimum level of vorticity must be supplied to the leading edge for a vortex to form. It was found that the introduction of a spanwise variation into the freestream always caused an increase in the spanwise averaged heat transfer coefficient. The percentage increase in the heat transfer coefficient was found to be substantially greater than the freestream disturbance expressed as a percentage of freestream velocity. For example, a 0.04 disturbance with a wavelength of 0.4 times the leading edge radius located 9 radii upstream of the leading edge resulted in an increase in heat transfer coefficient of 18 percent above the two-dimensional case.

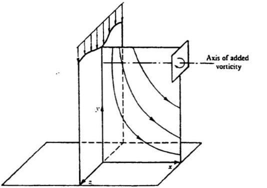

Figure 2.4 Velocity Profile with Superimposed Sinusoidal Variation

(Sutera et al., 1963)

VanFossen and Simoneau (1985) employed a combination of flow visualization using the smoke-wire technique and thermal visualization using liquid crystals to demonstrate the relation between vortex pairs and the spanwise heat transfer distribution. An array of parallel wires was installed upstream of the model leading edge to generate vortex pairs. The simultaneous flow and thermal visualization showed that the regions of highest heat transfer were between the vortex pairs as shown schematically in Figure 2.5. In this region, the induced velocity from adjacent vortex pairs is directed towards the cylinder surface.

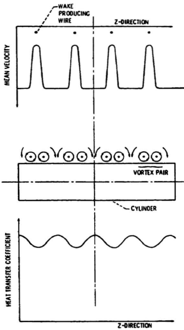

Figure 2.5 Spatial Relation between Wires, Vortex Pairs and Heat Transfer (VanFossen and Simoneau, 1985)

Van Fossen et al. (1995) used five different turbulence generating grids (four were square mesh, biplane grids made from square bars and the fifth grid was an array of fine parallel wires perpendicular to the model spanwise direction) in an attempt to correlate turbulence parameters and stagnation region heat transfer. The correlation developed by the study fit the data of the four square mesh grids, but under-predicted the heat transfer augmentation caused by the grid of parallel wires. It was concluded that the augmentation was also a function of the isotropy of the turbulent flow field as the turbulence generated by parallel wires had vortex lines dominating in one direction in comparison with grids of square mesh. The results indicate that turbulence with the majority of its vorticity oriented normal to the freestream and normal to the axis of the leading edge could have better interaction with the boundary layer to increase the heat transfer rate.

2.1.2 Empirical and Semi-Theoretical Correlation Models

Several empirical and semi-theoretical correlation models have been developed to predict stagnation region heat transfer in the presence of freestream turbulence. With increasing knowledge of turbulence and the physical mechanism of stagnation region heat transfer, the existing models need to be modified for more accurate prediction of heat transfer enhancement due to freestream turbulence. Heat transfer at the stagnation line is usually correlated with Reynolds number, freestream turbulence intensity and integral length scale. Since characterizing turbulence with these three parameters seems to be insufficient, the current correlation models are found to be experiment specific, not performing well with data from other researchers.

Frossling (1958) obtained a semi-theoretical solution for heat transfer in the stagnation region of a cylinder for a laminar freestream. The solution is valid in the laminar boundary layer region up to the separation point. Using an experimentally determined velocity distribution given by

$$U_\theta = \frac{3.6314}{2}\theta - \frac{2.1709}{8}\theta^3 - \frac{1.5144}{32}\theta^5 \tag{2.1}$$

Frossling obtained a solution for $Nu/\sqrt{Re_D}$, the Frossling number, as a function of the angular position from the stagnation point:

$$\frac{Nu}{\sqrt{Re_D}} = 0.9449 - \frac{0.510}{4}\theta^2 - \frac{0.5956}{16}\theta^4 \tag{2.2}$$

Smith and Kuethe (1966) suggested a semi-empirical theory for the augmentation of heat transfer at the stagnation point of a circular cylinder. By assuming the eddy viscosity to be proportional to the freestream turbulence and to the distance from the wall, they solved the two dimensional boundary layer equations to obtain an approximate linear relation between $Nu/\sqrt{Re_D}$ and $Tu\sqrt{Re_D}$. Experimental data for $Tu\sqrt{Re_D} < 20$ agreed satisfactorily with the theory, but deviated significantly at higher values of $Tu\sqrt{Re_D}$. The data also indicated an additional Reynolds number effect, especially at low values which they expressed as:

$$\frac{\left[\left(\frac{Nu}{\sqrt{Re_D}}\right) - 1\right]}{Tu\sqrt{Re_D}} = f(Re_D) \qquad (2.3\ a)$$

with

$$f(Re_D) = 0.0277[1 - exp(-2.9 \times 10^{-5}\ Re_D)] \qquad (2.3\ b)$$

It must also be noted that at Tu=0, the theory predicted $Nu\ \sqrt{Re_D}$ =1.00 rather than Frossling's value of 0.945. Equation 2.3 implies a linear relation between the stagnation point Fr and the freestream turbulence level for a constant Reynolds number. However, experimental data from later studies showed that Fr was not a linear function of turbulent intensity at higher turbulence intensities. The incorrect assumption of a linear relation could be due to the limited range of Tu, up to 6 percent, considered by Smith and Kuethe.

Kestin and Wood (1971) and Lowery and Vachon (1975) also used the parameter $Tu\sqrt{Re_D}$ to correlate the stagnation line heat transfer data. Kestin and Wood obtained a correlation for the Frossling number at the stagnation point in the range 0< $Tu\sqrt{Re_D}$ <40 by forcing the curve to pass through $Nu\ \sqrt{Re_D}$ =0.945 at $Tu\sqrt{Re_D}$ =0:

$$\frac{Nu}{\sqrt{Re_D}} = 0.945 + 3.45\left[\frac{Tu\sqrt{Re_D}}{100}\right] - 3.99\left[\frac{Tu\sqrt{Re_D}}{100}\right]^2 \qquad (2.4)$$

Lowery and Vachon (1975) extended the range of $Tu\sqrt{Re_D}$ to 64 and did not force their curve to pass through the Fr=0.945 for Tu=0. They found that the maximum deviation of any data point from their curve was 10.5 percent and that 87 percent of the data points were within 6.1 percent of the curve. Their correlation is given by:

$$\frac{Nu}{\sqrt{Re_D}} = 1.010 + 2.624\left[\frac{Tu\sqrt{Re_D}}{100}\right] - 3.070\left[\frac{Tu\sqrt{Re_D}}{100}\right]^2 \tag{2.5}$$

Lowery and Vachon concluded that disagreement between Equations 2.4 and 2.5 could be due to the difference in the test range of Reynolds number. The correlation of Equation 2.4 significantly over-predicts Nu when $Tu\sqrt{Re_D}$ becomes greater than 20. Daniels and Schultz (1982) found that heat transfer at the leading edge of a turbine blade was within 10% of the value predicted by Equation 2.5. However, experimental data from other studies show that Equation 2.5 is only valid for $Tu\sqrt{Re_D}$ from 0 to 40, but under-predicts Nu when $Tu\sqrt{Re_D}$ becomes greater than 40.

VanFossen et al. (1995) developed a correlation model for the stagnation point heat transfer by incorporating the integral length scale in addition to Reynolds number and turbulence intensity:

$$\frac{Nu}{\sqrt{Re_D}} = 0.008[Tu\, Re_D^{\,0.8}(\frac{\lambda_x}{D})^{-0.574}]^{0.5} + C \tag{2.6}$$

where the constant C is Fr at zero turbulence intensity.

Yeh et al. (1993) proposed a correlation model for the heat transfer at the stagnation point of a gas turbine blade based on the parameter developed by VanFossen et al. (1995). They modified the correlation model by changing the constants and exponents in order to best fit their experimental data. The correlation is given by:

$$\frac{Nu}{\sqrt{Re_D}} = 0.00732[Tu\, Re_D^{0.812} (\frac{\lambda_x}{D})^{-0.576}]^{0.5} + 0.945 \tag{2.7}$$

Dullenkopf and Mayle (1995) also proposed a correlation model (Eq. 2.8) in which they calculated the effective turbulence level based on the turbulence intensity and integral length scale of the freestream. The heat transfer Nusselt number was then given as a function of Reynolds number, Prandtl number and effective turbulence level.

$$Nu_a\, Pr^{-0.37} = 0.571 + 0.01 Tu_\lambda \tag{2.8}$$

where

$$Tu_\lambda = \frac{Tu_a \lambda_x^{0.5}}{(1 + 0.004\lambda_x^2)^{5/12}}$$

$$Nu_a = Nu_D / \sqrt{a_1\, \mathrm{Re}_D}$$

$$Tu_a = Tu\sqrt{\mathrm{Re}_D / a_1}$$

a_1 is a constant which may vary from 2.4 to 4 depending on the strain rate of freestream approaching the leading edge.

The above models are found to be experiment specific to varying degrees. While one can correlate data from the same experiment to a satisfactory level of accuracy, there are significant discrepancies when compared with other experimental data (see Figure

2.6). Wang et al. (1999) also showed that current correlation models did not fit well for turbulence with extremely large scales, i.e. $\lambda_x D$ of about one.

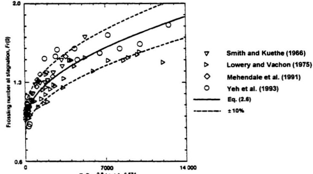

Figure 2.6 Comparison of Prediction by Eq. 2.6 with other Data (VanFossen et al., 1995)

Furthermore, previous attempts to formulate correlation models are based on isotropic turbulence generated by mesh grids. These models under-predict the stagnation line heat transfer for freestream turbulence with vortex lines in specific orientation (VanFossen et al., 1995). Therefore, the parameters used in current models are found to be insufficient to characterize the freestream turbulence. Vortical structure and vorticity characteristics are believed to play important roles in stagnation region heat transfer, and inclusion of these parameters in correlation models should lead to more robust and reliable models.

2.1.3 Predictions by Computational Methods

Computational techniques have been increasingly employed to estimate heat transfer on a bluff body in an external flow. There have been several numerical studies on gas turbine blade heat transfer using both Direct Numerical Simulations (DNS) and turbulence modeling. Since DNS is still a research tool and the Reynolds numbers handled by DNS are well below that of most applications (Kasagi and Iida, 1999), this section only reviews computational methods which use turbulence modeling. In most early attempts, heat transfer was estimated using a boundary layer analysis, where the flow field outside the boundary layer is approximated from inviscid codes and the momentum and energy equations are solved for the boundary layer. However, the inability to calculate heat transfer beyond the separation point prevented the boundary layer equation techniques from being widely used. For the case of stagnation region heat transfer, the boundary layer analysis cannot predict heat transfer at the leading edge well due to poor grid resolution in the very thin boundary layer at the leading edge. In addition, the heat transfer prediction in the leading edge region with boundary layer analyses may be in error, because of the necessity of modeling freestream turbulence (Boyle, 1991). Alternatively, the heat transfer can be calculated using a Navier-Stokes analysis, which solves the entire flow field. The Navier-Stokes analysis, however, needs more computational resources than boundary layer analysis. This is currently the most widely used analysis by industries and researchers due to the rapid increase of computing power. Accuracy of heat transfer prediction by computational techniques generally depends on:

(i) governing equations (simplified Navier-Stokes, thin-layer or parabolized, or full Navier-Stokes);

(ii) choice of turbulence and heat flux models;

(iii) computational techniques (different methods of finite volume, finite element and finite difference); and

(iv) grid resolution.

Boyle (1991) computed the heat transfer distributions on seven turbine vane and blade geometries using a quasi-three dimensional thin-layer Navier-Stokes analysis. The turbulent Prandtl number model proposed by Kays and Moffat (1975) and modified Baldwin-Lomax turbulent eddy viscosity model were used in the study. The predicted results for a turbine stator are given in Figure 2.7 for a laminar freestream and a freestream turbulence intensity of 8.3 percent. When freestream turbulence was imposed, significant errors arose in the stagnation region, and this was found to be true for other blade geometries. In order to improve the heat transfer prediction in the leading edge region, the calculations were repeated using turbulence models proposed by Smith and Kuethe (1966) and Forrest (1977). Boyle (1991) concluded that the Forrest model gave the best results for the stagnation region.

Ameri et al. (1992) computed heat transfer rates on two turbine blades by solving the two-dimensional, compressible, thin-layer Navier-Stokes and energy equations. The Baldwin-Lomax algebraic model and the q - ω low Reynolds number two-equation turbulence models were used, and the turbulent Prandtl number was assumed to be 0.9 for the heat flux calculations. There is a significant discrepancy between the experimental and predicted heat transfer in the stagnation region (Figure 2.8), implying that the present turbulence models are not suitable for stagnation point heat transfer.

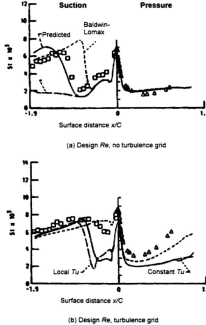

Figure 2.7 Predicted Stanton Number Distribution for a Turbine Stator

(Boyle, 1991)

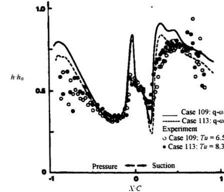

Figure 2.8 Heat Transfer Coefficient on a Vane (Ameri et al., 1992)

Larsson (1997) used a two-dimensional full Navier-Stokes solver to calculate the external heat transfer on a turbine cascade. Heat transfer results were obtained with two low-Reynolds k-ε and two k-ω turbulence models assuming turbulent Prandtl number of 0.9. At four percent freestream turbulence level, the prediction of stagnation region heat transfer by all turbulence models was significantly higher than experimental data. Estimation of stagnation region heat transfer did not improve even after turbulence models were modified as suggested by Kato and Launder (1993).

With increasing computing power, analysis with full Navier-Stokes and energy equation solvers is expected to dominate current and future computational studies on turbomachinery heat transfer. However, prediction of stagnation region heat transfer cannot be accurate unless reliable turbulence and heat flux models are formulated. A better understanding of the stagnation region heat transfer and turbulence characteristics is essential for the development of appropriate turbulence and heat flux models.

2.2 Review of Turbulence with Coherent Structures

While momentum and heat transport mechanisms in turbulent flows have been studied for many decades, the dynamics of turbulent flows are still not fully understood. Recent advances in DNS have provided an excellent insight into turbulence dynamics and transport mechanisms for turbulent flows, especially at low Reynolds numbers (Kasagi and Iida, 1999). An important contribution of DNS has been to provide a better understanding of the role of coherent vortical structures on turbulent flows in momentum and heat transport mechanisms. A coherent motion or a coherent structure is defined as a three-dimensional region of the flow over which at least one fundamental flow variable (velocity component, density, temperature, etc.) exhibits significant correlation with itself, or with another variable, over a range of space and/or time that is significantly larger than the smallest local scales of the flow (Robinson, 1991). While energy dissipation of a turbulent flow is associated with the smallest scales of the flow, larger coherent eddies are responsible for transporting momentum and heat across the flow (Tennekes and Lumley, 1972; Souza et al., 1999). Several boundary layer studies have shown that breaking the large scale coherent motion close to the wall using various means could result in a skin friction reduction (Jacobson and Reynolds, 1993; Moin and

Bewley, 1994; Ho and Tai, 1996). Knowledge of turbulent coherent structures and their roles in transport mechanisms is essential in the study of turbulent heat transfer.

The kinematics of coherent structures has been investigated using several techniques: flow visualization, statistical analysis techniques, e.g. wavelet analysis and conditional-sampling, and numerical simulation, e.g. DNS and large-eddy simulation (LES). The studies of turbulence with coherent structures are reviewed in this section, focusing on the turbulent wake behind a circular cylinder and coherent motions in the boundary layer, because of substantial research work in these areas. Since the current study had an intention to use turbulence generating grids of parallel rods, the characteristics of vortical structures in the wake of a circular cylinder and their evolution with downstream distance would be useful for this study. A review of coherent structures in boundary layers, and their role in transport mechanisms and interaction with uniform freestream, should give certain knowledge on the physics of the effect of the turbulent freestream on the laminar boundary layer of the current study.

2.2.1 Wake Behind a Circular Cylinder

Vortex shedding and the wake characteristics of a circular cylinder are dependent on Reynolds number, and different flow regimes can be defined (Roshko, 1992; Williamson, 1996b; Zdravkovich, 1997). The various vortex dynamics phenomena of the wake for each regime with increasing Reynolds number are briefly discussed below.

(i) Steady Laminar Wake (Re_d < 49)

Up to a Reynolds number of about five, there is no flow separation. Flow separation initiates at Re_d of around five, and up to Re_d around 49, the wake comprises a steady recirculation region of two symmetrically placed vortices on each side of the wake (Figure 2.9.a). The recirculation region grows with the Reynolds number, and the flow remains laminar in both near wake and far wake in this flow regime (Williamson, 1996b).

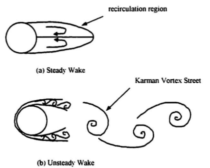

Figure 2.9 Flow Regimes and Recirculation Region in the Cylinder Wake (Williamson, 1996b)

(ii) Periodic Laminar Regime (Re_d = 49 to 140-194)

The elongated recirculation region in the near-wake becomes unstable as Re_d increases. The shear layers, which are separated from the cylinder, roll up and the final product is a staggered array of laminar eddies known as Karman vortex street or Karman-

Bernard eddy street (Zdravkovich, 1997) as given in Figure 2.9 (b). The flow in the wake in this regime is still laminar with primary vortices parallel to the cylinder. Taneda (1959) and Matsui and Okude (1980) claimed from their experimental data the formation of secondary eddy street beyond $x/d = 50$ was present in this flow regime apart from the Karman vortex street.

(iii) Wake-Transition Regime ($Re_d \sim 190$-260)

Transition to turbulence commences in the wake in this regime due to increasing instability of the Karman vortices. The transition regime is associated with two discontinuous changes in the wake formation (Williamson, 1996b). At $Re_d \approx 180$-194, the inception of vortex loops can be seen along with the formation of streamwise vortex pairs due to the deformation of primary vortices as they are shed, at a wavelength of around 3-4 diameters (Williamson, 1988; Zhang et al., 1995). The second discontinuity, which occurs over a range of Re_d from 230 to 250, comprises finer-scale streamwise vortices, with a spanwise length scale of around one diameter. The prominent characteristic of this flow regime is the evidence of streamwise vortex structures along with the primary vortices. The large intermittent low-frequency wake velocity fluctuations are present due to the vortex dislocations in this transition regime (Williamson, 1992). At $Re_d \approx 260$, the three-dimensional streamwise vortex structures in the near wake become increasingly disordered (Williamson, 1996a; Prasad and Williamson, 1995).

(iv) Shear-Layer Transition Regime ($Re_d = 1{,}000$ to $200{,}000$)

In this flow regime, transition occurs in the free shear layer separated from the cylinder, and the wake is turbulent. The transition region moves with increasing Re_d

along the free shear layers towards the separation. Three-dimensional structures on the scale of shear layer thickness are expected to develop in this regime as well as three-dimensionality on the scale of the Karman vortices (Wei and Smith, 1986; Williamson et al., 1995; Williamson, 1996b). The changes in character of the vortex shedding are relatively small over a large range of Re_d, and the streamwise vortex scales are almost independent of Reynolds number within this regime (Williamson, 1996b).

The presence of primary vortices are strongly evident up to $x/d = 50$, and the primary vortices become dislocated and cannot be precisely traced beyond $x/d > 50$ in this flow regime (Zdravkovich, 1997). However, coherent large scale structures were reported in the far wake in a few studies (Antonia et al., 1987, Bisset et al., 1990, Zhou et al., 1999). Furthermore, large scale secondary vortical structures, called double rollers in the literature (Payne and Lumley, 1967; Corke et al., 1992), are found in the far wake ($x/d > 100$) of the circular cylinder.

(v) Boundary-Layer Transition Regime ($Re_d > 200{,}000$)

The transition region in the shear layer transition regime moves towards the separation point with an increase in Reynolds number as mentioned earlier, and finally, the boundary layer on the surface of the cylinder itself becomes turbulent. It is generally assumed that the downstream wake would be fully turbulent, and it is not expected that coherent vortices would be observed (Williamson, 1996b). Roshko (1961), however, claimed that periodic vortex shedding was strongly in evidence even in this flow regime.

2.2.2 Coherent Structures and Transport Mechanism in Boundary Layers

In a turbulent boundary layer, kinetic energy from the freestream is converted into turbulent fluctuations and then into internal energy by viscous action. This process is self-sustaining in the absence of strong stabilizing effects. The coherent structures in a turbulent boundary layer are believed to be responsible for this self-sustaining (production and dissipation) of turbulence and transport mechanism in the boundary layer (Kline and Robinson, 1989; Robinson, 1991).

A turbulent boundary layer can be divided into different regions starting from the wall: the sublayer, buffer region, log region and wake or intermittent region. The sublayer and buffer regions are referred to as the inner region, and the combined log and wake regions are known as the outer region. The most dominant coherent structures in a turbulent boundary layer are horseshoe, hairpin and streamwise vortices (Head and Bandyopadhyay, 1981; Jeong et al., 1997), and these structures play different roles in the transports of momentum and heat. The quasi-streamwise vortices near the wall could 'pump-out' mass and momentum from the wall (Robinson, 1991). The majority of the turbulence production in the entire boundary layer occurs in the buffer region during intermittent, violent outward ejection of low-speed fluid and during inrushes of high-speed fluid at a shallow angle toward the wall. This phenomenon is known as bursting. Outward movement, away from the wall, of the heads of horseshoe and hairpin vortices is closely associated with bursting (Smith and Walker, 1997; Carpenter, 1997).

In the outer region, three-dimensional bulges on the scale of the boundary layer thickness form in the turbulent/non-turbulent interface. Deep irrotational valleys occur on the edges of the bulges, through which freestream fluid is entrained into the turbulent region (Robinson, 1991). The intermittent region of the boundary layer is dominated by large-scale motions (also called entrainment eddies). Entrainment of potential fluid occurs in valleys in the turbulent/non-turbulent interface that exit at the edges of bulges (Spina and Smits, 1987; Antonia et al., 1989; Robinson, 1990; Robinson, 1991). Based on the knowledge of turbulent boundary layer, it may be concluded that the motion of large scale eddies, or eddies with integral length scale, could play an important role in the transport mechanisms at the turbulent/non-turbulent interface of a turbulent freestream and laminar boundary layer of the stagnation region. Using the integral length scale of turbulence (Yardi and Sukhatme, 1978; Yeh et al., 1993; VanFossen et al., 1995; Wang et al., 1999) in correlation models to determine the influence of freestream on the stagnation heat transfer seems to be justified.

2.3 Vorticity Characteristics and Measurements

2.3.1 Vorticity Dynamics in Turbulent Flows

Vorticity can be considered the organizing principle of turbulent motion (Wallace, 1986) and is the feature that distinguishes turbulence from other random fluid motions like ocean waves and atmospheric gravity waves (Tennekes and Lumley, 1972). Vorticity is defined, in Cartesian tensor notation, as:

$$\Omega_i = \varepsilon_{ijk} \frac{\partial U_k}{\partial x_j} \tag{2.9}$$

where ε_{ijk} is the alternating tensor and U_j is the velocity in the j direction.

At each point in the flow field, the motion of a spherical fluid particle can be decomposed into translation, expansion and rotation. The vorticity can be interpreted as twice the instantaneous solid body-like rotation rate of the fluid particles or, more precisely, twice the rotation rate of particles along principal axes in the fluid where there exists no shear deformation (Panton, 1984). Alternatively, vorticity can be defined as the circulation per unit area of surface perpendicular to the vorticity field.

Vorticity plays an important role in the dynamics of turbulence. There are some distinct advantages to describing the dynamics of turbulent motion in terms of vorticity. The equation of motion in terms of vorticity is:

$$\frac{\partial \Omega_i}{\partial t} + U_j \frac{\partial \Omega}{\partial x_j} = \Omega_j \frac{\partial U_i}{\partial x_j} + \upsilon \frac{\partial^2 \Omega_i}{\partial x_j \partial x_j} \tag{2.10}$$

The total rate of change of vorticity, local plus convection, is due to the deformation of the vortex lines and viscous diffusion of vorticity (two terms on the right hand side of Eq. 2.10). Since the diffusion of vorticity is a relatively slow process, it is possible to ignore the last term of Equation (2.10) in many applications. Therefore, a change in the vorticity of a particle is primarily due to the distortion caused by the straining of the vortex lines. Vorticity dynamics must play a prominent role in heat transfer at the leading edge because of the vorticity amplification due to vortex stretching.

2.3.2 Measurement Techniques

There have been significant advances in the measurement of vorticity in turbulent flows over the last few years (Wallace and Foss, 1995). The techniques can be generally classified into thermal anemometry and optical anemometry.

2.3.2.1 Thermal Anemometry

A hot-wire anemometer is a transducer that senses the changes in heat transfer from a small, electrically heated sensor exposed to fluid motion. There are two modes of operation of a hot-wire anemometer depending on the way the sensor heating current is controlled. In the constant-current mode, the current to the sensor is kept constant and variations in sensor resistance caused by the flow are measured by monitoring the voltage drop variations across the sensor. In the constant-temperature mode, the wire is placed in a feedback circuit which maintains the wire at a constant resistance and hence constant temperature. Fluctuations in the cooling of the wire are seen as variations in wire current. A simple constant temperature anemometer is shown in Figure 2.10. The constant-temperature mode is used for velocity measurements almost exclusively, because it exhibits considerably higher frequency response than the constant-current mode (Lekakis, 1996).

The choice of the sensor diameter involves a compromise between a small value to improve the signal-to-noise ratio at high frequencies, to increase frequency response and spatial resolution, and to reduce flow interference and end conduction losses, and a large value to increase wire strength and reduce its contamination due to particles in the fluid. An optimum diameter is usually considered to be in the range 2-5 μm (Lekakis, 1996). The sensor length should be short to maximize spatial resolution and to minimize aerodynamic loading and long to minimize end conduction losses and to provide a more uniform temperature distribution. The best compromise is usually obtained when the length-to-diameter ratio is approximately 200 (Ligraani and Bradshaw, 1987; Turan and Azad, 1989).

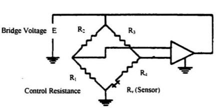

Figure 2.10 Electrical Circuit of a Constant-Temperature Anemometer (Lekakis, 1996)

A vorticity probe must have the capability to measure two velocity gradients simultaneously, ideally at a point. However, with multi-sensor probes, thermal anemometry can provide only an approximation. For example, $\partial u/\partial y$ at a point in the flow is obtained from $\Delta u/\Delta y$ by using two parallel wires separated by Δy. Therefore, spatial resolution considerations are important since wires spaced far apart will not reflect the required point property, and wires spaced too close could lead to inaccuracy due to aerodynamic disturbances between wires. In addition, the temporal resolution has to be carefully considered to obtain good measurements.

Spatial and Temporal Resolutions

Wyngaard (1969) analyzed the response of a vorticity probe by analytically subjecting it to the three-dimensional velocity spectrum given by Pao (1965) and assuming isotropy. He recommended that sensor length should not be more than 3.3η (where η is the Kolmogorov length scale), and found that separation of two parallel wires by $S\ \eta \approx 3.3$ could measure about 85% of the variance of true velocity gradient.

Antonia et al. (1993) tested Wyngaard's parallel sensors analysis by using data from two direct numerical simulations (DNS) at the center line of a turbulent channel flow (Kim et al., 1987; Kim, 1989). The finite difference approximation $\Delta u\ \Delta y$ was defined as measured fluctuating velocity gradient and the true gradient $\partial u\ \partial y$ was obtained by spectral differentiation using Chebychev polynomials. The ratio of the variance of the measured gradient to the true gradient decreases with increasing sensor separation as shown in Figure 2.11, where Δy^* is the separation between two wires normalized by η.

Ideally the separation between the two parallel wires should be as small as possible; however, there is a trade-off to minimize aerodynamic disturbance between the wires. Experimental data of measured to true velocity gradients are compared with DNS data in Figure 2.12, where the solid line represents Wyngaard's analysis with DNS spectrum, against Δy^*. It is clear from Figure 2.12 that the wire separation must be greater than 2η to avoid interference.

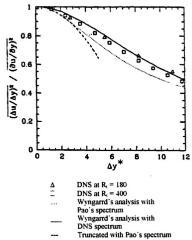

Figure 2.11 Attenuation of Measured Velocity Gradient Due to Separation Distance

(Antonia et al., 1993)

Wallace and Foss (1995) concluded that the optimum sensor separation for determining velocity gradients was about 2-4η when both resolution and accuracy constraints were considered. Zhu and Antonia (1995) studied the spatial resolution of a four X-wire vorticity probe, where the X-wires form sides of a box. They determined that streamwise velocity derivatives were more attenuated with separation between wires than the lateral derivatives, and the streamwise vorticity was less attenuated than the lateral vorticity component. Mi and Antonia (1996) measured the lateral vorticity components using two X-wires separated in the appropriate direction in the turbulent intermediate wake. They determined that the separation between the two X-wires should not be smaller than 3η.

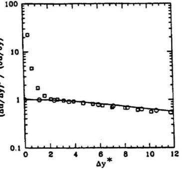

Figure 2.12 Dependence of Experimental (□) and DNS (O) Measured to True Velocity Gradients on Wire Separation Distance (Antonia et al., 1993)

Ideally, sampling of the sensor signals of probes designed to measure vorticity components should temporally resolve a frequency, $f_s \approx U/(3\eta)$, where U is the local mean velocity. This requires that the sampling frequency of f_s be at least twice the Kolmogorov frequency f_k in order to satisfy the Nyquist criterion (Wallace and Foss, 1995).

Performance of Vorticity Probes

Kovasznay (1950, 1954) proposed a geometrical configuration of hot wires forming the legs of a Wheatstone bridge (Figure 2.13) and later modified by Kastrinakis et al. (1979) to measure vorticity. The probe consists of four slanted wires forming two X-wires. While a pair of slanted wires was used as an X-wire to measure a lateral velocity component (V or W), the other two slanted wires measured the streamwise velocity (U) to estimate the lateral velocity derivatives ($\partial U/\partial y$ or $\partial U/\partial z$). However, the optimum sensor length to diameter ratio and the geometry of this type of vorticity probe lead to a large distance between X-wires, and vorticity components measured with this type of probe can be in serious error (Wallace and Foss, 1995).

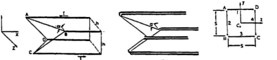

(a) (b)

Figure 2.13 (a) Kovasznay-Type Vorticity Probe and (b) Modified Version (Park and Wallace, 1993)

Foss (Foss, 1981, 1994; Foss et al., 1987; Foss and Haw, 1990a, 1990b) developed and refined an array of four hot-wire sensors to measure the cross-stream vorticity components, Ω_y and Ω_z (Figure 2.14). Antonia & Rajagopalan (1990) and Zhou and Antonia (2000) used a similar vorticity probe to measure ω_y and ω_z in the wake of a circular cylinder and a square mesh grid, respectively. The spatial separation between the pair of parallel wires was about 3.5η and that between the two wires in the X-array was about 5.1η. Rajagopalan and Antonia (1993) used a compact version of the vorticity probe in a turbulent boundary layer. The separations between the parallel wires ranged from 1.5η to 6η and separation between the X-wires was 1.8η to 7.4η. The measured rms vorticity ω_z was in reasonable agreement with the DNS results of Spalart (1988).

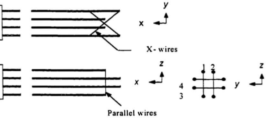

Figure 2.14 Compact Four-Sensor Cross-Stream Vorticity Probe (Foss and Haw, 1990b)

A vorticity probe of four sensors can only measure a single component of vorticity at a given time. Several attempts have been made to measure two and three components of vorticity simultaneously with multi-sensors probes: a five-sensor probe for two vorticity components (Eckelmann et al., 1977), a six-sensor probe for two vorticity components (Kim, 1989; Kim and Fiedler, 1989), a nine-sensor probe for three vorticity components (Wassman and Wallace, 1979; Balint et al., 1991; Vukoslavêevié et al., 1991; Hokan, 1993), and a twelve-sensor probe (Tsinober et al., 1992; Marasli et al., 1993; Vukoslavêevié and Wallace, 1996). Configurations of some multi-sensor probes are given in Figure 2.15. Although these multi-sensor probes can measure more than one vorticity component simultaneously, they have the following disadvantages:

(i) The greater number of hot-wires need more data acquisition resources and lead to higher level of uncertainty in signal interpretation;

(ii) Complex data reduction programs are required and agreements on computing procedures for a certain probe geometry, especially the nine and twelve-sensors probes, has not been obtained;

(iii) The more complex geometry and greater number of hot-wires widen the probe sensing volume leading to poor spatial resolution: unlike the four-sensor probes, the spatial resolution has not been studied satisfactorily.

2.3.2.2 Optical Anemometry

Two of the most widely used optical anemometry techniques are Laser Doppler Anemometry (LDA) and Particle Imaging Velocimetry (PIV). Both techniques measure the velocity of seeding particles, which must adequately follow the fluid motion. Apart from the spatial and temporal resolution constraints as in thermal anemometry, the constraints of density and size of particles are encountered in optical anemometry. The primary advantage of optical techniques is its non-intrusiveness to the flow.

Foss and Haw (1990b) found agreement between the thermal and optical anemometry methods for a mixing layer. Wallace and Foss (1995) compared thermal and optical anemometry measurements with DNS for a boundary layer and a mixing layer. In the boundary layer measurements, LDA and PIV data agreed better with DNS data than data from the hot-wires. The deviation of hot-wire data becomes larger close to the wall where the resolution problems of thermal anemometry are most severe. However, there was good agreement in the vorticity data with optical and thermal anemometry in the mixing layer where the spatial resolution problem is not as severe as in the near-wall region of a boundary layer.

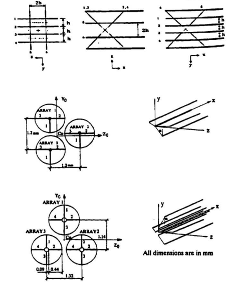

Figure 2.15 Schematic Diagrams of Multi-Sensor Probes (Wallace and Foss, 1996)

2.4 Summary

Heat transfer augmentation in the stagnation region due to freestream turbulence remains unsolved like many other transport mechanisms in turbulent flows. However, isolated influences of several turbulence parameters have been studied, and they were reviewed in this chapter. The existing empirical and semi-theoretical models as well as the attempts using computation techniques were examined. The laminar boundary layer in the stagnation region makes it difficult to predict the heat transfer accurately using existing turbulence models. The deficiency of existing empirical models seems to be the lack of incorporating the characteristics of turbulent coherent structures, which are believed to play a significant role in the turbulent transport mechanisms. This leads to the literature review on turbulence with coherent structures, focusing on the characteristics of the wake behind a circular cylinder and the turbulent boundary layer where a great deal of research has been performed. Although vorticity amplification has long been hypothesized to be the reason for the heat transfer augmentation in the stagnation region, very limited efforts to measure and incorporate vorticity into the correlation models have been made. Current vorticity measurement methods were reviewed in order to determine a suitable technique for the freestream turbulence. It was concluded that generating freestream turbulence with coherent vortical structures, and measuring and including the vorticity in characterizing the turbulence should result in a better description of freestream turbulence. Correlating these turbulence parameters with the stagnation region heat transfer should lead to a better understanding of the heat transfer mechanisms and the development of more robust empirical models.

Chapter III

Experimental Set-up and Data Reduction

3.1 Experimental Facilities

3.1.1 Wind Tunnel Configuration

The experiments were performed in an open circuit low speed wind tunnel shown schematically in Figure 3.1. The wind tunnel has a 1m × 1m test section and is over 20 m long. The roof of the tunnel is adjusted to maintain a zero pressure gradient along the test section.

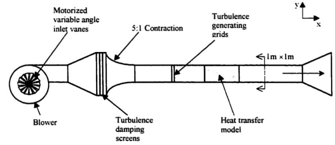

Figure 3.1. Schematic Diagram of the Wind Tunnel

A centrifugal blower driven by a 19 kW motor is used in the wind tunnel. The air passes through a screened diffuser and a large settling chamber with three single-piece precision screens. The air is accelerated into the test section through a 5:1 contraction.

The maximum freestream velocity in the test section is about 15 m/sec. The freestream turbulence intensity is less than 0.5% at all flow rates. The velocity in the test section is changed using motorized variable angle inlet vanes on the blower.

3.1.2 Heat Transfer Model

Figure 3.2a shows a schematic of the heat transfer model with a cylindrical leading edge to simulate the leading edge of a gas turbine vane. To minimize the flow blockage effect on the heat transfer, the cylindrical leading edge of 20.32 cm in diameter and 1m in height, which creates a flow blockage of 20 percent, was used. Photographs of the model in the wind tunnel are shown in Figure 3.2b. The leading edge is attached to a flat body 60 cm long. The after body is then streamlined with a long tapered tail in order to prevent the shift of the stagnation point due to vortex shedding at the end. The model is made of 0.635 cm thick Plexiglass to lower the conduction loss.

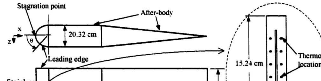

Figure 3.2a Schematic Diagram of Heat Transfer Model

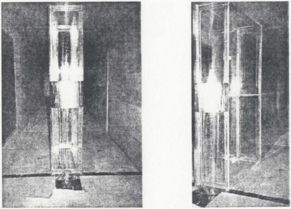

Figure 3.2b Photos of Heat Transfer Model

Nineteen strips of 0.005 cm-thick stainless steel foil are evenly distributed over the stagnation line at the center of the cylindrical leading edge, keeping the heat transfer region away from the boundary layers developed on the walls of the tunnel. Each strip is 15.24 cm long, 1.5 cm wide and separated from adjacent strips by a gap of 1 mm. The gaps between the strips are filled with super-glue and sanded until the surface is smooth and flush with the foil surface. The steel foils are connected in series, and a variable AC/DC transformer is used to supply power across the foils to obtain a constant heat flux surface at the leading edge. The voltage and current supply to the leading edge is measured using a multimeter with a resolution of 0.01 ampere and 0.01 volt. Six calibrated, 36-gauge T type copper-constantan thermocouples are attached to the underside of every foil strip on one half, i.e. $0° \leq \theta \leq 90°$ or ten strips, of the cylindrical leading edge. The thermocouples are evenly distributed in the middle portion of the strip in such a way that the distance between the edge of the strip and the nearest thermocouple is 3.25 cm as shown in Figure 3.2a. One strip on the other side of leading edge is also instrumented with six thermocouples in order to check the alignment of the model with the mean flow direction. The thermocouples are threaded through small holes drilled on the leading edge. Additional thermocouples are attached on the inner wall of the leading edge to estimate the conduction heat loss through the Plexiglass.

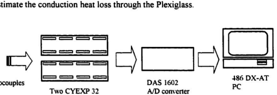

Figure 3.3 Data Acquisition for Heat Transfer Model

Data from the thermocouples is acquired via two CYEXP 32 Multiplexors (Cyber Research) connected in series (Figure 3.3). Analog outputs from the Multiplexors are digitized using a DAS 1602 A/D converter (Cyber Research) and data logging is controlled by the "Labtech Buildtime" software package.

3.1.3 Turbulence Generating Grids

Freestream turbulence was generated using grids of different size parallel rods in both horizontal and vertical orientations. The grids with parallel rods were expected to produce freestream turbulence with well-defined vortex lines. Two C channels were used to hold the parallel rods as shown in Figure 3.4. For the grid of horizontal parallel rods, the channels were attached to the vertical sides of the wind tunnel, and in the case of vertical rods, the channels were fixed to the floor and roof of the wind tunnel. The rods and spacers were held in place in the channels by guide plates. The channels allow the use of different length spacers and different rod sizes providing the flexibility of grid arrangement to obtain a reasonable range of turbulence parameters.

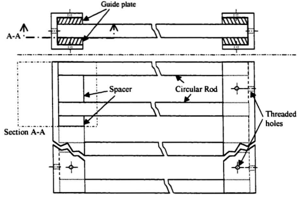

Figure 3.4 C-Channels Arrangement for Parallel Rods

The orientations of rod-grids with respect to the heat transfer model are shown in Figure 3.5. Hereafter, the grid with the rods perpendicular to the stagnation line will be called the grid in perpendicular orientation, while the grid with the rods parallel to the stagnation line will be called the grid in parallel orientation. The rods in both grid orientations are perpendicular to the streamwise direction. Three grids with rod diameters of 2.86 cm (1-1/8"), 1.59 cm (5/8") and 0.95 cm (3/8"), and 50% open area were used. The design of the grids was based on the turbulence intensity levels, geometrical similarity among the grids, the test-section length of the tunnel and uniformity of turbulent flow over the heat transfer surface.

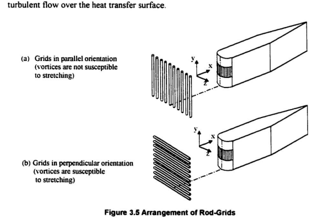

Figure 3.5 Arrangement of Rod-Grids

3.1.4 Hot-wire Anemometers and Data Acquisition Systems

Single, X-wire and four-wire vorticity probes were used to measure the turbulence characteristics of the freestream. The vorticity probes were designed and built in-house. The vorticity probe consists of four hot-wires, and the configuration of wires is adopted from the design developed by Foss and his coworkers (Foss, 1981, 1994; Foss et al., 1987; Foss and Haw, 1990a, 1990b). A schematic diagram of the vorticity probe is shown in Figure 3.6.

Each sensor is made of a 5 μm platinum-plated tungsten wire. The effective length of the hot-wires is about 1.5 mm. The parallel wires are separated by 1.2 mm, and the distance between the two X-wires is 1.5 mm. The vorticity probe is attached to a specially designed traversing mechanism, which consists of a digital height gauge and a digital caliper, so that the probe has two degrees of freedom with a minimum linear division of 0.01mm. The traverse is installed on rails mounted on the roof of the wind tunnel.

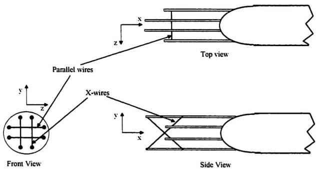

Figure 3.6 Four-Wire Vorticity Probe

Each sensor of the hot-wire probe is connected to a DANTEC 55M01 standard bridge, and is operated in the constant temperature mode. The hot wire signals are digitized using a 16 channel 12 bit Keithley 570 System Analog to Digital (A/D) converter, interfaced to a Pentium 100 personal computer. The hot-wire anemometer system is shown schematically in Figure 3.7. The frequency response of the circuit was determined by a standard square-wave test, and found to be 30 kHz. Both the oscilloscope and spectrum analyzer are dual channel and can accept signals from any two sensors.

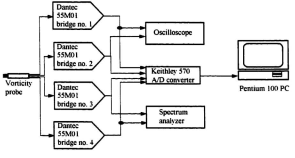

Figure 3.7 Instrumentation of Vorticity Probe

3.2 Experimental Procedures, Data Reduction and Uncertainty Analysis

Each grid was placed at five different positions, 25*d* to 125*d*, upstream of the stagnation line of the model. The wind tunnel was operated at freestream velocities of 5, 8 and 10.5 m/s, corresponding to Re_D of 67,750, 108,350 and 142,250, for each grid position. Velocity measurements for the hot-wire calibrations were made using a 8360-

M-GB VelociCalc® Plus TSI air velocity meter, which has a resolution of 0.01 m/s. The leading edge was heated to about 45°C for each heat transfer test. The thermocouple readings were monitored every 15 minutes until steady state conditions were reached. Three sets of temperature distributions and voltage and current flow of the DC power supply unit were recorded after steady state was attained. Each data set of temperature distributions contains 180 data points (data acquisition rate of 1.5 Hz for 2 minutes) for each thermocouple.

The single, X-wire and four-wire vorticity probes were used to measure the freestream turbulence characteristics at several positions downstream of the rod-grids in perpendicular orientation in the absence of the heat transfer model. Two sets of X-wire data, one for the simultaneous measurement of the velocity components in X and Y directions and another in X and Z directions (see Figure 3.2), were obtained by rotating the X-wire probe 90°. The spanwise fluctuating vorticity components, ω_z and ω_y, were measured using the vorticity probe. The two spanwise fluctuating vorticity components were obtained separately by rotating the vorticity probe 90°. The sampling frequency of the hot-wire measurements ranged from 20 to 30 kHz.

3.2.1 Heat Transfer Estimations

Electrical energy supplied to the series of stainless steel foils is lost to the freestream by convection, to the surroundings by radiation, and to the leading edge of the model by conduction. The Nusselt number was estimated as follows:

$$Nu(\theta) = \frac{Q_{conv} D}{A[Tw(\theta) - T_{\infty}]k} \tag{3.1a}$$

where

$$Q_{cov} = Q_{in} - Q_{rad} - Q_{cond} \tag{3.1b}$$

$$Q_{in} = Vo \times I \tag{3.1c}$$

$$Q_{rad} = \varepsilon \sigma A (Tw_{avg}^{4} - T_{sur}^{4}) \tag{3.1d}$$

$$Q_{cond} = k A C_f (Tw_{avg} - Tw_{inner}) \tag{3.1e}$$

Energy input to the leading edge, Q_{in}, was obtained from the supply voltage, Vo, and current flow, I. An estimation for the radiation heat loss, Q_{rad}, was made by assuming gray body radiation to black surroundings and an emissivity of 0.17 for the stainless steel foil. The conduction heat loss, Q_{cond}, through the leading edge wall was computed from the measured temperature difference between the outer and inner surface of the leading edge wall. Thermal conductivity of the leading edge was 0.201 W/m-K as provided by the manufacturer. The correction factor C_f was determined from the three-dimensional conduction heat transfer model which is given in Appendix A.

The average of 180 data points was obtained for each thermocouple. The spanwise temperature distribution of the stainless steel strips was found to be fairly constant and within the uncertainty of the temperature measurements. The spanwise variation of the temperatures from the six thermocouples (T1-T6) is about two percent for all heated strips (Figure 3.8), where strip no. 1 is on the stagnation line. Since the thermocouples are located in the middle portion of the stainless steel foils (see Figure 3.2a), the end conduction heat losses from the heated strips do not significantly influence the spanwise temperature distribution at the measured locations on the strips. Therefore, an average value of the six thermocouple readings is taken as the temperature $Tw(\theta)$ of a particular strip.

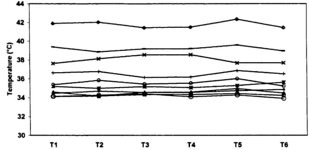

Figure 3.8 Spanwise Temperature Distributions of Heated Stainless Steel Strips (O, strip no. 1; □, 2; Δ, 3; ◊, 4; *, 5; O, 6; +, 7; ×, 8; -, 9; ◊, 10)

A number of test runs were performed with and without the grids to estimate the conduction heat losses. During these test runs, the spanwise temperature distributions of the heated strips and the temperatures outside the strips and on the inner surfaces were recorded. A three-dimensional finite difference scheme was then used to determine the total conduction heat losses taking into account the lateral end conduction heat losses. Correction factors were obtained for different freestream Reynolds numbers to estimate the conduction heat losses based on the average temperature difference between the heated outer surface and inner wall of the leading edge. Details of the three-dimensional finite difference scheme and the estimation of conduction heat losses are given in

Appendix A. In this experiment, radiation and conduction heat losses were on the order of 2 percent and 20 percent, respectively. Heat transfer tests were also performed without any grids to validate the heat transfer measurements. The stagnation line heat transfer Frossling numbers for the freestream with low turbulence intensity (0.5% for this study) ranged from 1.04 to 1.06 (Figure 3.9) for the Reynolds numbers of the study, and are in good agreement with the literature (Lowery and Vachon, 1975; Mehendale et al., 1991). As shown in Figure 3.9, off-stagnation line region ($\theta > 0$) heat transfer of the current study is in good agreement with the results of Mehendale et al. (1991), since both heat transfer models have the same geometry of cylindrical leading edge and flat plate after-body. The heat transfer results agreed with those of Lowery and Vachon (1975), who tested with a circular cylinder heat transfer model, up to $\theta \approx 40°$.

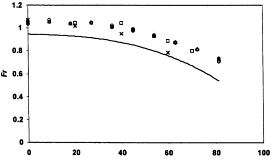

Figure 3.9 Distribution of Frossling Number in the Stagnation Region Without Turbulence Grids (◊, Re_D = 67,750; Δ, 108,350; ○, 142, 250; □, Mehendale et al. (1991); ×, Lowery and Vachon (1975); — Frossling Solution)

An uncertainty analysis was conducted using the methods of Moffat (1988). The uncertainty in Fr can be expressed as:

$$(Un_{Fr})^2 = (Un_{Nu})^2 + 0.25\,(Un_{ReD})^2 \tag{3.2}$$

where Un_{Fr} = Uncertainty in Fr (%)

Un_{Nu} = Uncertainty in Nu (%)

Un_{ReD} = Uncertainty in Re_D (%)

The uncertainty in Fr and the influencing variables with 95% confidence levels are given in Table 3.1 for both maximum and minimum freestream velocities. The definitions and sample estimations of bias and precision errors of variables are provided in Appendix B. Uncertainties in temperature were considered in estimating conduction heat loss, radiation heat loss and convection heat transfer. Uncertainties associated with leading edge diameter (D), thermal conductivity (k) and area (A) are assumed to be negligible since these values are based on the data specified by the manufacturers. The uncertainty in Fr is 3.92 percent and 3.67 percent for the minimum and maximum freestream Reynolds numbers, respectively.

3.2.2 Hot-wire Measurements

Hot-wires were calibrated using the 8360-M-GB VelociCalc® Plus TSI air velocity meter. About twenty data points were obtained with the freestream velocities covering the test range (5-10.5 m/s), and a sampling frequency of 20 Hz for 50 sec was used for calibration of the hot wires. Curve fitting with a third-order polynomial was performed to functionally relate the hot-wire signal (volts) and velocity (U) as given by Equation (3.3).

$$U(E) = a + b\,E + c\,E^2 + d\,E^3 \quad (3.3)$$

where U is the velocity reading of the TSI meter, and E is the hot-wire signal. The constants a, b, c and d were obtained by a least-squares curve fit to the data. Typical calibration curves for the single wire, X-wire and the vorticity probe are given in Appendix C.

Table 3.1 Experimental Uncertainty of Parameters in Estimating *Fr* (%)

Variable	Bias Error		Precision Error	
	Experimental Reynolds Number Range			
	Maximum	Minimum	Maximum	Minimum
Current I	0.18	0.26	0.53	0.51
Voltage Vo	0.06	0.08	0.20	0.21
Temperature difference ΔT	3.20	3.20	0.53	0.53
Conduction heat loss, Q_{cond}	4.60	4.60	0.75	0.75
Radiation heat loss, Q_{rad}	12.80	12.80	2.12	2.12
Convection heat Q_{cov}	1.61	2.10	0.55	0.60
Reynolds number Re_D	0.05	0.10	0.32	0.37
Frossling number Fr	3.58	3.83	0.79	0.82

3.2.2.1 Single Wire

The streamwise velocity fluctuation, turbulence intensity, Kolmogorov length scale, Kolmogorov frequency and integral length scale were estimated from the measurements taken using the single wire. The sample calibration and data reduction programs for the single wire are given in Appendix C.

The velocity fluctuation is the standard deviation of the velocity measured by the hot-wire, and the turbulence intensity in percentage is given by:

$$Tu = \frac{u}{U} \times 100 \tag{3.4}$$

Kolmogorov frequency (f_K) and Kolmogorov length scale (η) were calculated from the turbulence dissipation rate (ε), which is estimated from the spatial derivative of streamwise velocity $\partial u/\partial x$. Taylor's hypothesis was used to obtain $\partial u/\partial x$ from the streamwise velocity time series data (Equation 3.5).

$$\frac{\partial u}{\partial x} = \frac{1}{U}\frac{\partial u}{\partial t} \tag{3.5}$$

The equations for ε, η and f_K are given below (Tennekes and Lumley, 1972):

$$\varepsilon = 15\upsilon\overline{(\partial u / \partial x)^2} \tag{3.6}$$

$$\eta = (\upsilon^3 / \varepsilon)^{1/4} \tag{3.7}$$

$$f_K = U/(2\pi\eta) \tag{3.8}$$

The method proposed by VanFossen et al. (1995) was used to estimate the integral length scale of the freestream turbulence. Autocorrelation data of the single wire were least square curve-fitted by the exponential function:

$$R(\tau) = e^{-Ct x} \tag{3.9}$$

A sample autocorrelation curve is shown in Figure 3.10. The streamwise integral length scale is estimated from:

$$\lambda_x = U\int_0^{\infty} R(\tau)d\tau = \frac{U}{C_t} \tag{3.10}$$

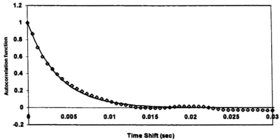

Figure 3.10 Curve-Fitting for Autocorrelation Function (0.95 cm Rod-Grid, Re_D = 67,750, x/d=25)

3.2.2.2 X-wire

Velocity and yaw calibrations were performed for the X-wire for each turbulence measurement. The yaw calibration of the X-wire followed the effective angle method proposed by Bradshaw (1971). Consider an inclined sensor of X-wire and an instantaneous velocity vector, S, that is in the plane of the hot wire and at some inclination to it (Figure 3.11a). Let the anemometer output voltage due to the velocity S be Vo. The effective velocity, U_{eff}, is defined as the velocity which, if it were normal to the wire, would produce exactly the same voltage Vo. The effective angle, θ_{eff}, between the velocity vector and the wire can then be defined as the angle that satisfies:

$$S\cos(\theta_{eff}) = U_{eff} \tag{3.11}$$

The effective angle is, therefore, approximately equal to the inclination of the hot-wire. It cannot be interpreted in a strictly geometrical sense, and depends on factors such as the straightness of the wire and the effect of longitudinal cooling of the wire. The yaw angle θ_{yaw} (Figure 3.11b) was varied from −30° to +30° in steps of 5° to determine the average effective angle θ_{eff} of each wire. The MATLAB data reduction programs for calibration of the X-wire with sample data and a yaw calibration curve are given in Appendix C.

Spanwise velocity fluctuations (v and w), which are standard deviations of velocity components in the Y and Z directions, respectively, were estimated, and autocorrelation curves were obtained from the X-wire measurements. Details of the data reduction programs are given in Appendix C.

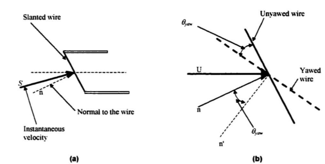

Figure 3.11 Instantaneous Velocity on a Slanted Sensor of X-wire and Yaw Angle

3.2.2.3 Vorticity Probe

The effective angles of the X-wire of the vorticity probe were determined by performing yaw calibrations similar to the calibration procedures for the X-wire. The spanwise vorticity components were measured using the vorticity probe and approximated by:

$$\Omega_y = \frac{\Delta U}{\Delta z} - \frac{\Delta W}{\Delta x} = \frac{\Delta U}{\Delta z} + \frac{1}{U}\frac{\Delta W}{\Delta t} \tag{3.12}$$

$$\Omega_z = \frac{\Delta V}{\Delta x} - \frac{\Delta U}{\Delta y} = -\frac{1}{U}\frac{\Delta V}{\Delta t} - \frac{\Delta U}{\Delta y} \tag{3.13}$$

where ΔU is the difference between the instantaneous streamwise velocity measured by a pair of parallel wires separated in spanwise directions, Δy and Δz. The spanwise velocity derivatives, $\Delta V/\Delta x$ and $\Delta W/\Delta x$, were estimated with the use of Taylor's hypothesis, i.e. $\Delta/\Delta x = -U^{-1}\,\Delta/\Delta t$.

Experimental uncertainties in turbulence intensity Tu, integral length scale λ_x, and fluctuating vorticity components, ω_y and ω_z, were estimated based on the uncertainty analysis of hot wire data by Yavuzkurt (1984). The components of total uncertainty in a variable measured by the hot-wire are uncertainty due to calibration and uncertainty due to curve fitting. The sample calculation of uncertainty in a hot wire measurement is given in Appendix B. Uncertainty in Tu, λ_x, and fluctuating vorticity components were estimated to be 3.09 percent, 10.95 percent, and 9.43 percent, respectively, as shown in Table 3.2.

Table 3.2 Experimental Uncertainty of Turbulence Parameters (%)

	Experimental Reynolds Number Range	
	Maximum	**Minimum**
Velocity Calibration (Tu, λ_x)	0.07	0.14
Velocity Curve Fitting (Tu, λ_x)	2.18	2.18
Autocorrelation Curve Fitting (λ_x)	10.50	10.50
Turbulence Intensity Tu	3.09	3.09
Integral Length Scale λ_x	10.95	10.95
Fluctuating vorticity ω_z and ω_y	9.43	9.43

Chapter IV

Results and Discussions

The experiments were performed as outlined in the previous chapter. The results are presented and discussed in this chapter. In the first section, characteristics of the freestream turbulence downstream of the rod-grids are presented. Turbulence intensity and integral length scales downstream of the grids are compared with existing results in the literature. The streamwise distribution of the three components of velocity fluctuations are also presented to highlight the evolution of the freestream vortical structures. The spanwise vorticity components were analyzed and the anisotropy of the freestream turbulence with downstream distances was estimated. The vortical structures of the freestream were further analyzed using wavelet transforms. This technique is increasingly used to detect coherent motions in turbulence. The second part of this chapter deals with the heat transfer augmentation in the stagnation region. The characteristics of heat transfer in the stagnation region due to the freestream turbulence generated by the two grid orientations are analyzed and presented. The heat transfer enhancement at the stagnation line for the two grid orientations are compared and discussed based on the literature on coherent vortical structures. Finally, heat transfer augmentation in the off-stagnation region for different freestream vortical structures is presented.

4.1 Characteristics of Freestream Turbulence

4.1.1 Turbulence Intensity

The streamwise turbulence intensity downstream of the three rod-grids are almost independent of Reynolds number (Figure 4.1), and well represented with the power law of Roach (1987).

$$Tu = C_1\left(\frac{x}{d}\right)^{-\frac{5}{7}} \tag{4.1}$$

The values of C_1 are 1.12, 1.24 and 1.20 for the rod-grids of 2.86 cm, 1.59 cm and 0.95 cm, respectively. The turbulence intensity decreases approximately from 12% to 4% as the grid-to-model distance increases from 25*d* to 125*d*.

4.1.2 Integral Length Scales

The streamwise distributions of the ratio of integral length scale to the diameter of the grid-rods (λ_x *d*) are given in Figure 4.2 for the three Reynolds numbers. Unlike the turbulence intensity, $\lambda_x d$ is dependent on Reynolds number, and the best-fit lines with the power law for the different Reynolds numbers are presented in Figure 4.2. The form of the power law used has the same growth rate of λ_x proposed by Roach (1987).

$$\lambda_x = C_2\left(\frac{x}{d}\right)^{\frac{1}{2}} \tag{4.2}$$

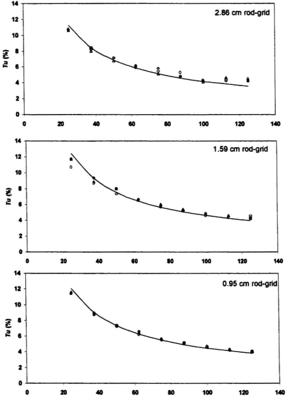

Figure 4.1 Streamwise Turbulence Intensity Downstream of the Grids (◊, Re_D = 67,750; Δ, 108,350; ο, 142,250)

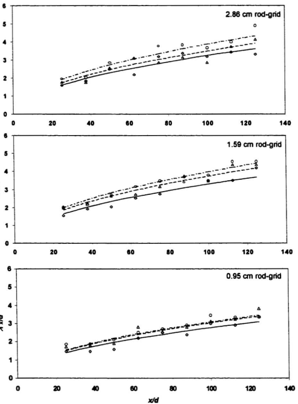

Figure 4.2. Streamwise Integral Length Scale Downstream of the Grids (◊, ____, Re_D = 67,750; Δ, ----, 108,350; ο, -.-.-., 142,250)

The values of C_2 are given in Table 4.1 for the different rod-grids and Reynolds numbers. The λ_x/d increases by about 45% as x/d increases from 25 to 125, and is in reasonable agreement with the results of Roach (1987). It should be noted that both rod-grids in perpendicular and parallel orientations give the same Tu and λ_x/d since they are calculated based on the streamwise velocity fluctuations.

Table 4.1 The constant C_2 of Eq. (4.2)

	Re_D= 67,750	Re_D= 108,350	Re_D= 142,250
2.86-cm rod	0.3235	0.3500	0.3873
1.59-cm rod	0.3299	0.3751	0.3984
0.95-cm rod	0.2767	0.3046	0.3105

4.1.3 Fluctuating Velocity Components

The rms values of the fluctuating velocity components, u, v and w, downstream of the rod-grids in perpendicular orientation are presented in Figure 4.3. At locations close to the grid, v and u are approximately equal ($v/u \approx 1$), and higher than the w component (w/u is in the range 0.85 to 0.91), because most of the turbulent eddies are aligned with the turbulence generating rods and velocity fluctuations in directions parallel to the rods are not as intense as in other directions. As x/d increases, the difference between the three components decreases. At x/d=125, v/u and w/u range from 0.99 to 0.9 and from 0.88 to 0.99, respectively. A plausible conclusion from Figure 4.3 is that the distinct structures of turbulence due to the parallel array of rods become more homogeneous with distance from the grid.

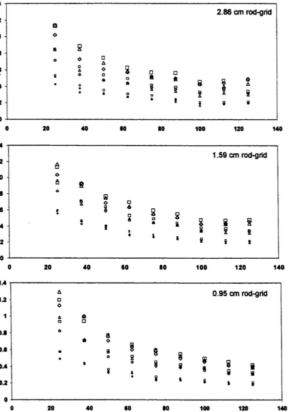

Figure 4.3. RMS Fluctuating Velocity Components of Grid in Perpendicular Orientation

(Re_D = 142,250:□, *u*, Δ, *v*, ◊, *w*; Re_D = 108,350: □, *u*, Δ, *v*, ◊, *w*; Re_D= 67,750: □, *u*, Δ, *v*, ◊, *w*)

4.1.4 Spanwise Vorticity Components and Isotropy of Turbulence

The streamwise distribution of spanwise vorticity, normalized with the mean freestream velocity and diameter of the leading edge, are presented in Figure 4.4. Since greater vorticity is usually associated with the smaller eddies in turbulence (Tennekes and Lumley, 1972), the fluctuating vorticity component increases with smaller grid-rod for a given mean freestream velocity. For example, at $x/d = 25$, $\omega D/U$ ranges from 20.02 to 25.18 for the 2.86 cm grid while it varies from 31.77 to 39.50 for the 0.95 cm grid. An attempt to examine the isotropy of the rod-grid turbulence was made by estimating the degree of isotropy of the turbulence from the measurements taken with the single wire and vorticity probes. For isotropic turbulence, $5\overline{\left(\frac{\partial u}{\partial x}\right)^2}$ is equal to $\overline{\omega_z^{\,2}}$ and $\overline{\omega_y^{\,2}}$ (Zhou and Antonia, 2000). Therefore, the degree of isotropy is defined as:

$$Iso = \frac{\overline{\omega^2}}{5\overline{\left(\frac{\partial u}{\partial x}\right)^2}} \tag{4.3}$$

where $\overline{\omega^2}$ is the mean square value of the fluctuating vorticity components and $\partial u/\partial x$ is estimated from single wire measurements. The streamwise distributions of the estimated degree of isotropy, which is calculated from the best-fit curves of vorticity components and $\partial u/\partial x$, are shown in Figure 4.5. For the 2.86 cm rod-grids, deviation from isotropy is highest (*Iso* of an order of 7 at x/d=25) at the lowest Reynolds number. At freestream Re_D of 67,750, the grid turbulence approaches isotropy with downstream distance for all grids (*Iso* ~ 1 at x/d=125). Deviation from isotropy is higher for the higher Reynolds numbers

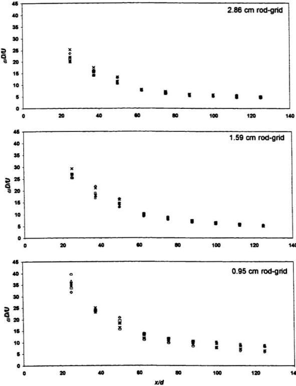

Figure 4.4. Streamwise Distribution of Fluctuating Vorticity Components (Re_D=67,750: ◊, ω_z, ×, ω_y; Re_D=108,350: □, ω_z, *, ω_y; Re_D= 142,250: Δ, ω_z, O, ω_y)

($Iso \sim 2$ at x/d=125) for Re_D of 108,350 and 142,250. The general trend is that turbulence approaches isotropy as downstream distance increases, turbulence generated by the biggest rod-grid is the most anisotropic.

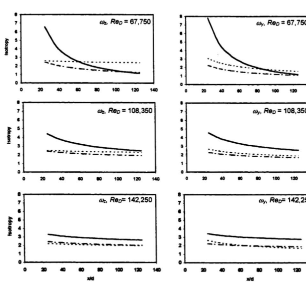

Figure 4.5. Streamwise Trends of the Degree of Isotropy (Rod-grids of: —, 2.86 cm; - — -, 1.59 cm; - - -, 0.95 cm)

4.1.5 Wavelet Analysis of Freestream Turbulence

Wavelet transforms have been increasingly used to identify the coherent structures of turbulent flows in recent years (Everson et al., 1990; Higuchi et al., 1994; Sullivan and Pollard, 1996; Addison, 1999). Wavelet transform is a signal analysis tool which allows both spectral and temporal information to be described simultaneously within the signal. Several researchers (Hajj and Tieleman, 1996; Souza et al., 1999) discussed the advantages of the wavelet transform over the Fourier analysis or conditional sampling techniques in detecting the turbulent structures. The main advantages of the wavelet analysis over other methods are better identification of energy containing spatial structures, and its ability to analyse individual coherent events without losing temporal information.

The wavelet transform of a continuous real-valued time signal, $s(t)$, with respect to the real valued wavelet function, g, is defined as

$$C_t(a,b) = \frac{1}{\sqrt{a}} \int_{-\infty}^{-\infty} g\left(\frac{t-b}{a}\right) s(t)\, dt \tag{4.4}$$

The transform coefficients $C_t(a, b)$ are found for both specific locations on the signal, $t = b$, and for specific wavelet periods (which are a function of a). Several wavelets, i.e. various forms of function g, are available for the analysis. The Mexican hat wavelet was used for this study. This wavelet is particularly good at highlighting the energy-containing structures within the flow signal (Addison, 1999), and offers better temporal resolution of individual events (Souza et al., 1999). The Mexican hat wavelet (see Figure 4.6) is the second derivative of the Gaussian function, is defined as:

$$g\left(\frac{t-b}{a}\right) = \left[1 - \left(\frac{t-b}{a}\right)^2\right] e^{-(1/2)[(t-b)/a]^2} \tag{4.5}$$

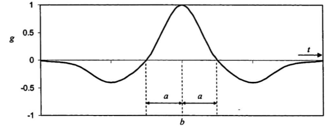

Figure 4.6 The Mexican Hat Wavelet (Equation 4.5)

The wavelet analysis was performed on the two lateral velocity components, v and w, since the objective was to detect vortical structures with the vortex lines in Y and Z directions. With velocity measurements behind the grids of parallel rods in horizontal orientation, the velocity component v should be the most indicative of the passage of primary coherent structures produced by the parallel rods (see Figure 4.7). On the other hand, the formation of secondary vortices, i.e. vortices with vorticity in the Y direction, should be reflected by the lateral velocity component w.

The sample temporal plots of the transform coefficients of two lateral fluctuating velocity components for the 2.86 cm rod-grid are given for x/d=25 and 125 in Figures 4.8 and 4.9, respectively. The same scale of the transform coefficients was used for each figure for the purpose of comparison. As can be seen in Figure 4.8, the velocity component v has much higher transform coefficients than w, indicating that the Mexican hat wavelet detected the energy containing structures, particularly at the scale a between 100 and 200 of the primary vortices. The structures over a wide range of scales can be seen in the transform plot for v. The periodic structures can be seen in the transform plot for the component w, however, with no significant peak at a particular scale. As shown in Figure 4.9, there is no significant difference between the temporal transform plots for the two lateral fluctuating velocity components. A comparison of Figures 4.8 and 4.9 illustrates that the structures of turbulence, i.e the characteristics of primary and secondary vortices, change substantially as x/d increases from 25 to 125.

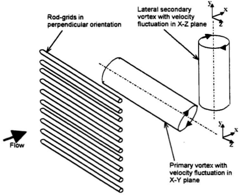

Figure 4.7 Primary Vortices behind the Grid-Rods in Perpendicular Orientation

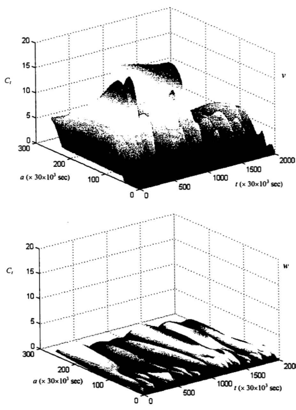

Figure 4.8 Temporal Plots of Wavelet Transform Coefficients for the 2.86 cm Rod-grids at x/d = 25

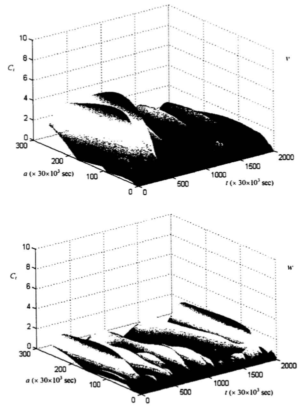

Figure 4.9 Temporal Plots of Wavelet Transform Coefficients for the 2.86 cm Rod-grids at x/d = 125

Although the wavelet analysis can provide the temporal information of turbulence structures, the current investigation of the evolution of the vortical structures downstream of the rod-grids only requires the time averaged information of the turbulence structures of different scales at different downstream distances. Therefore, the wavelet energy spectra analysis was used, and the energy spectra were plotted. The procedure is outlined below, and the details of the program are given in Appendix C.

(i) The wavelet transform (Equation 4.4 with the Mexican hat wavelet) was obtained for the time series velocity fluctuations.

(ii) The contribution to the total energy contained within the signal at a specific a scale is given by:

$$E(a) = \frac{1}{C_g} \int_{-\infty}^{+\infty} \frac{1}{a^2} [C_t(a,b)]^2 \, db \tag{4.6}$$

where C_g is the admissibility constant and equal to π for the Mexican hat wavelet (Addison, 1999).

(iii) The wavelet a scale (which is a time period) was converted to a frequency by:

$$f = \frac{f_c}{a} = \frac{0.251}{a} \tag{4.7}$$

(Note: for the Mexican hat wavelet with a = 1, the angular frequency of the passband centre of the wavelet ω_c is equal to $\sqrt{(5/2)}$ rad/s, or f_c = 0.251 Hz.)

As a sample, the wavelet energy spectra for the lateral velocity fluctuation v was compared with the spectra obtained using the Fourier transform for the 1.59 cm rod-grid component at x/d=25, see Figure 4.10. As claimed by previous studies, the wavelet can identify the energy containing structures more clearly than the Fourier transform.

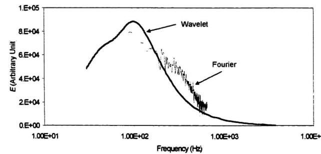

Figure 4.10 Comparison of Wavelet and Fourier Energy Spectra

The wavelet spectra plots of v and w for the 2.86 cm rod-grid in perpendicular orientation are shown in Figure 4.11 for $Re_D = 67{,}750$. An arbitrary scale was used for the total energy spectra since only qualitative information was required to examine the evolution of the vortical structures. The wavelet transform values were calculated for the fluctuating velocity components. As shown in Figure 4.11, there are significant differences in the characteristics of the spectra of the two velocity components at $x/d = 25$ and 50. The wavelet energy density function of v has a significant peak at a frequency of around 75 Hz for $x/d = 25$, while the curve for w shows only a very slight peak at this frequency. This implies that primary vortices at a particular scale ($= U/2\pi f = 0.052D$) are prominent in the flow at this downstream location. The secondary vortices are more random in nature with a typical energy distribution among the turbulent eddies, i.e higher energy associated with the larger eddies. Further downstream (at $x/d = 50$ and 75), the energy density curve of v changes in such a way that the turbulent flow gradually approaches isotropy with downstream distance by transferring turbulence energy concentrated at a particular eddy size to larger and smaller eddies. At x/d= 100 and 125, the energy density curves for v and w are not significantly different, implying that three-dimensionality of the turbulence increases. The characteristics of the primary and secondary vortices seem to be quite similar at these downstream distances.

The wavelet energy spectra plots of v and w for the 1.59cm rod-grid in perpendicular orientation at Re_D=67,750 are given in Figure 4.12. At x/d = 25, the energy density function of v has a maximum at $f \approx$ 100 Hz. The size of the energy containing eddies of this grid is, therefore, smaller than that generated by the 2.86 cm rod-grid. The energy density curve of w also has a local peak at $f \approx 115$ Hz. This is probably contributed by the deformation of streamwise vortices. The difference in characteristics of the lower frequency eddies between v and w are significant at x/d = 25 and 50. However, this difference diminishes as the downstream distance increases to 75, 100 and 125, indicating the increasing three-dimensionality of the coherent structures.

Figure 4.13 shows the wavelet energy density function of v and w for the 0.95 cm rod-gird in the perpendicular orientation at Re_D = 67,750. The curve for v shows a local peak at $f \approx$ 175 Hz at x/d = 25. Therefore, the size of the energy containing eddies for this rod-grid is the smallest in comparison with the other rod-grids. It should be noted that even at x/d = 25, the energy density function for v has its maximum value at larger eddies, indicating that the primary coherent vortices in the flow are not as dominant as those with the larger rod-grids. The difference between the two energy density curves is not significant for downstream distances x/d = 50 to 125 (Figure 4.13).

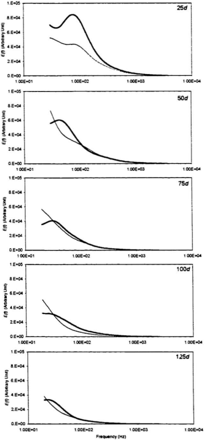

Figure 4.11 Wavelet Energy Spectra for 2.86 cm Grid (Perpendicular) at Re_D=67,750 (— ,v; —, w)

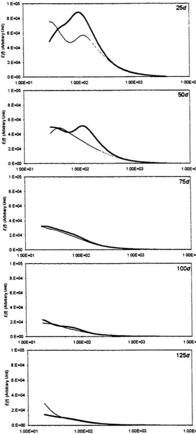

Figure 4.12 Wavelet Energy Spectra for 1.59 cm Grid (Perpendicular) at Re_D=67,750 (— ,v; —, w)

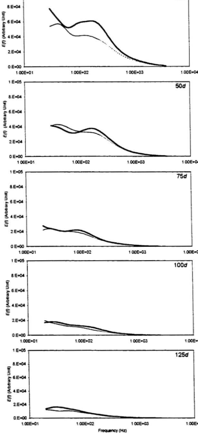

Figure 4.13 Wavelet Energy Spectra for 0.95 cm Grid (Perpendicular) at Re_D=67,750 (— ,v; —, w)

The wavelet energy plots at the higher Reynolds numbers for all rod-grids in perpendicular orientation are presented in Figures 4.14 to 4.19. Similar characteristics of the wavelet energy spectra of the lateral velocity components are observed for the smaller downstream distances (x/d = 25 and 50). The exception is the detection of the additional energy containing eddies at low frequency for the v component at $x/d = 25$ for the higher Reynolds numbers (two peaks in Figures 4.16-4.19). This could possibly be contributed by the formation of larger eddies from the primary energy containing eddies, although the detailed figures cannot be provided at this point.

The following conclusions can be drawn from the wavelet analysis of the freestream turbulence generated by the grids of parallel rods.

(i) The primary vortices at a particular scale contain higher energy close to the grids and show a significant difference from the secondary vortices. This energy is gradually transferred to larger and smaller eddies as the flow travels further downstream of the grids.

(ii) Unlike the primary vortices, the secondary vortices in the lateral direction show typical energy distribution among the different scales of turbulence, i.e higher energy associated with larger scales.

(iii) The difference in the characteristics of the primary and secondary vortices are more pronounced for larger rod-grids for a given normalized downstream distance.

(iv) The difference in characteristics of the primary and secondary vortices are more pronounced for smaller downstream distance for a given rod-grid.

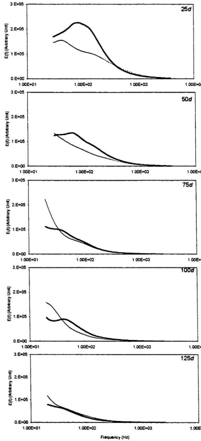

Figure 4.14 Wavelet Energy Spectra for 2.86 cm Grid (Perpendicular) at Re_D=108,350 (— ,v; —, w)

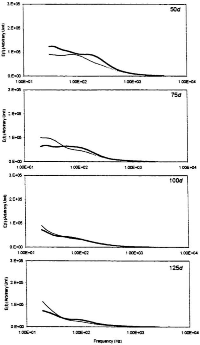

Figure 4.15 Wavelet Energy Spectra for 1.59 cm Grid (Perpendicular) at Re_D=108,350 (— ,v; ---, w)

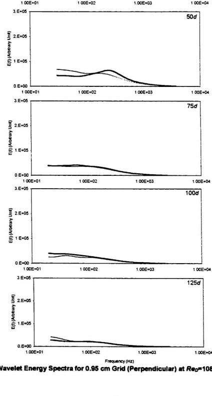

Figure 4.16 Wavelet Energy Spectra for 0.95 cm Grid (Perpendicular) at Re_D=108,350 (— ,v; —, w)

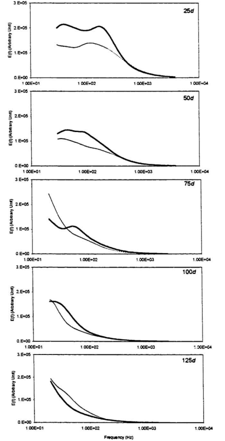

Figure 4.17 Wavelet Energy Spectra for 2.86 cm Grid (Perpendicular) at Re_D=142,250 (— ,v; —, w)

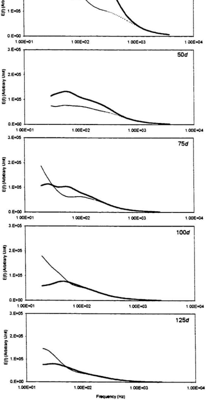

Figure 4.18 Wavelet Energy Spectra for 1.59 cm Grid (Perpendicular) at Re_D=142,250 (— ,v; ---, w)

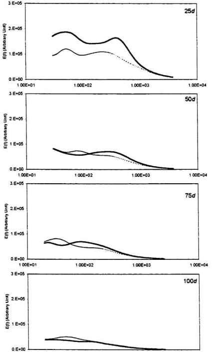

Figure 4.19 Wavelet Energy Spectra for 0.95 cm Grid (Perpendicular) at Re_D=142,250 (— ,v; —, w)

4.2 Heat Transfer Results

The distribution of Frossling number in the stagnation region for the three grids of 2.86 cm, 1.59 cm and 0.95 cm rods, where R and L denote rods in the perpendicular and parallel orientations, are presented in Figures 4.20, 4.21 and 4.22, respectively. The results for five grid locations and Re_D of 67,750, 108,350 and 142,250 are shown in the figures. The semi-theoretical solution of Frossling (1958) for a uniform freestream is also provided for reference. Heat transfer in the stagnation region decreases with increasing grid-to-model distance for a given Reynolds number. This is expected since the turbulence intensity of the freestream decreases with downstream distance from the grid. Heat transfer augmentation at the stagnation line over the uniform freestream ranges from 37% to 75% for a grid-to-model distance (x/d) of 25. The augmentation is reduced to the range 15% to 34% as x/d increases to 125. For a given x/d, the lowest heat transfer augmentation is obtained with the 2.86 cm rod-grid in parallel orientation (Figure 4.20) while the highest is obtained with the 0.95 rod-grid in perpendicular orientation (Figure 4.22). Heat transfer increases with increasing Reynolds number for a given rod-grid and grid-to-model distance. For example, heat transfer at the stagnation line increases by about 10% at x/d = 125 as Re_D increases from 67,750 to 142,250. At x/d = 25, the increase in heat transfer is about 15% for the same increase in Re_D. For the same x/d and Re_D, a smaller grid gives higher heat transfer. For example, at the stagnation line, heat transfer with the 0.95 cm rod-grid is about 5% higher than that with the 2.86 cm rod-grid.

VanFossen et al. (1995) determined that the heat transfer distribution over the stagnation region due to both uniform and turbulent freestream collapsed to a single curve regardless of the level of turbulence, when Fr is normalized by the value at the stagnation line, i.e $Fr(\theta)/Fr(0)$. Therefore, if the Frossling number at the stagnation line can be predicted accurately, the off-stagnation line heat transfer distribution can be estimated using the normalized laminar solution. The normalized heat transfer distributions (Figure 4.23-4.25) of the present study are also found to collapse to the Frossling solution within the experimental uncertainty. The experimental data are slightly below the normalized Frossling line at x/d=25. The deviation found in the region of θ>45° is that the experimental data are slightly above the normalized Frossling line. This is more pronounced for the parallel orientation of the 2.86 cm grid.

Heat transfer at the stagnation line (θ=0) with the rod-grids in perpendicular and parallel orientations is compared to investigate the effect of different freestream vortical structures (Figure 4.26). The best-fit lines to the data are also presented in the figures to highlight the trends. The detailed quantitative data of these figures is given in Table 4.2. In all cases, heat transfer enhancement by the grids in perpendicular orientation is larger than that by the grids in parallel orientation. It can be speculated that the larger heat transfer with the rod-grids in perpendicular orientation is due to greater vortex stretching of the primary vortices, which are parallel and aligned with the grid-rods. The primary vortical structures, which are detected by the wavelet analysis (Figures 4.11-4.19), can be conjectured to play an important role in the interaction of freestream turbulence with the stagnation region heat transfer.

As evident in Figure 4.26, the difference between the two heat transfer curves for the two different grid orientations decreases with increasing grid-to-model distance. As

x/d increases from 25 to 125, the average difference in heat transfer between the perpendicular and parallel orientations decreases from 7.39% to 1.06% for 2.86 cm rods, 4.63% to 0.81% for 1.59 cm rods and 2.46% to 0.89% for 0.95 cm rods. This is most likely due to the turbulence becoming more three-dimensional with increasing distance downstream of the grids (see Figures 4.3, 4.5 and 4.11-4.19). The evolution of vortical structures downstream of the grids of parallel rods can be further speculated using the literature on the vortex dynamics of wakes behind circular cylinders. The Reynolds numbers based on the rod size, Re_d, in this study range from 3,175 to 20,000. Hence, the wake is in the flow regime of shear layer transition (Zdravkovich, 1997). Besides the primary vortices, which are parallel and aligned with the circular cylinder, intense shedding of near wake (x/d < 1) streamwise vortices are present in this regime. Furthermore, three-dimensional vortical structures with sizes ranging from the shear layer thickness to the Karman vortices are expected to develop in this flow regime (Wei and Smith, 1986; Williamson, 1996). The primary vortices become dislocated and cannot be precisely traced beyond x/d > 50 in this flow regime (Zdravkovich, 1997). The streamwise vortices, which evolve from the primary vortices in the near wake region, deform into three-dimensional structures as they travel further downstream. It is plausible to assume a similar turbulence structure downstream of the grids in this study, and this assumption is fairly supported by the measured turbulence characteristics (Figures 4.3, 4.5 and 4.11-4.19), resulting in a smaller difference in heat transfer with the perpendicular and parallel grid orientations at greater grid-to-model distances.

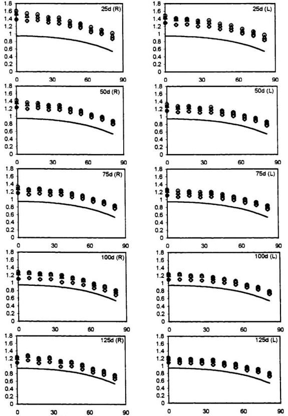

Figure 4.20 Distribution of Frossling Number in the Stagnation Region for 2.86 cm Rod-Grid(◊, Re_D = 67,750; Δ, 108,350; o, 142,250; —Frossling Solution)

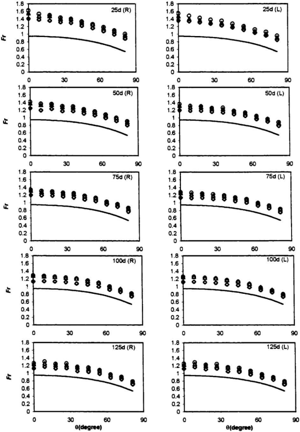

Figure 4.21 Distribution of Frossling Number in the Stagnation Region for 1.59 cm Rod-Grid(◊, Re_D = 67,750; Δ, 108,350; o, 142,250; —Frossling Solution)

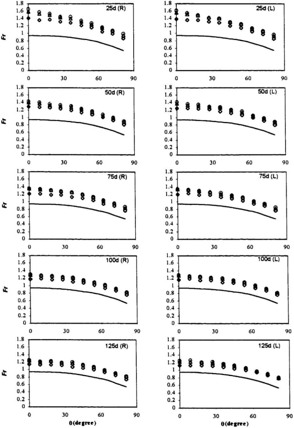

Figure 4.22 Distribution of Frossling Number in the Stagnation Region for 0.95 cm Rod-Grid(◊, Re_D = 67,750; Δ, 108,350; ο, 142,250; —Frossling Solution)

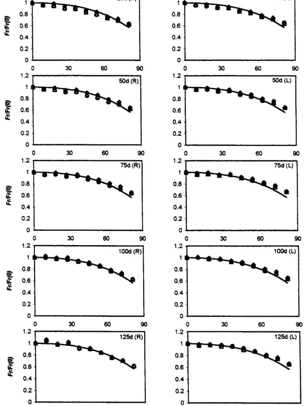

Figure 4.23 Distribution of Normalized Frossling Number in the Stagnation Region for 2.86 cm Rod-Grid(◊, Re_D = 67,750; Δ, 108,350; ο, 142,250; —Frossling Solution)

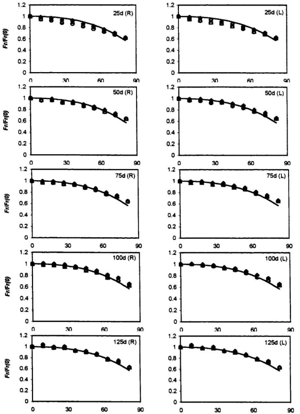

Figure 4.24 Distribution of Normalized Frossling Number in the Stagnation Region for 1.59 cm Rod-Grid(◊, Re_D = 67,750; Δ, 108,350; ○, 142,250; —Frossling Solution)

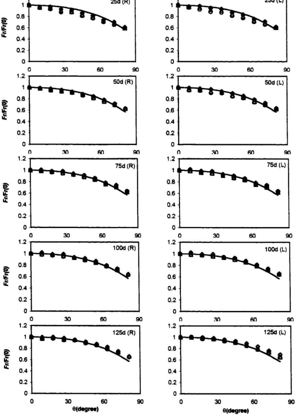

Figure 4.25 Distribution of Normalized Frossling Number in the Stagnation Region for 0.95 cm Rod-Grid(◊, Re_D = 67,750; Δ, 108,350; ○, 142,250; —Frossling Solution)

Table 4.2 Stagnation Line Frossling Numbers

	2.86 cm rods			*1.59 cm rods*			*0.95 cm rods*		
	R	***L***	***% Inc.***	***R***	***L***	***% Inc.***	***R***	***L***	***% Inc.***
I. x/d = 25									
U_1	1.3827	1.2915	*7.06*	1.4079	1.3593	*3.58*	1.4218	1.3873	*2.49*
U_2	1.5406	1.4407	*6.93*	1.5524	1.471	*5.53*	1.5916	1.5572	*2.21*
U_3	1.601	1.4801	*8.17*	1.6213	1.5473	*4.78*	1.6526	1.6094	*2.68*
II. x/d = 50									
U_1	1.2368	1.1555	*7.04*	1.2518	1.2004	*4.28*	1.2892	1.2571	*2.55*
U_2	1.3755	1.2872	*6.86*	1.3783	1.3154	*4.78*	1.4051	1.3828	*1.61*
U_3	1.4175	1.3244	*7.03*	1.4175	1.3604	*4.20*	1.4366	1.4243	*0.86*
III. x/d = 75									
U_1	1.1678	1.1131	*4.91*	1.1997	1.1374	*5.48*	1.2094	1.206	*0.28*
U_2	1.2913	1.2344	*4.61*	1.3137	1.2576	*4.46*	1.3494	1.3355	*1.04*
U_3	1.326	1.2561	*5.56*	1.3358	1.2777	*4.55*	1.3585	1.3417	*1.25*
IV. x/d = 100									
U_1	1.1018	1.0956	*0.57*	1.1312	1.1196	*1.04*	1.1774	1.1642	*1.13*
U_2	1.252	1.2197	*2.65*	1.2846	1.2471	*3.01*	1.2918	1.2705	*1.68*
U_3	1.2791	1.2336	*3.69*	1.2863	1.2544	*2.54*	1.3066	1.2825	*1.88*
V. x/d = 125									
U_1	1.0901	1.0887	*0.13*	1.1292	1.1228	*0.57*	1.14	1.1275	*1.11*
U_2	1.2157	1.1975	*1.52*	1.2361	1.2259	*0.83*	1.2382	1.2293	*0.72*
U_3	1.2321	1.2136	*1.52*	1.2624	1.2497	*1.02*	1.2626	1.2519	*0.85*

Note: 1) R and L represent the grids in perpendicular and parallel orientations, respectively.
2) U_1, U_2 and U_3 are the mean freestream velocities of 5 m/s, 8 m/s and 10.5 m/s, respectively.

The increase in heat transfer augmentation with the grids in perpendicular orientation over grids in parallel orientation decreases with decreases in the rod size. At x/d=25, the average increase in heat transfer augmentation from the perpendicular orientation over the parallel orientation is about 7.39%, 4.63% and 2.46% for the 2.86 cm, 1.59 cm and 0.95 grid-rods, respectively. The greater degree of anisotropy for the bigger grid-rods (Figure 4.5) could be the likely reason for this observed phenomenon. It can also be additionally explained from the distinction between the primary and secondary vortices downstream of a circular cylinder reported in the literature. While the size of the primary vortices depends on the size of the turbulence generating rod, the size of streamwise vortices are more dependent on the flow regime rather than the size of primary vortices (Williamson, 1996b). Within a flow regime, there are relatively small changes in the character of vortex shedding over a large range of Re_d (Williamson, 1996b). For the Re_d range of the present study, it seems likely that the size and strength of streamwise vortices, which promote the three-dimensionality of the vortical structure downstream of the grids, are somewhat comparable for all rod-grids. However, the sizes of primary vortices are relatively different for the three different rod-grids, leading to the greater degree of anisotropy of bigger grid-rods and smaller difference between the two grid orientations for smaller grid-rods.

The difference in heat transfer augmentation with the two different grid orientations over the entire stagnation region ($0° < \theta < 42°$) is presented in Figures 4.27, 4.28 and 4.29. For the 2.86 cm rod-grid, the difference in heat transfer augmentation between the two grid-orientations is highest at the stagnation line ($\theta = 0°$), and decreases with streamwise distance from the stagnation line (Figure 4.27). The percentage difference in heat transfer decreases by about three as θ increases from 0° to 40° for grid-to-model distances of 25*d*, 50*d*, 75*d*, and 100*d*. The heat transfer characteristics at grid-to-model distance of 125*d* are anomalous, where the heat transfer with the parallel orientation is higher than with the perpendicular orientation in the off-stagnation region. This distinct phenomena could be related to the large scale secondary vortical structures, called double rollers in the literature (Corke et al., 1992; Zdravkovich, 1997), found in the far wake ($x/d > 100$) of a circular cylinder; however, a detailed explanation for this cannot be offered at this point. For the 1.59 cm and 0.95 cm rod-grids, the difference in heat transfer for the two grid orientations remains relatively constant over the whole stagnation region for all grid-to-model distances and Re_D (Figure 4.28 and 4.29). The observed characteristics of the off-stagnation region heat transfer indicate that the nature of heat transfer enhancement in the stagnation region by different vortical structures is dependent on the size of the primary vortices, since the grid size is a determining factor of the size of the primary vortices.

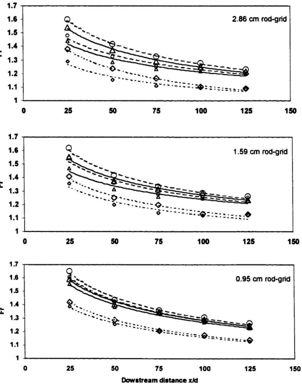

Figure 4.26 Stagnation Line Frossling Number [◊, Re_D = 67,750 (R); ◊, 67,750 (L); Δ, 108,350 (R); Δ, 108,350 (L); o, 142,250 (R); o, 142,250 (L)]

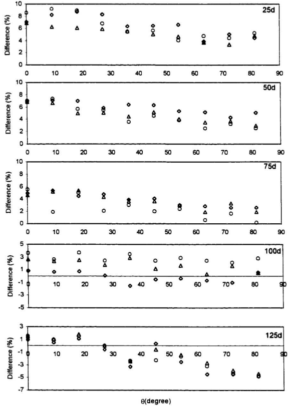

Figure 4.27 Difference in Heat Transfer with Grid in Perpendicular over Parallel Orientation for 2.86 cm Rod-grid (◊, Re_D = 67,750; Δ, 108,350; ○, 142,250)

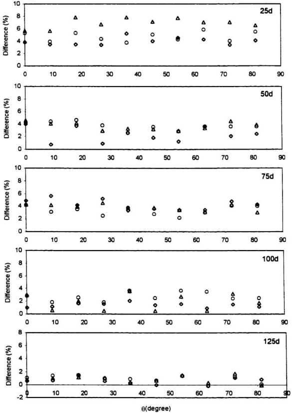

Figure 4.28 Difference in Heat Transfer with Grid in Perpendicular over Parallel Orientation for 1.59 cm Rod-grid (◊, Re_D = 67,750; Δ, 108,350; ○, 142,250)

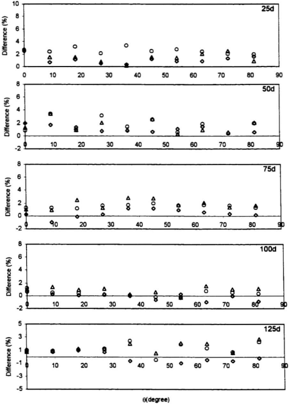

Figure 4.29 Difference in Heat Transfer with Grid in Perpendicular over Parallel Orientation for 0.95 cm Rod-grid (◊, Re_D = 67,750; Δ, 108,350; ○, 142,250)

Chapter V

Prediction of Stagnation Line Heat Transfer Augmentation

There have been a number of investigations to determine the relationship between the characteristics of freestream turbulence and stagnation line heat transfer augmentation. In this study, both a neural network and standard regression analysis were used to predict the stagnation line heat transfer. Neural networks were investigated in this instance as they are well suited to deal with a large number of variables. A new correlation model was developed by incorporating information pertaining to the vortical structures of the freestream turbulence.

5.1 Prediction Using Neural Networks

Neural networks have been used successfully in many different engineering problems, which, in general, are highly non-linear. Development of detailed mathematical models for neural networks began in the 1940s (McCulloch and Pitts, 1943; Hebb, 1949; Rosenblatt, 1959; Widrow and Hoff, 1960). More recent work by Hopfield (1986), Rumelhart and McClelland (1986) and others led to a new resurgence in this field. Neural networks have the capability of representing the physical knowledge of complex systems. A neural network extracts knowledge from the data presented to it, where the physical knowledge of the system is contained within the rules of the network. In this context, the feasibility of an Artificial Neural Network technique to predict stagnation region heat transfer in the presence of freestream turbulence was investigated.

The neural network was trained using data from the present experiments. The neural network technique used is briefly described prior to presentation of the results.

5.1.1 Neural Computing

Neural computing is a relatively new concept in computing and its architecture is motivated by the design and function of the human brain. In neural computing, the computations are performed in an entirely different manner from conventional computing. Conventional computing requires the determination of the solution to the problem and subsequent programming of the solution algorithm. By contrast, a Neural Network (NN) is trained to solve the desired problem and it derives its computing power through a massively distributed structure. Neural computing is also fault tolerant because information is distributed throughout the system architecture. If any processing element is destroyed, the performance of the network as a whole is only slightly degraded, whereas traditional computing systems are rendered useless by even a small amount of damage to memory. A NN system requires a certain amount of data for its proper training. This data could be obtained either experimentally or through physical simulations. In the present investigation, experimental data was used to train a NN for prediction of stagnation region heat transfer in the presence of freestream turbulence. A feed-forward neural network with one hidden layer and a back propagation-learning algorithm was selected in this instance, due to its popularity, simplicity and powerful function approximation capability.

5.1.1.1 Feed Forward Neural Network Model

Neural network models are specified by the net topology, node characteristics and training or learning rules. These rules specify an initial set of weights and indicate how the weights should be updated to improve the performance of the NN. A schematic of the Feed-Forward Neural Network (FFNN) architecture used for the present study is shown in Figure 5.1.

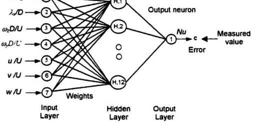

Figure 5.1 Feed-forward Artificial Neural Networks

The topology of the network consists of an input layer, one hidden layer and one output layer. There are 7 input neurons, 12 hidden neurons and 1 output neuron in the respective layers. Parameters to be considered when developing the FFNN are the number of hidden nodes and the learning rate. More complex functions can be modeled using a greater number of hidden nodes, however, if there are too many hidden nodes, the network does not find a general solution and instead becomes too specific or over-trained.

Each problem has an optimal number of hidden nodes, which needs to be determined. At least one hidden layer is required to perform a non-linear mapping. Although a multi-layered architecture can be used, it has been shown that one hidden layer is usually sufficient to solve many problems. The activation function through which the sum of the net input of a neuron determines the output of that neuron can be: sigmoidal, linear, hyperbolic tan, logistic, etc. In the present model, a logistic function has been used, which may be represented as:

$$f(x) = 1/(1 + exp(-x)) \tag{5.1}$$

The aim of the investigation is to predict via a neural network the stagnation region Nu directly from the freestream turbulence characteristics Re, λ_x, u, v, w, ω_y, and ω_z. A training sample size of 90 experimental data points was used for the NN training. The range of the input and output variables from the experimental study is given in Table 5.1. These values were normalized between 0.1 and 0.9 and were converted into binary form for acceptance by the neural network software. In order to validate the network, an independent validation set of 35 experimental data points was used.

5.1.1.2 Optimization of the Neural Network Model

The performance of the NN is influenced by the size and efficiency of the training set, by the architecture of the network and by the physical complexity of the problem being solved. It is extremely important to determine the appropriate number of hidden neurons and optimize the learning rate. There are, however, no well-defined criteria for the optimization of the NN parameters; the optimum values depend on the specific problem. Hence, a number of trials need to be performed to determine the optimum number of hidden neurons and learning rate. To obtain the optimum number of hidden neurons, a sensitivity analysis of the NN was performed in which the number of hidden neurons was varied, while keeping the other parameters constant. The effect of the number of hidden neurons on the Root Mean Square Error (RMSE) is presented in Figure 5.2. The smallest RMSE for both the training and test set of data was obtained with 12 hidden neurons. Hence, for all further computations, 12 hidden neurons were used in the NN.

Table 5.1 Variation of Input and Output Parameters

#	Variables	Range of Variation	
		Minimum	**Maximum**
	Experimental input data		
1	Reynolds number (Re_D)	67,750	142,250
2	Integral length scale (λ_x/D)	0.0694	0.70
3	Span wise vorticity ($\omega_z D/U$)	4.55	39.50
4	Normal vorticity ($\omega_y D/U$)	4.55	39.50
5	Stream wise turbulence intensity (u/U)	0.0393	0.1178
6	Normal turbulence intensity (v/U)	0.0335	0.1233
7	Span wise turbulence intensity (w/U)	0.0335	0.1233
	Experimental measured values		
8	Nusselt number (Nu)	283.4	623.3

The learning rate of the NN was also optimized for the present investigation. The learning algorithm modifies the weights associated with each processing element such that the system minimizes the error between the target output and the actual network output. Figure 5.3 shows the influence of the learning parameter on the RMSE. The RMSE is plotted as a function of the epoch size, a number that represents how many times each data set has been presented to the network. A smaller learning rate parameter results in a smaller change in the network from one iteration to the next and the learning curve is smoother. This is, however, attained at the cost of a slower rate of learning.

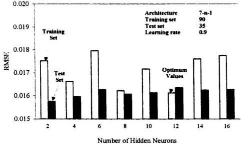

Figure 5.2 Optimization of the Number of Hidden Neurons

When the learning rate parameter increases, the learning process is faster. Further, at high epoch sizes, the learning process becomes slower and the curves for learning rates of 0.5, 0.7 and 0.9 are almost the same. The learning rate that, on average, yields a local minimum error with the smallest epoch size is selected as the optimum. A learning rate of 0.9 has been selected for the present NN. The learning is quite rapid and the test error is very close to the training error, which indicates the network is able to generalize the problem well when new test data was presented to it. The training was also carried out for an epoch size of 20,000. The test error and training error were further reduced. The learning process was stopped, when the generalization performance was observed to be satisfactory. Table 5.2 summarizes the optimal values of the trained NN parameters.

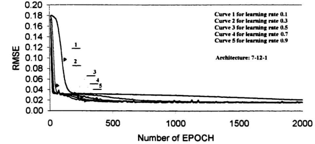

Figure 5.3 Optimization of the Learning Rate Value

Table 5.2 Neural Network Optimization Configurations

Variable Name	Optimization Parameter
Number of input neurons	7
Number of hidden neurons	12
Number of output neurons	1
Learning rate	0.9
EPOCH size	20000
Training sample size	90
Training error	0.009447
Test error	0.010718

5.1.2 Results from the Neural Network

The trained and optimized NN was evaluated using a new set of 35 measured data points. The error analysis for the cross-validation of the new set of 35 data points showed that the error of the NN output for more than 80 percent of the data points was below 2%, and the maximum error of any data point was below 3%. This indicates that the network was able to predict the output with a high degree of accuracy for the present problem.

To further evaluate the efficacy of the NN, the network was used to predict the variation of the stagnation line heat transfer with the freestream turbulence parameters; these calculated data were then compared to the experimental data (Figures 5.4-5.9). In all cases, there is very good agreement between the heat transfer predicted by the NN and the experimental results. The results indicate that there is a decrease in the heat transfer with an increase in the integral length scale (Figure 5.4), and an increase in heat transfer with an increase in the other parameters.

In neural network analysis, the relative importance of an input parameter is usually determined by the contribution of this parameter to the output parameter. For this purpose, the NEUROSHELL2 package was used to determine the relative contribution factor of input variables in predicting heat transfer augmentation in the stagnation line. The results are plotted in Figure 5.10. On the maximum scale of 6, provided by the software, turbulence intensity has the highest contribution factor, 5.38, and integral length scale has the lowest, 3.54. All the measured input variables seem to have fairly equivalent influence on the stagnation line heat transfer augmentation. Therefore, all of the characteristics of freestream turbulence measured in this study should be considered in the formulation of mathematical correlation models.

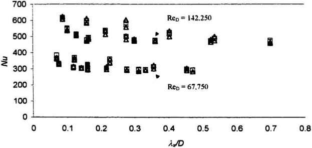

Figure 5.4 Nusselt Number (*Nu*) vs. Integral Length Scale (λ_x/D) Δ Measured Values; □ Calculated by Neural Network

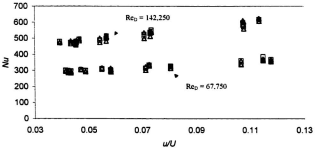

Figure 5.5 Nusselt Number (*Nu*) vs. Streamwise Turbulence Intensity (*u/U*) Δ Measured Values; □Calculated by Neural Network

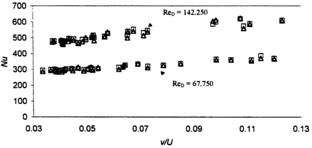

Figure 5.6 Nusselt Number (*Nu*) vs. Normal Turbulence Intensity (*v/U*) Δ Measured Values; □ Calculated by Neural Network

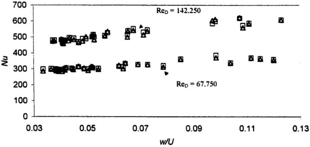

Figure 5.7 Nusselt Number (*Nu*) vs. Spanwise Turbulence Intensity (*w/U*) Δ Measured Values; □ Calculated by Neural Network

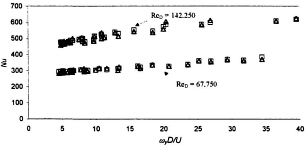

Figure 5.8 Nusselt Number (Nu) vs. Normal Vorticity ($\omega_y D/U$) Δ Measured Values; □ Calculated by Neural Network

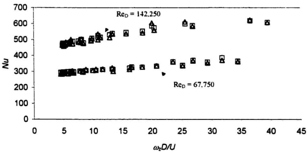

Figure 5.9 Nusselt Number (Nu) vs. Spanwise Vorticity ($\omega_z D/U$) Δ Measured Values; □ Calculated by Neural Network

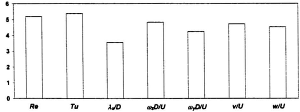

Figure 5.10 Relative Contribution (Strength) Factors of Input Variables

The use of neural networks in this field is innovative. The present investigation has demonstrated that a neural network can be trained effectively to predict heat transfer using a large number of input variables. The NN performance is strongly dependent on the number and character of the training samples. The number of hidden neurons and the learning rate are also crucial parameters. The number of hidden neurons is much more dependent on the relationship between the input and the output rather than the number of input and output neurons. A greater number of hidden neurons are required as the complexity of the problem increases.

5.2 Prediction by Correlation Models

In this section, heat transfer data of the present study is compared with existing correlation models. Using standard regression analysis, a new correlation model, which takes into account the structures of turbulence, is also developed.

5.2.1 Comparison with Existing Correlation Models

The data from the three grids is compared with the correlation of VanFossen et al. (1995) for freestream turbulence from square bar mesh grids:

$$Fr = 0.008\sqrt{Tu\, Re_D^{\,0.8}\left(\frac{\lambda_x}{D}\right)^{-0.574}} + 0.939 \tag{5.3}$$

As shown in Figure 5.11, the discrepancy between the present experimental data and Equation (5.3) is significant for the 2.86 cm rod-grid, but the agreement improves with decreasing size of rods. For the 0.95 cm rod-grid, 87% of the data falls within ± 4 percent of Equation (5.3). It is clear from Figure 5.11 that correlations developed for isotropic turbulence generated by square mesh grids should be corrected to predict the heat transfer due to the turbulence with distinct coherent vortical structures. The errors are larger for the 2.86 cm rod-grid, where the freestream turbulence has a greater distinction between the primary and secondary vortices. It is unlikely that correlations developed for isotropic turbulence can be used to estimate heat transfer to gas turbine blades, where the turbulence from the combustor and wakes from the upstream blades are highly anisotropic and laced with well-defined vortical structures.

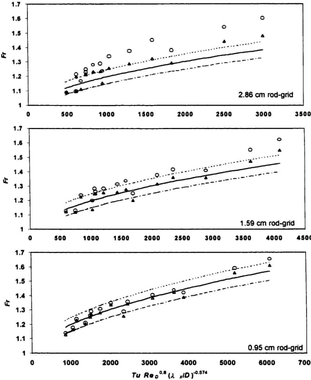

Figure 5.11 Stagnation Line *Fr* Vs. Correlation Parameter proposed by VanFossen et al. (1995) [Orientation of Rod-grids: o, Perpendicular; Δ, Parallel, Correlation lines: ___, VanFossen et al. (1995); _ _ _, + 4%; _ _ _ _; - 4%]

5.2.2 Correlation Model Incorporating Vortical Structures and Vorticity Field

The freestream turbulence needs to be characterized more comprehensively to obtain more accurate empirical models. Characterizing the freestream turbulence with Tu, Re_D and λ_x does not provide a complete picture of the turbulence, especially when the turbulence is anisotropic. The Reynolds number does not describe the nature of turbulence. The Tu and λ_x provide very limited information about the structure of the turbulence since they are estimated from streamwise velocity fluctuations measured by a single wire. The correlation model to estimate the stagnation line heat transfer was formulated incorporating information pertaining to the coherent structures and vorticity field. It seems plausible that incorporating the vorticity field and spanwise velocity fluctuations would improve the correlation, since they highlight the distinct structure of turbulence (see Figures 4.3-4.5). Since the vorticity amplification due to vortex stretching is hypothesized to be an influential factor in stagnation region heat transfer, the fluctuating vorticity component of primary vortices, i.e. ω_y and ω_z for turbulence generated by the rod-grids in perpendicular and parallel orientations, respectively, were considered to form a new turbulence parameter. The products of spanwise vorticity and velocity fluctuating components, $v\omega_z$ and $w\omega_y$, were taken as additional parameters to be included in the correlation. The products, $v\omega_z$ and $w\omega_y$, can be interpreted to represent the vortex forces in turbulence, which are analogous to the Coriolis forces (Tennekes and Lumley, 1972). The additional turbulence parameter used to develop a new correlation for the stagnation line heat transfer is defined as:

$$F_v = \frac{v\omega_z D}{U^2}$$ For rods-grid in perpendicular orientation (5.4a)

$$F_v = \frac{w\omega_y D}{U^2}$$ For rods-grid in parallel orientation (5.4b)

Therefore, the additional parameter is the vortex force due to freestream vortices, which are susceptible to stretching, normalized by the diameter of the leading edge and the mean freestream velocity. The new correlation was obtained by a regression analysis and is presented in Figure 5.12. It can be seen that 95 % of the experimental data falls within the +/- 4% of the new correlation given by:

$$Fr = 0.00021\sqrt{Re_D^{\,1.2146}\, Tu^{0.4845}\left(\frac{\lambda_x}{D}\right)^{-0.0752} F_v^{\,0.3833}} + 0.939 \qquad (5.5)$$

The improved correlation suggests that the inclusion of the vorticity field and spanwise velocity components takes into account the vortical structures of the freestream to a certain extent. It is clear that freestream turbulence with different orientations of coherent vortical structures has different influence over the heat transfer in the stagnation region, and the consideration of vortical structures of turbulence would improve the correlation models in prediction of gas turbine heat transfer.

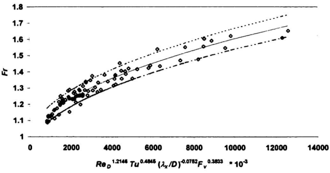

Figure 5.12 Stagnation Line *Fr* Vs. Correlation Parameter with Spanwise Vorticity and Velocity Fluctuations for both Grid Orientations (◊, Data, Correlation lines: ___, Equation (5.5); _ _ _, + 4%; __ _ __; - 4%)

Chapter VI

Conclusions, Contributions and Recommendations

An experimental study was performed to investigate the effect of freestream turbulence vortical structures and vorticity on stagnation region heat transfer. Freestream turbulence with different orientations of primary vortices was generated using grids of 2.86 cm, 1.59 cm and 0.95 cm diameter parallel rods in perpendicular and parallel orientations with respect to the stagnation line. The characteristics of freestream turbulence were measured using hot-wire anemometry. Heat transfer in the stagnation region of the heat transfer model with a cylindrical leading edge was measured. Reynolds numbers based on the diameter of the leading edge ranged from 67,750 to 142,250. The turbulence intensity and the ratio of integral length scale to leading edge diameter were in the range of 3.93% to 11.78% and 0.07 to 0.7, respectively.

6.1 Conclusions

Overall, the structures of the freestream turbulence have a significant influence on the stagnation region heat transfer. Similar to the findings of previous studies, an increase in Reynolds number and turbulence intensity results in higher heat transfer in the stagnation region, because of the thinner boundary layer and the greater transport of heat by the turbulence eddies. Heat transfer increases with decreasing integral length scale as the smaller eddies can better interact with the boundary layer. Additionally, the results of this experimental study show that stagnation region heat transfer increases with the lateral vorticity fluctuations of the freestream turbulence. The freestream turbulence where the primary vortices are susceptible to stretching gives the higher heat transfer in the stagnation region. Apparent distinction between the primary and secondary vortices, i.e. the higher degree of anisotropy of turbulence, leads to more noticeable difference in heat transfer between two grid orientations. The existing correlation models for the stagnation region heat transfer produce increasing discrepancies with greater degrees of anisotropy, since these models were developed based on nearly isotropic turbulence generated by square-mesh grids. Inclusion of turbulence parameters pertaining to the structures of turbulence could improve the correlation for the stagnation region heat transfer.

The specific conclusions with quantitative figures are:

1. Turbulence downstream of the grid of parallel rods is anisotropic close to the grids ($x/d \approx 25$-50), and the degree of anisotropy decreases with the downstream distance. The anisotropy is more pronounced with the larger rods. Three-dimensionality of the turbulence increases with greater distance downstream of the grids.
2. Wavelet analysis was used to identify the coherent primary vortices generated by the grid of parallel rods; the coherent vortices are prominent at locations close to the grids ($x/d \approx 25$-50). The difference in the characteristics of the primary and secondary vortices are more pronounced for larger rods at a given normalized downstream distance. However, these primary vortices seem to weaken and their distinction from the secondary vortices becomes less with increasing downstream distance.
3. Heat transfer in the stagnation region decreases with increasing grid-to-model distance for a given Reynolds number. The increase in heat transfer at the stagnation

line over a uniform freestream ranges from 37% to 75% at $x/d = 25$, and 15% to 34% at $x/d = 125$ for the three different grids.

4. Heat transfer increases with increasing Re_D for a given rod-grid and grid-to-model distance. The stagnation line heat transfer increases by 10% and 15% at x/d of 125 and 25 as Re_D increases from 67,750 to 142,250.
5. For a given grid-to-model distance, x/d, and Re_D, the grid with smaller diameter rods gives higher heat transfer. At the stagnation line, heat transfer with the 0.95 cm rod-grid is about 5% higher than that with the 2.86 cm rod-grid. This can be attributed to the smaller length scales associated with the smaller rod-grid.
6. The heat transfer enhancement by the grids in perpendicular orientation is larger than that by the grids in parallel orientation. This can be speculated to be caused by greater vortex stretching, since the primary vortices generated by the perpendicular orientation are primarily aligned normal to the stagnation line, and more susceptible to stretching as they approach the stagnation region.
7. The difference in heat transfer augmentation by grids in perpendicular and parallel orientations decreases with the size of grid-rods. This could be due to a more apparent distinction between primary and secondary vortices with the bigger rods which generate turbulence with a higher degree of anisotropy. At a grid-to-model distance of $25d$, the average difference in heat transfer augmentation is 7.39%, 4.63% and 2.46% for the 2.86 cm, 1.59 cm and 0.95 cm rods, respectively.
8. The difference in heat transfer augmentation with grids in perpendicular and parallel orientations decreases with increasing grid-to-model distance. This is likely due to the

greater three-dimensionality of the freestream vortical structures as the distance from the grid increases.

9. For the 2.86 cm rod-grid, the difference in heat transfer between perpendicular and parallel grid-orientations is the highest at the stagnation line, and decreases with streamwise distance. However, this difference remains fairly constant over the whole stagnation region for the 1.59 cm and 0.95 cm rod-grids. This indicates that the heat transfer enhancement in the stagnation region by different vortical structures is dependent on the size of the primary vortices.
10. The nature of heat transfer enhancement in the stagnation region by freestream turbulence with distinct coherent vortical structures is quite distinct from that by turbulence generated using square-mesh grids. The heat transfer data of this study are poorly predicted using the existing correlation models for turbulence generated from square-mesh grids. The discrepancies increase for the larger rods which generate turbulence with a higher degree of anisotropy.
11. A neural network could be an effective tool with a higher level of accuracy to predict the stagnation region heat transfer using the characteristics of the freestream turbulence measured in this study. The neural network trained in this study could predict more than 80% of the sample data points below 2% error. The maximum percentage error was 3.
12. The correlation can be improved with the inclusion of spanwise vorticity and velocity fluctuations. The improved model correlates the heat transfer data of this study within +/- 4%. Therefore, any correlation model for stagnation region heat transfer should

take into account the distinct nature of the coherent vortical structures of the turbulence to improve its predictive capability.

6.2 Contributions

The contributions of this experimental study to the literature of the stagnation region heat transfer are:

1. The study investigated the relationship between the stagnation region heat transfer and the freestream turbulence with well-defined vortical structures instead of isotropic turbulence used in the previous studies.
2. The hypothesis of the heat transfer augmentation due to vortex stretching was experimentally proved.
3. The study revealed the deficiencies of current empirical models in predicting real-life applications, where turbulence with higher degrees of anisotropy occurs.
4. The use of neural networks to predict stagnation region heat transfer, using sufficient turbulence characteristics of the freestream, was innovative and proved that neural networks could be an effective tool for convection heat transfer with a turbulent freestream.
5. A new correlation model with an additional turbulence parameter, which takes the structure of turbulence into account, was developed.

6.3 Recommendations

The followings recommendation are made for further study.

1. The influence of the vortical structures might change with the Mach number of the flow. This should be investigated since compressible flow is often encountered in gas turbine applications.
2. Measurements could be performed with the grids of parallel rods aligned at different angles with the stagnation line. This would provide a better understanding of the interaction of inclined vortical structures with the boundary layer of the stagnation region.
3. Turbulence with higher degree of anisotropy than those in this study should be tested, since these flows are common in real-life applications.
4. Inclusion of the streamwise vorticity component is recommended to obtain a more complete picture of the vorticity field.

References

Achenbach E. (1975) Total and Local Heat Transfer from a Smooth Cylinder in Crossflow at High Reynolds Numbers, *Int. J. of Heat Mass Transfer*, Vol. 18, 1387-1396.

Addison, P. S. (1999) Wavelet Analysis of the Breakdown of a Pulsed Vortex Flow, *Proc. Instn. Mech. Engrs.*, Vol. 213 (C), 217-229.

Ahmaed, G. R. and **Yovanovich, M. M.** (1997) Experimental Study of Forced Convection from Isothermal Circular and Square Cylinders and Toroids, *ASME J. of Heat Transfer*, Vol. 119, 70 - 79.

Ameri, A. A., Sockol, P. M. and **Gorla, R. S. R.** (1992) Navier-Stokes Analysis of Turbomachinery Blade External Heat Transfer, *J. of Propulsion and Power*, Vol. 8, No. 2, 374-381.

Antonia, R. A., Brown, L. W. B. and **Bisset, D. K.** (1989) Effect of Reynolds Number on the Organized Motion in a Turbulent Boundary Layer, *Near Wall Turbulence Proceedings, Zaric Memorial Conference*, ed. S. J. Kline, N. H. Afgan, 488-506, Hemisphere, New York.

Antonia, R. A., Browne, L. W. B., Bisset, D. K. and Fulachier, L. (1987) A Description of the Organized Motion in the Turbulent Far Wake of a Cylinder at Low Reynolds Number, *J. of Fluid Mechanics*, Vol. 184, 423-444.

Antonia, R. A., Browne, L. W. B. and **Shah, D. A.** (1998) Characteristics of Vorticity Fluctuations in a Turbulent Wake, *J. Fluid Mechanics*, Vol. 189, 349-365.

Antonia, R. A. and **Rajagopalan, S.** (1990) Performance of Lateral Vorticity Probe in a Turbulent Wake, *Exp. Fluids*, Vol. 9, 118-120.

Antonia R. A., Zhu, Y. and **Kim, J.** (1993) On the Measurement of Lateral Velocity Derivatives in Turbulence Flows, *Exp. Fluids*, Vol. 9, 65-69.

Balint J. L., Wallace, J. M. and **Vukoslaveevic, P.** (1991) The Velocity and Vorticity Vector Fields of a Turbulent Boundary Layer, Part 2, Statistical Properties, *J. Fluid Mechanics*, Vol. 228, 53-86.

Bathie, W. W. (1996) *Fundamentals of Gas Turbines*, 2nd Ed., John Wiley & Sons, Inc., USA.

Bisset, D. K., Antonia, R. A. and **Browne, L. W. B.** (1990) Spatial Organization of Large Structures in the Turbulent Far Wake of a Cylinder, *J. of Fluid Mechanics*, Vol. 218, 439-461.

Blair, M.F., Dring, R. P. and **Joslyn, H. D.** (1989) The Effects of Turbulence and Stator/Rotor Interactions on Turbine Heat Transfer: Part I - Design Operating Conditions, *ASME J. of Turbomachinery*, Vol. 111, 87-96.

Boyle, R. J. (1991) Navier-Stokes Analysis of Turbine Blade Heat Transfer, *ASME J. of Turbomachinery*, Vol. 113, 392-403.

Bradshaw, P. (1971) *An Introduction to Turbulence and its Measurements*, Pergamon, Oxford.

Carpenter, P. (1997) The Right Sort of Roughness, *Nature*, Vol. 388, pp. 713-714.

Ching, C. Y. and **O'Brien, J. E.** (1991) Unsteady Heat Flux in a Cylinder Stagnation Region with High Freestream Turbulence, *Fundamental Experimental*

Measurements in Heat Transfer, eds. Beasley, D. E. and Chen, J. L. S., HTD-Vol. 179, 57-66.

Corke, T., Krull, J. D. and **Ghassemi, M.** (1992) Three-dimensional Mode Resonance in Far Wake, *J. of Fluid Mechanics*, Vol. 239, No. 99.

Daniels, L. C. and **Shultz, D. L.** (1982) Heat Transfer Rate to Blade Profiles- Theroy and Measurement in Transient Facilities, *VKI Lecture Series*, Vols. 1 and 2.

Du, H., Ekkad, S. and **Han, J. C.** (1997) Effect of Unsteady Wake with Trailing Edge Coolant Ejection on Detailed Heat Transfer Coefficient Distributions for a Gas Turbine Blade, *ASME J. of Heat Transfer*, Vol. 119, 242 - 248.

Duffy, S.F., Sandifer, J.B., DeBellis, C. L., Edwards, M.J. and **Hindman, D. L.** (1997) Trends in the Design and Analysis of Components Fabricated from CFCCs, *ASME J. of Engineering for Gas Turbines and Power*, Vol. 119, 1 - 6.

Dullenkopf, K. and **Mayle, R. E.** (1995) An Account of Free-Stream-Turbulence Length Scale on Laminar Heat Transfer, *ASME J. of Turbomachinery*, Vol. 117, 401-406.

Eckkelmann, H., Nychas, S. G., Brodkey, R. S. and **Wallace, J. M.** (1977) Vorticity and Turbulence Production in Pattern Recognized Turbulence Flow Structures, *Physics of Fluids*, Vol. 20, 225-231.

Everson, R., Sirovoich, L. and **Sreenivasan, K. R.** (1990) Wavelet Analysis of the Turbulent Jet, *Phys. Lett. (A)*, Vol. 145, no. 6-7, 314-322.

Forrest, A. E. (1977) Engineering Predictions of Transitional Boundary Layers, AGARD-CP-224.

Foss, J. F. (1981) Advanced Techniques for Transverse Vorticity Measurements, *Proc. Biannual Symp. on Turbulence*, Rolla, Missouri, 1980, 208-218.

Foss, J. F. (1994) Vorticity Consideration and Planar Shear Layers, *Exp. Therm. Fluid Sci.*, Vol. 8, 260-270.

Foss, J. F., Ali, S. K. and **Haw, R. C.** (1987) A Critical Analysis of Transverse Vorticity Measurements in a Large Plane Shear Layer, *Advances in Turbulence, First European Turbulence Conference*, 1986, eds. Comopte-Bellot. G. and Mathieu, J., 446-455, Berlin/Heidelberg/New York: Springer-Verlag.

Foss, J. F. and **Haw, R. C.** (1990a) Transverse Vorticity Measurements using a Compact Array of Four Sensors. *The Heuristics of Thermal Anemometry*, eds. Stock, D. E., Sherif, S. A., Smits, A. J., ASME-FED 97: 71-76.

Foss, J. F. and Haw, R. C. (1990b) Vorticity and Velocity Measurements in a 2:1 Mixing Layer, *Forum on Turbulent Flows*, eds. Bowers, W. W., Morris, M. J., Samimy, M., ASME-FED 94: 115-120.

Frossling, N. (1958) Evaporating Heat Transfer and Velocity Distribution in Two-Dimensional and Rotationally Symmetric Laminar Boundary Layer Flow, NACA TM-1432.

Hajj, M. R. and **Tieleman, H. W.** (1996) Application of Wavelet Analysis to Incident Wind in Relevance to Wind Loads on Low-Rise Structures, *Trans. ASME*, Vol. 118, 874-876.

Han, J. C., Zhang, L. and **Ou, S.** (1993) Influence of Unsteady Wake on Heat Transfer Coefficients from a Gas Turbine Blade, *ASME J. of Heat Transfer*, Vol. 115, 904-911.

Hannis, J. M. and **Smith, M. K. D.** (1982) The Design and Test of Air Cooled Blading for an Industrial Gas Turbine, ASME Paper 82-GT-229.

Head, M. R. and **Bandyopadhyay, P.** (1981) New Aspects of Turbulent Boundary Layer Structure, *J. of Fluid Mechanics*, Vol. 107, 297-338.

Hebb, D.O. (1949) *The Organisation of the Behaviour*, John Wiley, New York.

Higuchi, H., Lewalle, J. and **Crane, P.** (1996) On the Structures of a Two-Dimensional Wake Behind a Pair of Flat Plates, *Physics of of Fluids*, Vol. 6, no. 1., 297-305.

Ho, C. M. and **Tai, Y. C.** (1996) Review: MEMS and its Applications for Flow Control, *ASME J. of Fluids Eng.*, Vol. 118, 437-447.

Hokan, A. (1993) *An Experimental Study of the Vortical Structure of Turbulent Flows*, PhD Thesis, City Univ., New York.

Hopfield, J.J. and **Tank, D.W.** (1986) Computing With Neural Circuits: A Model Properties Like Those of Two State Neurons, *Proc. Nat'l. Acad. Sci.* USA, Vol. 233.

Jacobson, S. A. and **Reynolds, W. C.** (1993) Active Control of Boundary Layer Wall Shear Stress Using Self-Learning Neural Networks, AIAA Paper 93-3272.

Johnston, J. P. (1974) The Effects of Rotation on Boundary Layers in Turbomachine Rotors, NASA SP 304.

Kays, W. M. and **Moffat, R. J.** (1975) The Behavior of Transpired Boundary Layers, *Studies in Convection, Vol. 1: Theory, Measurement, and Application*, ed. Launder, B. E., Academic Press, London.

Kastrinakis, E. G., Eckelmann, H. and **Willmarth, W. W.** (1979) Influence of the Flow Velocity on a Kovasznay Type Vorticity Probe, *Rev. Sci. Instr.*, Vol. 50, 759-767.

Kasagi, N. and **Iida, O.** (1999) Progress in Direct Numerical Simulation of Turbulent Heat Transfer, AJTE99-6302, *Proceedings of the 5th ASME JSME Joint Thermal Engineering Conference*, March 15-19, San Diego, USA.

Kato, M. and **Launder, B. E.** (1993) The Modeling of Turbulent Flow around Stationary and Vibrating Square Cylinders, *Proceedings of the Ninth Symposium on Turbulent Shear Flows*, Kyoto, August, 1993, 10.4.1-10.4.6.

Kestin, J. (1966) The Effect of Freestream Turbulence on Heat Transfer Rates, *Advances in Heat Transfer*, Vol. 3, 1-32.

Kestin, J. and **Wood, R.T.** (1971) The Influence of Turbulence on Mass Transfer from Cylinders, *ASME J. of Heat Transfer*, Vol. 93 C, 321-327.

Kim, J. (1989) On the Structure of Pressure Fluctuations in Simulated Turbulent Channel Flow, *J. of Fluid Mechanics.*, Vol. 205, 421-451.

Kim, J. and **Fiedler, H. E.** (1989) Vorticity Measurements in Turbulent Mixing Layer, *Advances in Turbulence 2, Second European Turbulence Conference 1988*, eds. Fernholz, H. H. and Fiedler H. E., 267-271, Berlin Heidelberg, Springer-Verlag, New York.

Kim, J., Moin P. and **Moser R.** (1987) Turbulence Statistics in Fully Developed Channel Flow at Low Reynolds Numbers, *J. of Fluid Mechanics*, Vol. 177, 133-166.

Kline, S. J. and **Robinson, S. K.** (1989) Quasi-Coherent Structures in the Turbulent Boundary Layer. Part I: Status Report on a Community-Wide Summary of the Data, in Near-Wall Turbulence, eds. Kline and Afgan, pp. 200-217, Hemishpere, New York.

Ko, S. Y. and **Tsou, F.K.** (1988) Advance in Gas Turbine Heat Transfer, *Experimental Heat Transfer, Fluid Mechanics, and Thermodynamics*, eds. Shah, R.K., Ganic, E.N. and Yang, K.T., Elsevier Science Publishing Co., Inc., New York.

Kovasznay, L. S. G. (1950) Q. Prog. Rep. Aeronaut. Dept. Contract NORD-8036-JIIB-39, Johns Hopkins Univ.

Kovasznay, L. S. G. (1954) Turbulence Measurements, *High Speed Aerodynamics and Jet Propulsion*, eds. Landenbuerg, R. W., Lewis, B., Pease, R. N. and Taylor, H. S., 213-285, Princeton University Press.

Lakshminarayana, B. (1996) *Fluid Dynamics and Heat Transfer of Turbomachinery*, Wiley - Interscience, John Wiley & Sons Inc., New York.

Larsson, J. (1997) Turbine Blade Heat Transfer Calculations Using Two-equation Turbulence Models, *Proc. Instn. Mech. Engrs.*, Vol. 221, Part A, pp. 253-262.

Lekakis, I. (1996) Calibration and Signal Interpretation for Single and Multiple Hot-Wire/Hot-Film Probes, review article, *Meas. Sci. Technol*, Vol. 7, 1313-1333.

LeGrives, E. (1986) Cooling Techniques for Modern Gas Turbines, *Topics in Turbomachinery Technology* , ed. Japikse, D., Concepts ETI, Inc., Norwich, NT.

Ligrani, P. M and **Bradshaw, P.** (1987) Spatial Resolution and Measurement of Turbulence in the Viscous Sublayer Using Subminiature Hot-Wire Probes, *Exp. Fluids*, Vol. 5, 407-417.

Lowery, G.W. and **Vachon, R.I.** (1975) Effect of Turbulence on Heat Transfer from Heated Cylinders, *Int. J. of Heat and Mass Transfer*, Vol. 18, No. 11, 1229-1242.

Maciejewski, P. K. and **Moffat, R. J.** (1992) Heat Transfer with Very High Free-Stream Turbulence: Part I - Experimental Data, and Part II - Analysis of Results, *ASME J. of Heat Transfer*, Vol. 114, 827 - 839.

Marasli, B., Nguyen, P. and **Wallace, J. M.** (1993) A Calibration Technique for Multiple-Sensor Hot-Wire Probes and Its Application to Vorticity Measurements in the Wake of a Circular Cylinder, *Exp. Fluids*, Vol. 15, 209-218.

Matsui, T. and **Okude, M.** (1980) Rearrangement of Karman Vortex Street at Low Reynolds Numbers, *XV International Congress Theoretical and Applied Mechanics*, University of Toronto Press, Toronto.

McCulloch, W.S. and **Pitts, W.** (1943) A Logical Calculus of the Idea Imminent in Nervous Activity, *Bulletin of Mathematical Biophysics*, 5, 115-133.

Mehendale, A. B., Han, J. C. and **Ou, S.** (1991) Influence of High Mainstream Turbulence on Leading Edge Heat Transfer, *ASME J. of Heat Transfer*, Vol. 113, 843-850.

Mi, J. and **Antonia, R. A.** (1996) Vorticity Characteristics of the Turbulent Intermediate Wake, *Exp. in Fluids*, Vol. 20, 383 - 392.

Moffat, R. J. (1988) Describing the Uncertainties in Experimental Results, *Experimental Thermal and Fluid Science*, Vol. 1, pp. 3-17.

Moin, P. and **Bewley, T.** (1994) Feedback Control of Turbulence, *Applied Mech. Rev.*, Vol. 47, S3-S13.

Morkovin, M. V. (1979) On the Question of Instabilities Upstream of Cylindrical Bodies, NASA CR-3231.

O' Brien, J. E. and **VanFossen, G. J.** (1985) The Influence of Jet-Grid Turbulence on Heat Transfer from the Stagnation Region of a Cylinder in Crossflow, ASME Paper 85-HT-58.

Panton, R. L. (1984) *Incompressible Flow*, John Wiley & Sons, New York, USA.

Pao, Y. H. (1965) Structure of Turbulent Velocity and Scalar Fields at large Wave Numbers, *Physics of Fluids*, Vol. 8, 1063-1075.

Payne, F. R. and **Lumely, J. L.** (1967) Large Eddy Structure of the Turbulent Wake Behind a Circular Cylinder, *Physics of Fluids*, Vol. 10, 194-196.

Prasad, A. and **Williamson, C. H. K.** (1995) Three-Dimensional Effects on Turbulent Bluff Body Wakes at Moderate Reynolds Numbers, *J. of Fluid Mechanics*,

Rajagopalan, S. and **Antonia, R. A.** (1993) RMS Spanwise Vorticity Measurements in a Turbulent Boundary Layer, *Exp. Fluids*, Vol. 14, 142-144.

Rigby, D. L. and VanFossen, G. J. (1991) Increased Heat Transfer to a Cylindrical Leading Edge Due to Spanwise Variation in the Freestream Velocity, AIAA papar 91-1739.

Roach, P. E. (1987) The Generation of Nearly Isotropic Turbulence by Means of Grids, *Heat and Fluid Flow*, Vol. 8, No. 2, pp. 82-92.

Robinson, S. K. (1990) *Kinematics of Turbulent Boundary Layer Structure*, PhD dissertation, Stanford University, USA.

Robinson, S. K. (1991) Coherent Motions in the Turbulent Boundary Layer, *Annual Review of Fluid Mechanics*, Vol. 23, 601-639.

Rosenblatt, R. (1959) *Principles of Neurodynamics*, Spartan Books, New York.

Roshko, A. (1961) Experiments on the Flow Past a Circular Cylinder at Very High Reynolds Numbers, *J. of Fluid Mechanics*, Vol. 10, 345-356.

Roshko, A. (1992) Perspectives on Bluff Body Aerodynamics, *Bluff Body Aerodynamics and Application*, Vol. 2, 1-21.

Rumelhart, D.E. and **McClelland, J.I.** (1986) *Parallel Distributed Processing: Exploration in the Microstructure of Cognition*, Vol. 1, MIT Press.

Sato, M., Kobayashi, Y., Matsuzak, A., Aoki, S., Tsukuda, V. and **Akita, E.** (1997) Final Report of the Key Technology Development Program for a Next-Generation High-Temp Gas Turbine, *ASME J. of Engineering for Gas Turbines and Power*, Vol. 119, 617 - 623.

Smit, M.C. and **Kuethe, A. M.** (1966) Effects of Turbulence on Laminar Skin Friction and Heat Transfer, *Physics of Fluids*, Vol. 9, No. 12, 2337-2344.

Smith, C. R. and **Walker, J. D. A.** (1997) Sustaining Mechanisms of Turbulent Boundary Layers: The Role of Vortex Development and Interaction, *Self Sustaining Mechanisms of Wall Turbulence*, ed. Panton, R. L., Computational Mechanics Publications, Southampton, pp. 13-47.

Souza, F. D., Delville, J., Lewalle, J. and **Bonnet, J. P.** (1999) Large Scale Coherent Structures in a Turbulent Boundary Layer Interacting with a Cylinder Wake, *Experimental Thermal and Fluid Science*, Vol. 19, pp. 204-213.

Spalart, P. R. (1988) Direct Simulation of a Turbulent Boundary Layer up to R_θ=1410, *J. of Fluid Mechanics*, Vol. 187, 61-98.

Spina, E. F. and **Smits, A. J.** (1987) Organized Structures in a Compressible, Turbulent, Boundary Layer, *J. of Fluid Mechanics*, Vol. 182, 85-109.

Sutera, S. P. (1965) Vorticity Amplification in Stagnation-Point Flow and its Effect on Heat Transfer, *J. of Fluid Mechanics*, Vol. 21, part 3, 513-534.

Sutera, S. P., Maeder, P. F. and **Kestin, J.** (1963) On the Sensitivity of Heat Transfer in the Stagnation-Point Boundary Layer to Free-stream Vorticity, *J. of Fluid Mechanics*, Vol. 16, part 3, 497-520.

Sullivan, P. and **Pollard, A.** (1996) Coherent Structure Identification from the Analysis of Hot-Wire Data, *Measurement Science and Technology*, Vol. 7, 1498-1516.

Taneda, S. (1956) Experimental Investigations of the Wakes Behind Cylinders and Plates at Low Reynolds Numbers, *Journal of Physical Society Japan*, Vol. 11, 302-307.

Tennekes, H. and **Lumley, J. L.** (1972) *A First Course in Turbulence*, MIT press, USA.

Tsinober, A., Kit, E. and **Dracos, T.** (1992) Experimental Investigation of the Field of Velocity Gradients in Turbulent Flows, *J. of Fluid Mechanics*, Vol. 242, 169-192.

Turan, Ö. and **Azad, R. S.** (1989) Effect of Hot-Wire Probe Defects on a New Method of Evaluating Turbulence Dissipation, *J. Phys. E: Sci. Instrum.*, Vol. 24, 254-261.

VanFossen, G. J. and Simoneau, R. J. (1987) A Study of the Relationship between Freestream Turbulence and Stagnation Region Heat Transfer, *ASME J. of Heat Transfer*, Vol. 109, no. 1, 10-15.

VanFossen, G. J., Simoneau, R. J. and **Ching, C. Y.** (1995) Influence of Turbulence Parameters, Reynolds Number and Body Shape on Stagnation Region Heat Transfer, *ASME J. of Heat Transfer*, Vol. 117, 597 - 603.

Vukoslaveevic, P., Wallace, J. M. and **Balint, J. M.** (1991) The Velocity and Vorticity Vector Fields of a Turbulent Boundary Layer, Part 1, Simultaneous Measurement by Hot-Wire Anemometry, *J. Fluid Mechanics*, Vol. 228, 25-51.

Vukoslaveevic, P. and **Wallace, J. M.** (1996) A 12-Sensor Hot-Wire Probe to Measure the Velocity and Vorticity Vectors in Turbulent Flow, *Meas. Sci. Technol.*, Vol. 7, 1451-1461.

Wang, H. P., Goldstein, R. J. and **Olson, S. J.** (1999) Effect of High Free-Stream Turbulence With Large Length Scale on Blade Heat/Mass Transfer, *ASME J. of Turbomachinery*, Vol. 121, 217-224.

Wallace, J. M. (1986) Methods of Measuring Vorticity in Turbulent Flows, *Exp. in Fluids*, Vol. 4, 61-71.

Wallace, J. M. and **Foss, J. F.** (1995) The Measurement of Vorticity in Turbulent Flows, *Annu. Rev. Fluid Mech.*, Vol. 27, 469 - 514.

Wassman, W. W. and **Wallace, J. M.** (1979) Measurement of Vorticity in Turbulent Shear Flow, *Bull. Am. Phys. Soc.*, Vol. 24, 1142 (abstr.)

Wei, T. and **Smith, C. R.** (1986) Secondary Vortices in the Wake of Circular Cylinders, *J. of Fluid Mechanics*, Vol. 169, 513-553.

Widrow, B. and **Hoff, M.E.** (1960) Adaptive Switching Circuits, 1960 IRE WESCON Con, Record part 4, 96-104.

Williamson, C. H. K. (1988) The existence of Two Stages in the Transition to Three Dimensionality of a Cylinder Wake, *Physics of Fluids*, Vol. 31, 3165-3167.

Williamson, C. H. K. (1992) The Natural and Forced Formation of 'Sport-Like' Vortex Dislocations in Transition of a Wake, *J. Fluid Mechanics*, Vol. 256, 393-442.

Williamson, C. H. K. (1996a) Three-Dimensional Wake Transition Behind a Cylinder, *J. of Fluid Mechanics*, Vol. 328, 345-407.

Williamson, C. H. K. (1996b) Vortex Dynamics in the Cylinder Wake, *Annual Review of Fluid Mech.*, Vol. 28, 477-539.

Williamson, C. H. K., Wu, J. and **Sheridan, J.** (1995) Scaling of Streamwise Vortices in Wakes, *Physics of Fluids*, Vol. 7, 2307-2309.

Wyngaard J. C. (1969) Spatial Resolution of the Voticity Meter and Other Hot-Wire Arrays, *J. Sci. Instr. (J. Phys. E)* Ser. 22, 983-987.

Yardi, N. R. and **Sukhatme, S. P.** (1978) Effects of Turbulence Intensity and Integral Length Scale of a Turbulent Freestream on Forced Convection Heat Transfer from a Circular Cylinder in Crossflow, 6th International Heat Transfer Conference, Proceedings General Papers, Vol. 5, Nuclear Reactor Heat Transfer, Forced Convection, Paper FC(b)-29, Hemisphere Publ., Washington, D. C., 347-352.

Yavuzkurt, S. (1984) A Guide to Uncertainty Analysis of Hot-Wire Data, *J. of Fluids Engineering*, Vol. 106, pp. 181-186.

Yeh, F. C., Hippensteele, S. A., VanFossen, G. J., Poinsatte, P. E. and **Ameri, A.** (1993) High Reynolds Number and Turbulence Effects on Aerodynamics and Heat Transfer in a Turbine Cascade, *AIAA-93-2252.*

Zdravkovich, M. M. (1997) *Flow around Circular Cylinders, Vol 1: Fundamentals*, Oxford Science Publications, Oxford University Press.

Zhang, H., Fey, U., Noack, B. R., König, M. and **Kckelmann, H.** (1995) On the Transition of the Cylinder Wake, *Physics of Fluids*, Vol. 7, 779-794.

Zhang, L., and **Han, J. C.** (1994) Influence of Mainstream Turbulence on Heat Transfer Coefficients from a Gas Turbine Blade, *ASME J. of Heat Transfer*, Vol. 116, 896-903.

Zhang, L. and **Han, J.C.** (1995) Combined Effect of Freestream Turbulence and Unsteady Wake on Heat Transfer Coefficients from a Gas Turbine Blade, *ASME J. of Heat Transfer*, Vol. 117, 296-302.

Zhou, T. and **Antonia, R. A.** (2000) Reynolds Number Dependence of the Small-Scale Structure of Grid Turbulence, *J. of Fluid Mechanics*, Vol. 406, pp. 81-107.

Zhou, Y., **Antonia, R. A.** and **Tsang, W. K.** (1999) The Effect of the Reynolds Number of the Reynolds Stresses and Vorticity in a Turbulent Far-Wake, *Experimental Thermal and Fluid Science*, Vol. 19, 291-298.

Zhu, Y. and **Antonia, R. A.** (1995) Effect of Wire Separation on X-Probe Measurements in a Turbulent Flow, *J. of Fluid Mechanics*, Vol. 287, 199-223.

Appendix A

Estimation of Conduction Heat Losses through the Leading Edge Body Using A Three-Dimensional Finite Element Model

Part of the energy supplied to the stainless steel foils of the leading edge is lost through the leading edge body by conduction, which is three-dimensional in nature. Preliminary heat transfer tests were conducted in order to estimate the total conduction heat losses from the difference between the average temperatures of the outer surface and inner surface of the leading edge (Equation 3.1e). The points where temperature measurements were taken during the preliminary tests are shown in Figure A.1.

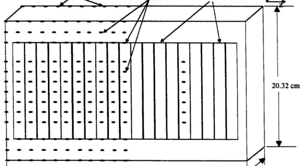

Figure A.1 Temperature Reading Points on the Leading Edge Surface

It should be noted that there are additional temperature reading points apart from the six thermocouples on each stainless steel strip. The same number of temperature reading points with the same y and z coordinates are located on the inner surface (which cannot be seen in Figure A.1). Firstly, the heat transfer tests were performed without turbulence grids. After the steady state was obtained, the temperatures of the reading points shown in Figure A.1 were recorded. Conduction heat losses from each strip were estimated using the ANSYS finite element package, and the flat plate finite element model used is shown in Figure A.2. The flat plate has a width of 3.2 cm, i.e the combined width of two strips and two gaps between strips, and is 0.635 cm thick. The height of the plate model is 20.32 cm, extending 2.54 cm at both ends of the heated stainless steel sheet.

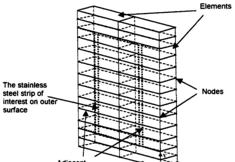

Figure A.2 Flat Plate Finite Element Model for a Stainless Steel Strip (not in scale)

The flat plate model has 26 elements and 84 nodes. The type of element is eight node brick (Solid 70 of the ANSYS package). The coordinates of the nodes, elements, program sample input data and results are given in the last part of this Appendix. The conduction loss from a strip was the weighted average of the heat flux at the nodes on the strip. The total conduction heat losses is the summation of conduction from all strips:

$$Q_{cond} = \int_{i=1}^{19} (q_{cond})_i$$

Where, Q_{cond} = Total conduction losses from the leading edge

$(q_{cond})_i$ = Conduction losses from the stainless steel strip i

The average temperature of the outer and inner surfaces of the leading edge was estimated from the temperature profile of those surfaces. The correction factor C_f was then obtained from:

$$Q_{cond} = kAC_f(Tw_{avg} - Tw_{inner})$$

Where, k = Thermal conductivity of the leading edge

A = Area of the leading edge

C_f = Correction factor for each freestream velocity

Tw_{ave} = Average temperature of the outer surface

Tw_{inner} = Average temperature of the inner surface

The heat transfer tests were repeated with the presence of turbulence generating grids, and the accuracy of the use of correction factors was checked. The total conduction heat losses computed using the correction factors agreed with that given by the finite element models using the ANSYS package within ± 2 percent for all freestream velocity.

List of Nodes (Input Geometry)

```
LIST ALL SELECTED NODES.   DSYS=  0
SORT TABLE ON   NODE  NODE  NODE

   NODE        X                    Y                    Z
      1     0.000000000000E+00   0.000000000000E+00   0.000000000000E+00
      2     0.000000000000E+00   0.127000000000E-01   0.000000000000E+00
      3     0.000000000000E+00   0.254000000000E-01   0.000000000000E+00
      4     0.000000000000E+00   0.404000000000E-01   0.000000000000E+00
      5     0.000000000000E+00   0.579000000000E-01   0.000000000000E+00
      6     0.000000000000E+00   0.753800000000E-01   0.000000000000E+00
      7     0.000000000000E+00   0.928600000000E-01   0.000000000000E+00
      8     0.000000000000E+00   0.110340000000       0.000000000000E+00
      9     0.000000000000E+00   0.127820000000       0.000000000000E+00
     10     0.000000000000E+00   0.145300000000       0.000000000000E+00
     11     0.000000000000E+00   0.162780000000       0.000000000000E+00
     12     0.000000000000E+00   0.177780000000       0.000000000000E+00
     13     0.000000000000E+00   0.190480000000       0.000000000000E+00
     14     0.000000000000E+00   0.203180000000       0.000000000000E+00
     15     0.635000000000E-02   0.000000000000E+00   0.000000000000E+00
     16     0.635000000000E-02   0.127000000000E-01   0.000000000000E+00
     17     0.635000000000E-02   0.254000000000E-01   0.000000000000E+00
     18     0.635000000000E-02   0.404000000000E-01   0.000000000000E+00
     19     0.635000000000E-02   0.579000000000E-01   0.000000000000E+00
     20     0.635000000000E-02   0.753800000000E-01   0.000000000000E+00

   NODE        X                    Y                    Z
     21     0.635000000000E-02   0.928600000000E-01   0.000000000000E+00
     22     0.635000000000E-02   0.110340000000       0.000000000000E+00
     23     0.635000000000E-02   0.127820000000       0.000000000000E+00
     24     0.635000000000E-02   0.145300000000       0.000000000000E+00
     25     0.635000000000E-02   0.162780000000       0.000000000000E+00
     26     0.635000000000E-02   0.177780000000       0.000000000000E+00
     27     0.635000000000E-02   0.190480000000       0.000000000000E+00
     28     0.635000000000E-02   0.203180000000       0.000000000000E+00
     29     0.000000000000E+00   0.000000000000E+00   0.160000000000E-01
     30     0.000000000000E+00   0.127000000000E-01   0.160000000000E-01
     31     0.000000000000E+00   0.254000000000E-01   0.160000000000E-01
     32     0.000000000000E+00   0.404000000000E-01   0.160000000000E-01
     33     0.000000000000E+00   0.579000000000E-01   0.160000000000E-01
```

34	0.000000000000E+00	0.753800000000E-01	0.160000000000E-01
35	0.000000000000E+00	0.928600000000E-01	0.160000000000E-01
36	0.000000000000E+00	0.110340000000	0.160000000000E-01
37	0.000000000000E+00	0.127820000000	0.160000000000E-01
38	0.000000000000E+00	0.145300000000	0.160000000000E-01
39	0.000000000000E+00	0.162780000000	0.160000000000E-01
40	0.000000000000E+00	0.177780000000	0.160000000000E-01

NODE	X	Y	Z
41	0.000000000000E+00	0.190480000000	0.160000000000E-01
42	0.000000000000E+00	0.203180000000	0.160000000000E-01
43	0.635000000000E-02	0.000000000000E+00	0.160000000000E-01
44	0.635000000000E-02	0.127000000000E-01	0.160000000000E-01
45	0.635000000000E-02	0.254000000000E-01	0.160000000000E-01
46	0.635000000000E-02	0.404000000000E-01	0.160000000000E-01
47	0.635000000000E-02	0.579000000000E-01	0.160000000000E-01
48	0.635000000000E-02	0.753800000000E-01	0.160000000000E-01
49	0.635000000000E-02	0.928600000000E-01	0.160000000000E-01
50	0.635000000000E-02	0.110340000000	0.160000000000E-01
51	0.635000000000E-02	0.127820000000	0.160000000000E-01
52	0.635000000000E-02	0.145300000000	0.160000000000E-01
53	0.635000000000E-02	0.162780000000	0.160000000000E-01
54	0.635000000000E-02	0.177780000000	0.160000000000E-01
55	0.635000000000E-02	0.190480000000	0.160000000000E-01
56	0.635000000000E-02	0.203180000000	0.160000000000E-01
57	0.000000000000E+00	0.000000000000E+00	0.320000000000E-01
58	0.000000000000E+00	0.127000000000E-01	0.320000000000E-01
59	0.000000000000E+00	0.254000000000E-01	0.320000000000E-01
60	0.000000000000E+00	0.404000000000E-01	0.320000000000E-01

NODE	X	Y	Z
61	0.000000000000E+00	0.579000000000E-01	0.320000000000E-01
62	0.000000000000E+00	0.753800000000E-01	0.320000000000E-01
63	0.000000000000E+00	0.928600000000E-01	0.320000000000E-01
64	0.000000000000E+00	0.110340000000	0.320000000000E-01
65	0.000000000000E+00	0.127820000000	0.320000000000E-01
66	0.000000000000E+00	0.145300000000	0.320000000000E-01
67	0.000000000000E+00	0.162780000000	0.320000000000E-01
68	0.000000000000E+00	0.177780000000	0.320000000000E-01
69	0.000000000000E+00	0.190480000000	0.320000000000E-01
70	0.000000000000E+00	0.203180000000	0.320000000000E-01
71	0.635000000000E-02	0.000000000000E+00	0.320000000000E-01
72	0.635000000000E-02	0.127000000000E-01	0.320000000000E-01
73	0.635000000000E-02	0.254000000000E-01	0.320000000000E-01
74	0.635000000000E-02	0.404000000000E-01	0.320000000000E-01
75	0.635000000000E-02	0.579000000000E-01	0.320000000000E-01
76	0.635000000000E-02	0.753800000000E-01	0.320000000000E-01
77	0.635000000000E-02	0.928600000000E-01	0.320000000000E-01
78	0.635000000000E-02	0.110340000000	0.320000000000E-01
79	0.635000000000E-02	0.127820000000	0.320000000000E-01
80	0.635000000000E-02	0.145300000000	0.320000000000E-01

NODE	X	Y	Z
81	0.635000000000E-02	0.162780000000	0.320000000000E-01

82	0.635000000000E-02	0.177780000000	0.320000000000E-01
83	0.635000000000E-02	0.190480000000	0.320000000000E-01
84	0.635000000000E-02	0.203180000000	0.320000000000E-01

List of Elements (Input Geometry)

LIST ALL SELECTED ELEMENTS. (LIST NODES)

ELEM	MAT	TYP	REL	ESY	SEC	NODES							
1	1	1	1	0	1	1	15	16	2	29	43	44	30
2	1	1	1	0	1	29	43	44	30	57	71	72	58
3	1	1	1	0	1	2	16	17	3	30	44	45	31
4	1	1	1	0	1	30	44	45	31	58	72	73	59
5	1	1	1	0	1	3	17	18	4	31	45	46	32
6	1	1	1	0	1	31	45	46	32	59	73	74	60
7	1	1	1	0	1	4	18	19	5	32	46	47	33
8	1	1	1	0	1	32	46	47	33	60	74	75	61
9	1	1	1	0	1	5	19	20	6	33	47	48	34
10	1	1	1	0	1	33	47	48	34	61	75	76	62
11	1	1	1	0	1	6	20	21	7	34	48	49	35
12	1	1	1	0	1	34	48	49	35	62	76	77	63
13	1	1	1	0	1	7	21	22	8	35	49	50	36
14	1	1	1	0	1	35	49	50	36	63	77	78	64
15	1	1	1	0	1	8	22	23	9	36	50	51	37
16	1	1	1	0	1	36	50	51	37	64	78	79	65
17	1	1	1	0	1	9	23	24	10	37	51	52	38
18	1	1	1	0	1	37	51	52	38	65	79	80	66
19	1	1	1	0	1	10	24	25	11	38	52	53	39
20	1	1	1	0	1	38	52	53	39	66	80	81	67

ELEM	MAT	TYP	REL	ESY	SEC	NODES							
21	1	1	1	0	1	11	25	26	12	39	53	54	40
22	1	1	1	0	1	39	53	54	40	67	81	82	68
23	1	1	1	0	1	12	26	27	13	40	54	55	41
24	1	1	1	0	1	40	54	55	41	68	82	83	69
25	1	1	1	0	1	13	27	28	14	41	55	56	42
26	1	1	1	0	1	41	55	56	42	69	83	84	70

List of Temperature at Nodes (Input Loads)

LIST CONSTRAINTS FOR SELECTED NODES 1 TO 84 BY 1
CURRENTLY SELECTED DOF SET= TEMP

NODE	LABEL	REAL	IMAG
1	TEMP	21.6200000	0.000000000E+00
2	TEMP	25.0100000	0.000000000E+00

3	TEMP	35.5700000	0.000000000E+00
4	TEMP	36.1400000	0.000000000E+00
5	TEMP	36.7100000	0.000000000E+00
6	TEMP	36.6800000	0.000000000E+00
7	TEMP	36.7300000	0.000000000E+00
8	TEMP	36.7000000	0.000000000E+00
9	TEMP	36.2300000	0.000000000E+00
10	TEMP	36.4100000	0.000000000E+00
11	TEMP	36.8100000	0.000000000E+00
12	TEMP	36.3100000	0.000000000E+00
13	TEMP	35.8100000	0.000000000E+00
14	TEMP	22.0100000	0.000000000E+00
15	TEMP	21.4200000	0.000000000E+00
16	TEMP	26.2300000	0.000000000E+00
17	TEMP	29.0100000	0.000000000E+00
18	TEMP	31.2700000	0.000000000E+00
19	TEMP	31.3900000	0.000000000E+00
20	TEMP	31.4100000	0.000000000E+00
NODE	LABEL	REAL	IMAG
21	TEMP	30.9800000	0.000000000E+00
22	TEMP	31.2200000	0.000000000E+00
23	TEMP	31.1800000	0.000000000E+00
24	TEMP	31.2900000	0.000000000E+00
25	TEMP	30.9900000	0.000000000E+00
26	TEMP	28.0700000	0.000000000E+00
27	TEMP	27.3100000	0.000000000E+00
28	TEMP	22.7100000	0.000000000E+00
29	TEMP	22.0400000	0.000000000E+00
30	TEMP	26.8500000	0.000000000E+00
31	TEMP	36.8900000	0.000000000E+00
32	TEMP	37.1600000	0.000000000E+00
33	TEMP	37.4200000	0.000000000E+00
34	TEMP	37.9500000	0.000000000E+00
35	TEMP	37.1800000	0.000000000E+00
36	TEMP	37.4600000	0.000000000E+00
37	TEMP	37.2800000	0.000000000E+00
38	TEMP	37.8600000	0.000000000E+00
39	TEMP	37.2100000	0.000000000E+00
40	TEMP	36.5600000	0.000000000E+00
NODE	LABEL	REAL	IMAG
41	TEMP	28.6700000	0.000000000E+00
42	TEMP	23.0500000	0.000000000E+00
43	TEMP	22.4000000	0.000000000E+00
44	TEMP	26.7500000	0.000000000E+00
45	TEMP	29.9400000	0.000000000E+00
46	TEMP	31.9000000	0.000000000E+00
47	TEMP	31.4500000	0.000000000E+00
48	TEMP	32.3400000	0.000000000E+00
49	TEMP	31.8500000	0.000000000E+00
50	TEMP	31.2800000	0.000000000E+00
51	TEMP	31.9100000	0.000000000E+00
52	TEMP	31.9200000	0.000000000E+00

```
  53  TEMP   28.9600000       0.000000000E+00
  54  TEMP   29.0100000       0.000000000E+00
  55  TEMP   27.0100000       0.000000000E+00
  56  TEMP   22.3500000       0.000000000E+00
  57  TEMP   22.0400000       0.000000000E+00
  58  TEMP   31.2500000       0.000000000E+00
  59  TEMP   37.9400000       0.000000000E+00
  60  TEMP   38.4800000       0.000000000E+00

NODE  LABEL     REAL             IMAG
  61  TEMP   38.9800000       0.000000000E+00
  62  TEMP   39.1600000       0.000000000E+00
  63  TEMP   38.9000000       0.000000000E+00
  64  TEMP   38.9000000       0.000000000E+00
  65  TEMP   38.2800000       0.000000000E+00
  66  TEMP   38.5900000       0.000000000E+00
  67  TEMP   38.0600000       0.000000000E+00
  68  TEMP   37.5200000       0.000000000E+00
  69  TEMP   32.9900000       0.000000000E+00
  70  TEMP   22.7800000       0.000000000E+00
  71  TEMP   22.0100000       0.000000000E+00
  72  TEMP   31.2600000       0.000000000E+00
  73  TEMP   32.2200000       0.000000000E+00
  74  TEMP   33.4100000       0.000000000E+00
  75  TEMP   33.9200000       0.000000000E+00
  76  TEMP   33.9100000       0.000000000E+00
  77  TEMP   33.3300000       0.000000000E+00
  78  TEMP   33.4300000       0.000000000E+00
  79  TEMP   33.0700000       0.000000000E+00
  80  TEMP   33.5500000       0.000000000E+00

NODE  LABEL     REAL             IMAG
  81  TEMP   32.9400000       0.000000000E+00
  82  TEMP   29.9900000       0.000000000E+00
  83  TEMP   27.7800000       0.000000000E+00
  84  TEMP   23.0400000       0.000000000E+00
```

List of Heat Flux at Nodes (Solutions)

```
PRINT TF   NODAL SOLUTION PER NODE

 ***** POST1 NODAL THERMAL FLUX LISTING *****
 PowerGraphics Is Currently Enabled

 LOAD STEP=     1  SUBSTEP=     1
 TIME=    1.0000        LOAD CASE=   0
 NODAL RESULTS ARE FOR MATERIAL    1

 THE FOLLOWING X,Y,Z VALUES ARE IN GLOBAL COORDINATES
```

NODE	TFX	TFY	TFZ	TFSUM
1	6.3	-54.	-5.3	54.
2	-39.	-0.11E+03	-23.	0.12E+03
3	0.21E+03	-87.	-17.	0.23E+03
4	0.15E+03	-7.1	-13.	0.15E+03
5	0.17E+03	-3.1	-8.9	0.17E+03
6	0.17E+03	-0.11	-16.	0.17E+03
7	0.18E+03	-0.11	-5.7	0.18E+03
8	0.17E+03	2.9	-9.5	0.17E+03
9	0.16E+03	1.7	-13.	0.16E+03
10	0.16E+03	-3.3	-18.	0.16E+03
11	0.18E+03	1.1	-5.0	0.18E+03
12	0.26E+03	7.3	-3.1	0.26E+03
13	0.27E+03	0.11E+03	90.	0.31E+03
14	-22.	0.22E+03	-13.	0.22E+03
15	6.3	-76.	-12.	77.
16	-39.	-60.	-6.5	72.
17	0.21E+03	-37.	-12.	0.21E+03
18	0.15E+03	-16.	-7.9	0.16E+03
19	0.17E+03	-0.80	-0.75	0.17E+03
20	0.17E+03	2.4	-12.	0.17E+03
21	0.18E+03	1.1	-11.	0.18E+03
22	0.17E+03	-1.1	-0.75	0.17E+03
23	0.16E+03	-0.40	-9.2	0.16E+03
24	0.16E+03	1.1	-7.9	0.16E+03
25	0.18E+03	21.	26.	0.19E+03
26	0.26E+03	26.	-12.	0.26E+03
27	0.27E+03	42.	3.8	0.27E+03
28	-22.	73.	4.5	76.
29	-11.	-76.	-2.6	77.
30	3.2	-0.12E+03	-39.	0.12E+03
31	0.22E+03	-81.	-15.	0.23E+03
32	0.17E+03	-3.3	-15.	0.17E+03
33	0.19E+03	-4.5	-14.	0.19E+03
34	0.18E+03	1.4	-16.	0.18E+03
35	0.17E+03	2.8	-14.	0.17E+03

NODE	TFX	TFY	TFZ	TFSUM
36	0.20E+03	-0.57	-14.	0.20E+03
37	0.17E+03	-2.3	-13.	0.17E+03
38	0.19E+03	0.40	-14.	0.19E+03
39	0.26E+03	8.1	-7.9	0.26E+03
40	0.24E+03	67.	-7.6	0.25E+03
41	53.	0.11E+03	18.	0.12E+03
42	22.	89.	-4.8	92.
43	-11.	-69.	-3.7	70.
44	3.2	-60.	-32.	68.
45	0.22E+03	-38.	-20.	0.22E+03
46	0.17E+03	-11.	-13.	0.17E+03
47	0.19E+03	-2.5	-16.	0.19E+03
48	0.18E+03	-2.3	-16.	0.18E+03
49	0.17E+03	6.1	-15.	0.17E+03
50	0.20E+03	-0.34	-14.	0.20E+03
51	0.17E+03	-3.7	-12.	0.17E+03

52	0.19E+03	17.	-14.	0.19E+03
53	0.26E+03	17.	-12.	0.26E+03
54	0.24E+03	15.	-12.	0.24E+03
55	53.	53.	-3.0	74.
56	22.	74.	-2.1	77.
57	0.95	-0.15E+03	-0.25E-11	0.15E+03
58	-0.32	-0.13E+03	-55.	0.14E+03
59	0.18E+03	-57.	-13.	0.19E+03
60	0.16E+03	-6.5	-17.	0.16E+03
61	0.16E+03	-3.9	-20.	0.16E+03
62	0.17E+03	0.46	-15.	0.17E+03
63	0.18E+03	1.5	-22.	0.18E+03
64	0.17E+03	3.6	-18.	0.17E+03
65	0.16E+03	1.8	-13.	0.17E+03
66	0.16E+03	1.3	-9.2	0.16E+03
67	0.16E+03	6.7	-11.	0.16E+03
68	0.24E+03	39.	-12.	0.24E+03
69	0.16E+03	0.12E+03	-54.	0.21E+03
70	-8.2	0.16E+03	3.4	0.16E+03
NODE	TFX	TFY	TFZ	TFSUM
71	0.95	-0.15E+03	4.9	0.15E+03
72	-0.32	-81.	-57.	99.
73	0.18E+03	-16.	-29.	0.18E+03
74	0.16E+03	-11.	-19.	0.16E+03
75	0.16E+03	-2.9	-31.	0.16E+03
76	0.17E+03	3.4	-20.	0.17E+03
77	0.18E+03	2.8	-19.	0.18E+03
78	0.17E+03	1.5	-27.	0.18E+03
79	0.16E+03	-0.69	-15.	0.17E+03
80	0.16E+03	0.75	-20.	0.16E+03
81	0.16E+03	23.	-50.	0.17E+03
82	0.24E+03	37.	-12.	0.24E+03
83	0.16E+03	55.	-9.7	0.17E+03
84	-8.2	75.	-8.7	76.

MINIMUM VALUES

NODE	2	71	72	1
VALUE	-39.	-0.15E+03	-57.	54.

MAXIMUM VALUES

NODE	13	14	13	13
VALUE	0.27E+03	0.22E+03	90.	0.31E+03

Appendix B

Estimation of Experimental Uncertainties

B.1 Uncertainties in Frossling Number

For each variable measured (or estimated), the total uncertainty can be calculated from:

$$Un = [B^2 + P^2]^{1/2}$$

where Un = Total uncertainty

B = Bias error

P = Precision error

Total uncertainty (Un)

The ±Un interval about the result presented is the band within which the experimenter is 95% confident that the true value of the result lies.

Bias error (B)

The bias error is an estimate of the magnitude of the fixed, constant error. It is assigned with the understanding the experimenter is 95% confident that the true value of the bias error would be less than $|B|$. The bias error of the variable measured is usually based on the resolution of the equipment and the error specifications provided by the manufacturer. For instance, the multimeter has a resolution of 0.01 ampere, which is taken as constant error by taking the calibration error of the equipment into account, in measuring the current flow. The average currents to the leading edge for the maximum and minimum freestream velocity of the tests are 5.56 and 3.85 amperes, respectively.

Therefore, the percentage bias error in current I is 0.18 percent (= 0.01/5.56 *100) for the maximum velocity, and the 0.26 percent (= 0.01/3.85) for the minimum freestream velocity.

The bias error for estimated variables are calculated using the root-sum-square method (Moffat, 1988), which is the basis for all uncertainty estimation. If the result R of the experiment is calculated from the a set of measured (or estimated) variables:

$$R = R(x_1, x_2, x_3, \ldots\ldots\ldots, x_N)$$

then, the bias error of the variable R is given by the root-sum-square method:

$$B_R = \left[\sum_{i=1}^{N} \left(\frac{\partial R}{\partial x_i} B_{x_i} \right)^2 \right]^{1/2}$$

The partial derivative of R with respect to x_i is the sensitivity coefficient for the result R with respect to the measurement x_i. In case the variable R is estimated from a pure product form of a set of variables:

$$R = x_1^{\,a}\, x_2^{\,b}\, x_3^{\,c} \ldots\ldots\ldots x_N^{\,m}$$

then, the root-sum-square method gives the bias error in R:

$$\frac{B_R}{R} = \left[\left(a \frac{B_{x_1}}{x_1} \right)^2 + \left(b \frac{B_{x_2}}{x_2} \right)^2 + \ldots\ldots\ldots\ldots + \left(m \frac{B_{x_N}}{x_N} \right)^2 \right]^{1/2}$$

The bias errors of energy input to the leading edge Q_{in}, heat losses Q_{rad} and Q_{cond}, Nusselt number Nu and Frossling number Fr were estimated by applying the root-sum-square method to the Equation 3.1.

Precision error (P)

The $\pm P$ interval of a result is the 95% confidence estimate of the band within which the true value of the result falls, if the experiment were repeated many times under the same conditions using the same equipment. Thus, the precision error is an estimate of the lack of repeatability caused by random errors and unsteadiness.

The precision error of the single sample parameter, i.e voltage, current and freestream mean velocity for this study, is estimated from the standard deviation (S) of the population of the measurements (31 samples were taken for each piece of equipment in this study). The ratio of precision error to the standard deviation (P/S) for 31 samples ranges between 1.34 to 0.8 (see Moffat, 1988), and the average value [=(1.34+0.8)/2] is taken for this study. For instance, to estimate the precision error of the TSI velocity meter at the maximum freestream velocity, 31 samples were taken running the wind tunnel at U=10.5 m/s. The sample data (in m/s) is:

U=[10.50, 10.50, 10.50, 10.55, 10.50, 10.55, 10.45, 10.50, 10.50, 10.50, 10.45, 10.50, 10.55, 10.55, 10.50, 10.50, 10.50, 10.55, 10.45, 10.45, 10.50, 10.50, 10.50, 10.50, 10.50, 10.45, 10.50, 10.55, 10.50, 10.50, 10.45]

The standard deviation (S) of the sample was estimated to be 0.0316 m/s, and the precision error P was calculated using the ratio of P/S for the population of 31 samples:

$$P/S = (1.34+0.8)/2$$

Therefore, the percentage precision error of the TSI meter for the maximum freestream velocity is 0.322 (=P/U=0.03381/10.5 *100).

The precision error of a multiple-sample parameter, i.e. temperature readings of thermocouples for this experiment, can be considered based on statistical theories. Multiple-sample tests are those in which enough data is taken at each test point to support a sound statistical interpretation of the random error characteristics of the set. In this study, the reading of a thermocouple was the average of the set of 180 data points, the standard deviation of which was lower than the bias error of the thermocouple. Therefore, the precision error in temperature was assumed to be equivalent to the bias error. The precision error of an estimated variable can be calculated using the root-sum-square methods similar to that mentioned in the bias error section.

B.2 Uncertainty in Tu, λ_x and ω

The uncertainty of the hot-wire data includes calibration uncertainty, α, and curve-fitting uncertainty, β (Yavuzkurt, 1984). Total uncertainty in a parameter is calculated depending on how this parameter is estimated and the number of curve-fittings involved. For instance, the uncertainty in the streamwise fluctuating velocity component can be estimated:

$$Un_u = [\alpha^2 - \beta^2]^{1/2}$$

However, total uncertainty in integral length scale needs to take into account the additional uncertainty in curve-fitting for autocorrelation function.

Calibration uncertainty (α)

Calibration uncertainty is mainly due to the uncertainty in velocity measurement in calibrating the hot-wire. Since the TSI velocity meter was used for calibration, the total uncertainty, i.e. combined bias and precision errors, in velocity measurement was taken as the calibration uncertainty. Unlike the velocity measurement in estimation of the Frossling number, where the velocity was the single-sample parameter, the velocity readings were recorded as multiple-sample parameters (31 readings for each freestream velocity) in the calibration process in order to reduce the precision error.

Curve-fitting uncertainty (β)

From the curve fit data, uncertainty β can be calculated as follows (Yavuzkurt, 1984):

$$\beta = \left[\frac{\sum_{i=1}^{n} \left(\frac{\Delta U}{U} \right)_i^2}{n} \right]^{1/2}$$

where	U	= Measured velocity (m/s)
	ΔU	= Difference between the measured and curve-fitted data (m/s)
	n	= Total numbers of data points for curve-fitting

The root-sum-square method was applied to the Equations 3.9 and 3.10 to estimate the uncertainty in integral length scale, and to the Equations 3.11 and 3.12 to determine the uncertainty in fluctuating vorticity components.

Appendix C

Calibration and Data Reduction Programs for Hot-wires

C.1 Single Wire

C.1.1 Velocity Calibration

```
clear
% Script file to obtain a calibration curve for s-wire
% filename: xcalib.m
% generate sequence of file names
file = [ 'scal00.dat'; 'scal01.dat'; 'scal02.dat'; 'scal03.dat'; 'scal04.dat'; 'scal05.dat';
'scal06.dat'; 'scal07.dat'; 'scal08.dat'; 'scal09.dat'; 'scal10.dat'; 'scal11.dat'; 'scal12.dat';
'scal13.dat'; 'scal14.dat'; 'scal15.dat'; 'scal16.dat'; ];
for n=1:size(file,1);                                        % file incrementer
    fid = fopen(file(n,1:size(file,2)),'r');
    data = fscanf(fid, '%i %i', [1, inf]);
    hwire1(n) = mean(data(1,1:size(data,2)));
    fclose(fid);
    clear data;
end;
tsi_vel=[0.00 1.87 2.47 3.13 3.75 4.35 5.02 5.82 6.48 7.28 8.00 8.75 9.28 9.88 10.50
11.40 12.25];
pxm3100a1 = polyfit(hwire1, tsi_vel,3);
```

```
x=linspace(100,2500,100);
y1=polyval(pxm3100a1,x);
y = polyval(pxm3100a1, hwire1);
plot(hwire1, tsi_vel,'r+',x,y1,'k--');
title('Calibration Curve for S-Wire  data set, Mar. 16, 2000');
xlabel('Hot Wire Signal (A/D Data)');
ylabel('Velocity (TSI meter),m/sec.');
axis([300 2500 0 13.0])
save pxm3100a1 pxm3100a1;
```

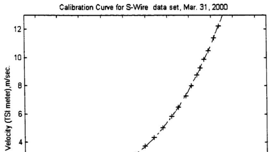

Figure C1 Calibration Curve for Single Wire

C.1.2 Estimation of U and Tu

```
clear
% Script file to analyze mean and rms velocity.      % filename : xmsave.m
load pxm3100a1;
file1 = ['ss111.dat'; 'ss121.dat'; 'ss131.dat'; 'ss611.dat'; 'ss621.dat'; 'ss631.dat'; 'ss211.dat';
'ss221.dat'; 'ss231.dat'; 'ss711.dat'; 'ss721.dat'; 'ss731.dat'; 'ss311.dat'; 'ss321.dat'; 'ss331.
'ss811.dat'; 'ss821.dat'; 'ss831.dat'; 'ss411.dat'; 'ss421.dat'; 'ss431.dat'; 'ss911.dat';
'ss921.dat'; 'ss931.dat'; 'ss511.dat'; 'ss521.dat'; 'ss531.dat'; ];
nu = 0.0000155;
for n=1:size(file1,1);                                   %file incrementer
    fid = fopen(file1(n,1:size(file1,2)),'r');
    data = fscanf(fid, '%i %i', [1, inf]);
    ndata_1=data(1,:);
    u1 = polyval(pxm3100a1,ndata_1);
    if n<10
        dt = 1/30000;
        [z,wn]=buttord(14000/15000,15000/15000,1,50);
    else
        dt = 1/20000;
        [z,wn]=buttord(9500/10000,10000/10000,1,50);
    end
    [b,a]=butter(z,wn);
```

```
    u1f=filter(b,a,u1);
    u=u1f(100:139900);
    u_mean(n)=mean(u(1,1:size(u,2)));
    u_prime = u-u_mean(n);
    clear data ndata_1;
    fclose(fid);
    u_rms(n) = std(u);
    tu(n)=(u_rms(n)/u_mean(n))*100;
    %-------------------------------
    for i = 2:(size(u,2)-1);
        dupdt(i)  = (u_prime(i+1)-u_prime(i-1))/(2*dt);        % (dv/dt)
        dupdx(i)  = dupdt(i)/u_mean(n);                        % (dv/dt)/U
    end;
    dupdxrms(n) = std(dupdx);
    epsilon(n) = 15*nu*(dupdxrms(n))^2;          % mean of dissipation rate
    eta(n)     = (nu^3/epsilon(n)).^0.25;        % Kolomogorov length scale
    tau(n)     = (nu/epsilon(n)).^0.5;           % Kolomogorov time scale
    fK(n)      = u_mean(n)/(2*22/7*eta(n));      % Kolomogorov frequency
    VK(n) = (nu*epsilon(n)).^0.25;               % Kolomogorov velocity scale
    clear u_prime u;
end;                                             %repeat for every file
y=linspace(1,27,27);
```

```
save umean.dat y u_mean -ASCII;
save tuinten.dat y tu -ASCII;
save urms.dat y u_rms -ASCII;
save epseta.dat y epsilon eta -ASCII;
save taufk.dat y tau fK -ASCII;
save dupdx.dat y dupdxrms -ASCII;
save vk.dat y VK -ASCII;
clear n m fid file1 pxm3100a1;
```

C.1.3 Autocorrelation

```
clear
load pxm3100a1;
file1 = ['ss111.dat'; 'ss121.dat'; 'ss131.dat'; 'ss611.dat'; 'ss621.dat'; 'ss631.dat'; 'ss211.dat';
'ss221.dat'; 'ss231.dat'; 'ss711.dat'; 'ss721.dat'; 'ss731.dat'; 'ss311.dat'; 'ss321.dat';
'ss331.dat'; 'ss811.dat'; 'ss821.dat'; 'ss831.dat'; 'ss411.dat'; 'ss421.dat'; 'ss431.dat';
'ss911.dat'; 'ss921.dat'; 'ss931.dat'; 'ss511.dat';'ss521.dat'; 'ss531.dat'; ];
nu = 0.0000155;
x=linspace(1,250,250);
for n=1:size(file1,1);                                    %file incrementer
    fid = fopen(file1(n,1:size(file1,2)),'r');
    data = fscanf(fid, '%i %i', [1, inf]);
    ndata_1=data(1,:);
```

```
u1 = polyval(pxm3100a1,ndata_1);
if n<10
    dt = 1/30000;
    [z,wn]=buttord(14000/15000,15000/15000,1,50);
else
    dt = 1/20000;
    [z,wn]=buttord(9500/10000,10000/10000,1,50);
end
y=x*dt*12;
[b,a]=butter(z,wn);
u1f=filter(b,a,u1);
u=u1f(100:139900);
u_mean(n)=mean(u(1,1:size(u,2)));
u_prime = u-u_mean(n);
clear data ndata_1;
fclose(fid);
u_rms(n) = std(u);
for j=1:250;
    for i = 1:(size(u,2)-(j*12)-1);
        uprimebar(i)=u_prime(i+(j*12)-1)*u_prime(i)/(u_rms(n)*u_rms(n));
    end;
    auto(n,j)=mean(uprimebar);
```

```
    end;
    clear u_prime u;
end;
save autocor.dat y auto -ASCII;   clear n m fid file1 pxm3100a1;
```

C.2 X-Wire

C.2.1 Velocity Calibration

```
clear
% Script file to obtain a calibration curve for X-wire    % filename: xcalib.m
file = [ 'xcal00.dat'; 'xcal01.dat'; 'xcal02.dat'; 'xcal03.dat'; 'xcal04.dat'; 'xcal05.dat';
'xcal06.dat'; 'xcal07.dat'; 'xcal08.dat'; 'xcal09.dat'; 'xcal10.dat'; 'xcal11.dat'; 'xcal12.dat';
'xcal13.dat'; 'xcal14.dat'; 'xcal15.dat'; 'xcal16.dat'; ];
for n=1:size(file,1);                                   % file incrementer
        fid = fopen(file(n,1:size(file,2)),'r');
        data = fscanf(fid, '%i %i', [2, inf]);
        hwire1(n) = mean(data(1,1:size(data,2)));
        hwire2(n) = mean(data(2,1:size(data,2)));
        fclose(fid);
        clear data;
end;                                                    % repeat for every file
tsi_vel=[0.00 1.80 2.59 3.14 3.89 4.47 5.00 5.75 6.38 7.32 8.00 8.77 9.28 9.87 10.50
 11.40 12.35];
```

```
pxa0500a1 = polyfit(hwire1, tsi_vel,3); pxa0500a2 = polyfit(hwire2, tsi_vel,3);
x=linspace(200,2400,100);
y1=polyval(pxa0500a1,x); y2=polyval(pxa0500a2,x);
y = polyval(pxa0500a1, hwire1);  z = polyval(pxa0500a2, hwire2);
plot(hwire1, tsi_vel,'r+',x,y1,'k--',hwire2,tsi_vel,'gx',x,y2,'k--');
title('Calibration Curve for X-Wire  data set, Apr. 05, 2000');
xlabel('Hot Wire Signal (A/D Data)');ylabel('Velocity (TSI meter),m/sec.');
axis([200 2400 0 13.0]); save pxa0500a1 pxa0500a1; save pxa0500a2 pxa0500a2;
```

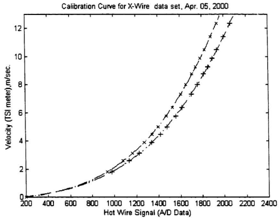

Figure C2 Velocity Calibration Curve for X-wire

C.2.2 Yaw Angle Calibration

```
clear

% tetaef.m : Script file to obtain teta effective

load pxa0500a1;

load pxa0500a2;

file = [ 'xa00.dat'; 'xa06.dat'; 'xa05.dat'; 'xa04.dat'; 'xa03.dat'; 'xa02.dat'; 'xa01.dat';

'xa07.dat'; 'xa08.dat'; 'xa09.dat'; 'xa10.dat'; 'xa11.dat'; 'xa12.dat'; ];

yaw = [30 25 20 15 10 5 -5 -10 -15 -20 -25 -30];

for n = 1 :size(file,1);

        fid = fopen(file(n,1:size(file,2)),'r');

        data = fscanf(fid,'%i %i', [2, inf]);

        hw1(n) = mean(data(1,1:size(data,2)));

        hw2(n) = mean(data(2,1:size(data,2)));

        fclose(fid);

        clear data;

end;                    % repeat for every file

for n = 1 : size(file,1);

        vel_1(n) = polyval(pxa0500a1,hw1(n));

        vel_2(n) = polyval(pxa0500a2,hw2(n));

end;

for n = 1: size(file,1);

        efang_1(n)  = atan((cos(yaw(n)*pi/180)-(vel_1(n)/8.1839))/sin(-yaw(n)*pi/180));
```

```
        efang_2(n) = atan((cos(yaw(n)*pi/180)-(vel_2(n)/8.2183))/sin(yaw(n)*pi/180));
        tetaef_1(n) = efang_1(n)*180/pi;
        tetaef_2(n) = efang_2(n)*180/pi;
end;                                        %repeat for every file
av_eff_1 = mean(tetaef_1); av_eff_2 = mean(tetaef_2)
plot(yaw,tetaef_1,'r+',yaw,tetaef_2,'gx',yaw,tetaef_1,'y',yaw,tetaef_2,'b');
title('Effective angle versus Teta yaw, Mar. 18, 2000');
xlabel('Teta yaw, Degree'); ylabel('Effective angle of wires, Degree');
clear n fid file;
```

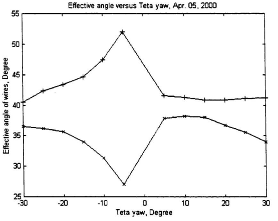

Figure C3 Yaw Angle Calibration for X-wire

C.2.4 Estimation of Fluctuating Velocity Components

```
clear
% Script file to analyze mean and rms of a set of x-wire data.  % filename : xmsave.m
load pxa0500a1;
load pxa0500a2;
file1 = ['xs111.dat'; 'xs121.dat'; 'xs131.dat'; 'xs611.dat'; 'xs621.dat'; 'xs631.dat';
'xs211.dat'; 'xs221.dat'; 'xs231.dat'; 'xs711.dat'; 'xs721.dat'; 'xs731.dat'; 'xs311.dat';
'xs321.dat'; 'xs331.dat'; 'xs811.dat'; 'xs821.dat'; 'xs831.dat'; 'xs411.dat'; 'xs421.dat';
'xs431.dat'; 'xs911.dat'; 'xs921.dat'; 'xs931.dat'; 'xs511.dat'; 'xs521.dat'; 'xs531.dat'; ];
file2 = ['xp111.dat'; 'xp121.dat'; 'xp131.dat'; 'xp611.dat'; 'xp621.dat'; 'xp631.dat';
'xp211.dat'; 'xp221.dat'; 'xp231.dat'; 'xp711.dat'; 'xp721.dat'; 'xp731.dat'; 'xp311.dat';
'xp321.dat'; 'xp331.dat'; 'xp811.dat'; 'xp821.dat'; 'xp831.dat'; 'xp411.dat'; 'xp421.dat';
'xp431.dat'; 'xp911.dat'; 'xp921.dat'; 'xp931.dat'; 'xp511.dat'; 'xp521.dat'; 'xp531.dat'; ];
nu = 0.0000155;
tteta_1 = 43.0944;              % teta 1 effective in degrees
tteta_2 = 35.0726;              % teta 2 effective in degrees
teta1 = tteta_1*pi/180;         % teta 1 effective in radian
teta2 = tteta_2*pi/180;         % teta 2 effective in radian
tanteta1=tan(teta1);
tanteta2=tan(teta2);
costeta1=cos(teta1);
for n=1:size(file1,1);          %file incrementer
```

```
fid = fopen(file1(n,1:size(file1,2)),'r');
data = fscanf(fid, '%i %i', [2, inf]);
ndata_1=data(1,:);
ndata_2=data(2,:);
u1 = polyval(pxa0500a1,ndata_1);
u2 = polyval(pxa0500a2,ndata_2);
if n<10
    dt = 1/30000;
    [z,wn]=buttord(14000/15000,15000/15000,1,50);
else
    dt = 1/20000;
    [z,wn]=buttord(9500/10000,10000/10000,1,50);
end
[b,a]=butter(z,wn);
u1f=filter(b,a,u1);
u1=u1f(100:99900);
u2f=filter(b,a,u2);
u2=u2f(100:99900);
for q =1:size(u1,2);
        u(q) = (costeta1*u1(q))/(cos(teta1-atan((u1(q)/u2(q)
        1)/(tanteta2*u1(q)/u2(q)+tanteta1))))*cos(atan((u1(q)/u2(q)-
        1)/(tanteta2*u1(q)/u2(q)+tanteta1)));
```

```
        v(q) = (costeta1*u1(q))/(cos(teta1-atan((u1(q)/u2(q)-
        1)/(tanteta2*u1(q)/u2(q)+tanteta1))))*sin(atan((u1(q)/u2(q)-
        1)/(tanteta2*u1(q)/u2(q)+tanteta1)));
end;
u_mean(n)=mean(u(1,1:size(u,2)));
v_mean(n)=mean(v(1,1:size(v,2)));
u_prime = u-u_mean(n);
v_prime = v-v_mean(n);
clear data ndata_1 ndata_2;
fclose(fid);
u_rms(n) = std(u);
v_rms(n) = std(v);
tu(n)=(u_rms(n)/u_mean(n))*100;
for i = 2:(size(u1,2)-1);
        dvpdt(i)  = (v_prime(i+1)-v_prime(i-1))/(2*dt);      % (dv/dt)
        dvpdx(i)  = dvpdt(i)/u_mean(n);                      % (dv/dt)/U
        dupdt(i)  = (u_prime(i+1)-u_prime(i-1))/(2*dt);      % (dv/dt)
        dupdx(i)  = dupdt(i)/u_mean(n);                      % (dv/dt)/U
end;
dvpdxrms(n) = std(dvpdx);                     % mean of (du/dx)^2
dupdxrms(n) = std(dupdx);
epsilon(n)  = 15*nu*(dupdxrms(n))^2;          % mean of dissipation rate
```

```
        eta(n)   = (nu^3/epsilon(n)).^0.25;                    % Kolomogorov length scale
        tau(n)   = (nu/epsilon(n)).^0.5;                       % Kolomogorov time scale
        fK(n)    = u_mean(n)/(2*22/7*eta(n));                  % Kolomogorov frequency
        VK(n) = (nu*epsilon(n)).^0.25;                         % Kolomogorov velocity scale
        clear beta s u1 u2 u_prime v_prime u v ;
end;                                                           %repeat for every file
y=linspace(1,27,27);
for n=1:size(file2,1);                                         %file incrementer
        fid = fopen(file2(n,1:size(file2,2)),'r');
        data = fscanf(fid, '%i %i', [2, inf]);
        ndata_1=data(1,:);
        ndata_2=data(2,:);
        u1 = polyval(pxa0500a1,ndata_1);
        u2 = polyval(pxa0500a2,ndata_2);
        if n<10
                dt = 1/30000;
                [z,wn]=buttord(14000/15000,15000/15000,1,50);
        else
                dt = 1/20000;
                [z,wn]=buttord(9500/10000,10000/10000,1,50);
        end
        [b,a]=butter(z,wn);
```

```
u1f=filter(b,a,u1);
u1=u1f(100:99900);
u2f=filter(b,a,u2);
u2=u2f(100:99900);
for q =1:size(u1,2);
        uxz(q) = (costeta1*u1(q))/(cos(teta1-atan((u1(q)/u2(q)-
        1)/(tanteta2*u1(q)/u2(q)+tanteta1))))*cos(atan((u1(q)/u2(q)-
        1)/(tanteta2*u1(q)/u2(q)+tanteta1)));
        w(q) = (costeta1*u1(q))/(cos(teta1-atan((u1(q)/u2(q)-
        1)/(tanteta2*u1(q)/u2(q)+tanteta1))))*sin(atan((u1(q)/u2(q)-
        1)/(tanteta2*u1(q)/u2(q)+tanteta1)));
end;
uxz_mean(n)=mean(uxz(1,1:size(uxz,2)));
w_mean(n)=mean(w(1,1:size(w,2)));
uxz_prime = uxz-uxz_mean(n);
w_prime = w-w_mean(n);
clear data ndata_1 ndata_2;
fclose(fid);
uxz_rms(n) = std(uxz);
w_rms(n) = std(w);
tuxz(n)=(uxz_rms(n)/uxz_mean(n))*100;
for i = 2:(size(u1,2)-1);
```

```
            dwpdt(i)  = (w_prime(i+1)-w_prime(i-1))/(2*dt);            % (dv/dt)
            dwpdx(i)  = dwpdt(i)/uxz_mean(n);                          % (dv/dt)/U
            duxzpdt(i)  = (uxz_prime(i+1)-uxz_prime(i-1))/(2*dt);      % (dv/dt)
            duxzpdx(i)  = duxzpdt(i)/uxz_mean(n);
        end;
        dwpdxrms(n) = std(dwpdx);                              % mean of (du/dx)^2
        duxzpdxrms(n) = std(duxzpdx);
        clear beta s u1 u2 uxz_prime w_prime uxz w;
end;                                                               %repeat for every file
save umean.dat y u_mean uxz_mean -ASCII;
save tuinten.dat y tu tuxz -ASCII;
save uvrms.dat y u_rms v_rms -ASCII;
save uxzwrms.dat y uxz_rms w_rms -ASCII;
save pdxrms.dat y dvpdxrms dwpdxrms -ASCII;
save vwmean.dat y v_mean w_mean -ASCII;
save epseta.dat y epsilon eta -ASCII;
save taufk.dat y tau fK -ASCII;
save dupdx.dat y dupdxrms duxzpdxrms -ASCII;
save vk.dat y VK -ASCII;
clear n m fid file1 file2 pxa0500a1 pxa0500a2 teta1 teta2 tteta_1 tteta_2;
```

C.3 Vorticity Probe

C.3.1 Velocity Calibration

```
clear

% Script file to obtain a calibration curve for v-wire, filename: vcalib.m

file = [ 'vcal00.dat'; 'vcal01.dat'; 'vcal02.dat'; 'vcal03.dat'; 'vcal04.dat'; 'vcal05.dat';
'vcal06.dat'; 'vcal07.dat'; 'vcal08.dat'; 'vcal09.dat'; 'vcal10.dat'; 'vcal11.dat'; 'vcal12.dat';
'vcal13.dat'; 'vcal14.dat'; 'vcal15.dat'; 'vcal16.dat'; ];

for n=1:size(file,1);                                    % file incrementer
        fid = fopen(file(n,1:size(file,2)),'r');
        data = fscanf(fid, '%i %i', [4, inf]);
        hwire1(n) = mean(data(1,1:size(data,2)));
        hwire2(n) = mean(data(2,1:size(data,2)));
        hwire3(n) = mean(data(3,1:size(data,2)));
        hwire4(n) = mean(data(4,1:size(data,2)));
        fclose(fid);
        clear data;
end;                                  % repeat for every file

tsi_vel=[0.00 1.79 2.50 3.27 3.90 4.48 5.03 5.77 6.40 7.28 8.02 8.73 9.12 9.82 10.50
11.25 12.20];

pxa1700a1 = polyfit(hwire1, tsi_vel,3); pxa1700a2 = polyfit(hwire2, tsi_vel,3);
pxa1700a3 = polyfit(hwire3, tsi_vel,3); pxa1700a4 = polyfit(hwire4, tsi_vel,3);
x=linspace(200,2000,100);
```

```
y1=polyval(pxa1700a1,x); y2=polyval(pxa1700a2,x);
y3=polyval(pxa1700a3,x); y4=polyval(pxa1700a4,x);
plot(hwire1, tsi_vel,'r+',x,y1,'k--',hwire2,tsi_vel,'gx',x,y2,'k--',hwire3,
tsi_vel,'m+',x,y3,'k',hwire4,tsi_vel,'bx',x,y4,'k');
title('Calibration Curve for V-Wire  data set, Apr. 17, 2000');
xlabel('Hot Wire Signal (A/D Data)'); ylabel('Velocity (TSI meter),m/sec.');
axis([200 2000 0 12.5]);
save pxa1700a1 pxa1700a1; save pxa1700a2 pxa1700a2;
save pxa1700a3 pxa1700a3; save pxa1700a4 pxa1700a4;
```

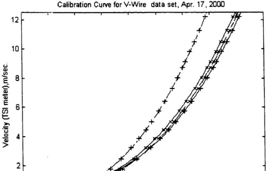

Figure C4 Velocity Calibration for Vorticity Probe

C.3.2 Yaw Angle Calibration

```
clear

% tetaef.m : Script file to obtain teta effective

% Filename: tetaef.m

load pxa1700a1;

load pxa1700a2;

file = ['va00.dat'; 'va06.dat'; 'va05.dat'; 'va04.dat'; 'va03.dat'; 'va02.dat'; 'va01.dat';

'va07.dat'; 'va08.dat'; 'va09.dat'; 'va10.dat'; 'va11.dat'; 'va12.dat'; ];

yaw = [0 30 25 20 15 10 5 -5 -10 -15 -20 -25 -30];

for n = 1 :size(file,1);

        fid = fopen(file(n,1:size(file,2)),'r');

        data = fscanf(fid,'%i %i', [4, inf]);

        hw1(n) = mean(data(1,1:size(data,2)));

        hw2(n) = mean(data(2,1:size(data,2)));

        fclose(fid);

        clear data;

end;                                    % repeat for every file

for n = 1 : size(file,1);

        vel_1(n) = polyval(pxa1700a1,hw1(n));

        vel_2(n) = polyval(pxa1700a2,hw2(n));

end;

for n = 1: size(file,1);
```

```
        efang_1(n)  = atan((cos(yaw(n)*pi/180)-(vel_1(n)/8.0655))/sin(-yaw(n)*pi/180));
        efang_2(n)  = atan((cos(yaw(n)*pi/180)-(vel_2(n)/8.0634))/sin(yaw(n)*pi/180));
        tetaef_1(n) = efang_1(n)*180/pi;
        tetaef_2(n) = efang_2(n)*180/pi;
end;                                            %repeat for every file
av_eff_1 = mean(tetaef_1)
av_eff_2 = mean(tetaef_2)
plot(yaw,tetaef_1,'r+',yaw,tetaef_2,'gx',yaw,tetaef_1,'y',yaw,tetaef_2,'b');
title('Effective angle versus Teta yaw, Apr. 12, 2000');
xlabel('Teta yaw, Degree');
ylabel('Effective angle of wires, Degree');
clear n fid file
```

C.3.3 Estimation of Fluctuating Vorticity Components

```
clear
% filename : vmsave.m
% Script file to estimate the fluctuating vorticity components
load pxa1700a1;
load pxa1700a2;
load pxa1700a3;
load pxa1700a4;
```

```
file1 = ['vm111.dat'; 'vm121.dat'; 'vm131.dat'; 'vm611.dat'; 'vm621.dat'; 'vm631.dat';
'vm211.dat'; 'vm221.dat'; 'vm231.dat'; 'vm711.dat'; 'vm721.dat'; 'vm731.dat'; 'vm311.dat';
'vm321.dat'; 'vm331.dat'; 'vm811.dat'; 'vm821.dat'; 'vm831.dat'; 'vm411.dat'; 'vm421.dat';
'vm431.dat'; 'vm911.dat'; 'vm921.dat'; 'vm931.dat'; 'vm511.dat'; 'vm521.dat'; 'vm531.dat';
];
file2 = ['vn111.dat'; 'vn121.dat'; 'vn131.dat'; 'vn611.dat'; 'vn621.dat'; 'vn631.dat';
'vn211.dat'; 'vn221.dat'; 'vn231.dat'; 'vn711.dat'; 'vn721.dat'; 'vn731.dat'; 'vn311.dat';
'vn321.dat'; 'vn331.dat'; 'vn811.dat'; 'vn821.dat'; 'vn831.dat'; 'vn411.dat'; 'vn421.dat';
'vn431.dat'; 'vn911.dat'; 'vn921.dat'; 'vn931.dat'; 'vn511.dat'; 'vn521.dat'; 'vn531.dat'; ];
nu = 0.0000155;
tteta_1 = 56.4064;          % teta 1 effective in degrees
tteta_2 = 49.4436;          % teta 2 effective in degrees
teta1 = tteta_1*pi/180;     % teta 1 effective in radian
teta2 = tteta_2*pi/180;     % teta 2 effective in radian
tanteta1=tan(teta1);
tanteta2=tan(teta2);
costeta1=cos(teta1);
ystar=[9.67 11.66 12.67 8.81 10.13 10.72 8.45 9.21 9.67 5.90 7.28 8.01 5.46 6.60 7.28
5.23 6.20 6.79 4.94 5.74 6.19 4.87 5.48 5.99 4.75 5.31 5.71];
for n=1:size(file1,1);                              %file incrementer
        fid = fopen(file1(n,1:size(file1,2)),'r');
        data = fscanf(fid, '%i %i', [4, inf]);
```

```
ndata_1=data(1,:);
ndata_2=data(2,:);
ndata_3=data(3,:);
ndata_4=data(4,:);
u1 = polyval(pxa1700a1,ndata_1);
u2 = polyval(pxa1700a2,ndata_2);
u3 = polyval(pxa1700a3,ndata_3);
u4 = polyval(pxa1700a4,ndata_4);
if n<10
        dt = 1/30000;
        [z,wn]=buttord(14000/15000,15000/15000,1,50);
else
        dt = 1/20000;
        [z,wn]=buttord(9500/10000,10000/10000,1,50);
end
[b,a]=butter(z,wn);
u1f=filter(b,a,u1);
u1=u1f(100:52001);
u2f=filter(b,a,u2);
u2=u2f(100:52001);
u3f=filter(b,a,u3);
u3=u3f(100:52001);
```

```
u4f=filter(b,a,u4);
u4=u4f(100:52001);
for q =1:size(u1,2);
        u(q) = (costeta1*u1(q))/(cos(teta1-atan((u1(q)/u2(q)-
        1)/(tanteta2*u1(q)/u2(q)+tanteta1))))*cos(atan((u1(q)/u2(q)-
        1)/(tanteta2*u1(q)/u2(q)+tanteta1)));
        v(q) = (costeta1*u1(q))/(cos(teta1-atan((u1(q)/u2(q)-
        1)/(tanteta2*u1(q)/u2(q)+tanteta1))))*sin(atan((u1(q)/u2(q)-
        1)/(tanteta2*u1(q)/u2(q)+tanteta1)));
end;
u_mean(n)=mean(u(1,1:size(u,2)));
v_mean(n)=mean(v(1,1:size(v,2)));
u_prime = u-u_mean(n);
v_prime = v-v_mean(n);
clear data ndata_1 ndata_2 ndata_3 ndata_4;
fclose(fid);
u_rms(n) = std(u);
v_rms(n) = std(v);
tu(n)=(u_rms(n)/u_mean(n))*100;
for i = 2:(size(u1,2)-2);
    if n<10
        dvpdt(i)  = (v_prime(i+2)-v_prime(i-1))/(3*dt);
```

```
    else
        dvpdt(i)  = (v_prime(i+1)-v_prime(i-1))/(2*dt);
    end
    dvpdx(i)  = dvpdt(i)/u_mean(n);
    if n<10
        dupdt(i)  = (u_prime(i+2)-u_prime(i-1))/(3*dt);
    else
        dupdt(i)  = (u_prime(i+1)-u_prime(i-1))/(2*dt);
    end
    dupdx(i)  = dupdt(i)/u_mean(n);
    corre(n)  =  1.0185-0.0319*ystar(n)-0.0011*(ystar(n))^2;
    dupdy(i)  =(u3(i)-u4(i))/(corre(n)*0.0013);
    omegaz(i)  = -dvpdx(i)-dupdy(i);
end;
dvpdxrms(n) = std(dvpdx);
dupdxrms(n) = std(dupdx);
dupdyrms(n) = std(dupdy);
omegazrms(n)= std(omegaz);
epsilon(n)  = 15*nu*(dupdxrms(n))^2;          % mean of dissipation rate
eta(n)    = (nu^3/epsilon(n)).^0.25;          % Kolomogorov length scale
tau(n)    = (nu/epsilon(n)).^0.5;             % Kolomogorov time scale
fK(n)     = u_mean(n)/(2*22/7*eta(n));        % Kolomogorov frequency
```

```
        VK(n)      = (nu*epsilon(n)).^0.25;                  % Kolomogorov velocity scale
        clear beta s u1 u2 u3 u4 u_prime v_prime u v ;
end;
y=linspace(1,27,27);

for n=1:size(file2,1);                              %file incrementer
        fid = fopen(file2(n,1:size(file2,2)),'r');
        data = fscanf(fid, '%i %i', [4, inf]);
        ndata_1=data(1,:);
        ndata_2=data(2,:);
        ndata_3=data(3,:);
        ndata_4=data(4,:);
        u1 = polyval(pxa1700a1,ndata_1);
        u2 = polyval(pxa1700a2,ndata_2);
        u3 = polyval(pxa1700a3,ndata_3);
        u4 = polyval(pxa1700a4,ndata_4);
        if n<10
            dt = 1/30000;
            [z,wn]=buttord(14000/15000,15000/15000,1,50);
        else
            dt = 1/20000;
            [z,wn]=buttord(9500/10000,10000/10000,1,50);
```

```
end
[b,a]=butter(z,wn);
u1f=filter(b,a,u1);
u1=u1f(100:52001);
u2f=filter(b,a,u2);
u2=u2f(100:52001);
u3f=filter(b,a,u3);
u3=u3f(100:52001);
u4f=filter(b,a,u4);
u4=u4f(100:52001);
for q =1:size(u1,2);
    uxz(q) = (costeta1*u1(q))/(cos(teta1-atan((u1(q)/u2(q)-
    1)/(tanteta2*u1(q)/u2(q)+tanteta1))))*cos(atan((u1(q)/u2(q)-
    1)/(tanteta2*u1(q)/u2(q)+tanteta1)));
    w(q) = (costeta1*u1(q))/(cos(teta1-atan((u1(q)/u2(q)-
    1)/(tanteta2*u1(q)/u2(q)+tanteta1))))*sin(atan((u1(q)/u2(q)-
    1)/(tanteta2*u1(q)/u2(q)+tanteta1)));
end;
uxz_mean(n)=mean(uxz(1,1:size(uxz,2)));
w_mean(n)=mean(w(1,1:size(w,2)));
uxz_prime = uxz-uxz_mean(n);
w_prime = w-w_mean(n);
```

```
clear data ndata_1 ndata_2 ndata_3 ndata_4;
fclose(fid);
uxz_rms(n) = std(uxz);
w_rms(n) = std(w);
tuxz(n)=(uxz_rms(n)/uxz_mean(n))*100;
for i = 2:(size(u1,2)-2);

    if n<10
        dwpdt(i)  = (w_prime(i+2)-w_prime(i-1))/(3*dt);
    else
        dwpdt(i)  = (w_prime(i+1)-w_prime(i-1))/(2*dt);
    end
    dwpdx(i)  = dwpdt(i)/uxz_mean(n);
    if n<10
        duxzpdt(i)  = (uxz_prime(i+2)-uxz_prime(i-1))/(3*dt);
    else
        duxzpdt(i)  = (uxz_prime(i+1)-uxz_prime(i-1))/(2*dt);
    end
    duxzpdx(i)  = duxzpdt(i)/uxz_mean(n);
    corre(n)   =   1.0185-0.0319*ystar(n)-0.0011*(ystar(n))^2;
    dupdz(i)  =(u3(i)-u4(i))/(corre(n)*0.0013);
    omegay(i) = dupdz(i) + dwpdx(i);
```

```
        end;
        dwpdxrms(n) = std(dwpdx);
        duxzpdxrms(n) = std(duxzpdx);
        dupdzrms(n) = std(dupdz);
        omegayrms(n)= std(omegay);
        clear beta s u1 u2 u3 u4 uxz_prime w_prime uxz w;
end;                            %repeat for every file

save umean.dat y u_mean uxz_mean -ASCII;
save tuinten.dat y tu tuxz -ASCII;
save uvrms.dat y u_rms v_rms -ASCII;
save uwrms.dat y uxz_rms w_rms -ASCII;
save pdxrms.dat y dvpdxrms dwpdxrms -ASCII;
save durms.dat y dupdyrms dupdzrms -ASCII;
save omega.dat y omegazrms omegayrms -ASCII;
save vwmean.dat y v_mean w_mean -ASCII;
save epseta.dat y epsilon eta -ASCII;
save taufk.dat y tau fK -ASCII;
save dupdx.dat y dupdxrms duxzpdxrms -ASCII;
save vk.dat y VK -ASCII;
clear n m fid pxa1700a1 pxa1700a2 pxa1700a3 pxa1700a4 teta1 teta2 tteta_1 tteta_2;
```

C.3.4 Wavelet Energy Spectrum

```
% program for Wavelet spectrum analysis
clear
load pxf0700a1;
load pxf0700a2;
file1 = ['xb111.dat';
  ];
file2 = ['xd111.dat';
  ];
dt = 1/30000;
nu = 0.0000155;
tteta_1 = 42.9980;      % teta 1 effective in degrees
tteta_2 = 38.7307;      % teta 2 effective in degrees
teta1 = tteta_1*pi/180;       % teta 1 effective in radian
teta2 = tteta_2*pi/180;       % teta 2 effective in radian
tanteta1=tan(teta1);
tanteta2=tan(teta2);
costeta1=cos(teta1);
for n=1:size(file1,1);                      %file incrementer
   fid = fopen(file1(n,1:size(file1,2)),'r');
   data = fscanf(fid, '%i %i', [2, inf]);
   ndata_1=data(1,:);
```

```
ndata_2=data(2,:);
u1 = polyval(pxf0700a1,ndata_1);
u2 = polyval(pxf0700a2,ndata_2);
u1=u1(1000:10000);
u2=u2(1000:10000);
for q =1:size(u1,2);
   u(q) = (costeta1*u1(q))/(cos(teta1-atan((u1(q)/u2(q) 1) /(tanteta2*u1(q)/u2(q)
  +tanteta1)))) *cos(atan((u1(q)/u2(q)-1)/(tanteta2*u1(q)/u2(q)+tanteta1)));
   v(q) = (costeta1*u1(q))/(cos(teta1-atan((u1(q)/u2(q)-1) /(tanteta2*u1(q)
  /u2(q)+tanteta1))))*sin(atan((u1(q)/u2(q)-1)/(tanteta2*u1(q)/u2(q)+tanteta1)));
end;
u_mean(n)=mean(u(1,1:size(u,2)));
v_mean(n)=mean(v(1,1:size(v,2)));
u_prime = u-u_mean(n);
v_prime = v-v_mean(n);
clear data ndata_1 ndata_2;
 fclose(fid);
 c1=cwt(u_prime,2:256,'mexh');
  ua=columns(c1);
  c2=cwt(v_prime,2:256,'mexh');
  va=columns(c2);
 %------------------------------
```

```
  clear beta s u1 u2 u v u1f u2f uu vv uvins u_prime v_prime c1 c2;
end;                                    %repeat for every file
for n=1:size(file2,1);                  %file incrementer
  fid = fopen(file2(n,1:size(file2,2)),'r');
  data = fscanf(fid, '%i %i', [2, inf]);
  ndata_1=data(1,:);
  ndata_2=data(2,:);
  u1 = polyval(pxf0700a1,ndata_1);
  u2 = polyval(pxf0700a2,ndata_2);
  u1=u1(1000:10000);
  u2=u2(1000:10000);
  for q =1:size(u1,2);
    w(q) = (costeta1*u1(q))/(cos(teta1-atan((u1(q)/u2(q)-1) /(tanteta2*u1(q) /u2(q)
      +tanteta1))))*sin(atan((u1(q)/u2(q)-1)/(tanteta2*u1(q)/u2(q)+tanteta1)));
  end;
  w_mean(n)=mean(w(1,1:size(w,2)));
  w_prime = w-w_mean(n);
  clear data ndata_1 ndata_2;
  fclose(fid);
  c3=cwt(w_prime,2:256,'mexh');
  wa=columns(c3);
```

```
  clear beta s u1 u2 uxz w u1f u2f ww uwins w_prime c3;
end;                          %repeat for every file
save spweng111.dat ua va wa -ASCII;
clear n m fid file1 file2 pxf0700a1 pxf0700a2 teta1 teta2 tteta_1 tteta_2;
clear q pitot_vel press rho temp uu vv ww;

% Function used in the "Spectrum-wavelet.m" file
function AVC=columns(inp1)
%----------------------------------
clear AVC;
clear sumco;
for p =1:(size(inp1,1));
  sumco(p)= 0;
  for q=1:(size(inp1,2));
     sumco(p)=sumco(p)+(inp1(p,q))^2;
   end;
  AVC(p)=sumco(p);
end;
```